Dissertation

submitted to the
Combined Faculties for the Natural Sciences and for Mathematics
of the
Ruperto-Carola University of Heidelberg, Germany
for the degree of

Doctor of Natural Sciences

Put forward by
Dipl.-Phys.: Stefan Ohm
Born in: Sondershausen, Germany

Oral examination: 21 May 2010

Development of an

Advanced γ/hadron separation technique

and application to particular

γ-ray sources with H.E.S.S.

Referees: Prof. Dr. Werner Hofmann
Prof. Dr. Heinz Völk

Abstract

The High Energy Stereoscopic system, H.E.S.S. is an array of four imaging atmospheric Čerenkov telescopes, designed for the study of non-thermal phenomena in the universe at very high energies (VHE). The sensitivity of telescope systems such as H.E.S.S. can considerably be improved by a better discrimination of the vast number of hadronic cosmic-ray background events against the very rare γ-ray signal events. In this work, an elaborated discrimination technique – the Boosted Decision Tree method – has been developed and its capabilities in terms of γ/hadron separation and improved sensitivity are demonstrated. In the second part, the BDT method is applied to data obtained in observations of massive star forming environments, namely the colliding wind binary η Carinae, the massive stellar cluster Westerlund 1 and the Starburst galaxy NGC 253. An upper limit on the γ-ray flux of the famous colliding wind binary system η Carinae is derived and, for the first time, an alternative model for the high-energy emission observed by the Fermi satellite is presented. The detection of very extended VHE γ-ray emission from the vicinity of Westerlund 1 is reported and thorough spectral and morphological tests are presented. Large parts of the resolved emission can be explained in a hadronic scenario, however, a decisive conclusion can not be drawn. Finally, the BDT method allowed to detect the first Starburst galaxy, namely NGC253, in VHE γ rays. Spectral and morphological results are presented and suggest that large parts of the CR energy content are convectively and diffusively transported into the intergalactic medium.

Kurzfassung

H.E.S.S. ist ein System aus vier abbildenden Čerenkov Teleskopen und untersucht das nicht-thermische Universum bei Energien im 100 GeV – 100 TeV Bereich. Die Sensitivität von H.E.S.S. ist hauptsächlich durch die effektive Unterdrückung der enormen Anzahl an hadronischen Untergrundereignissen in der Analyse bestimmt. In dieser Arbeit wurde eine neue Analysemethode, die sogenannte Boosted Decision Trees (BDT) Methode, auf Daten und Simulationen angewendet und zeigt ein enormes Potential in der γ/Hadron Separation. Ausführliche Tests mit Simulationen und Beobachtungsdaten realer Gammaquellen demonstrieren die Eignung der BDT Methode und zeigen eine deutlich höhere Signifikanz im Vergleich zur Standardanalyse. Im zweiten Teil der Arbeit wurde die BDT Methode auf Beobachtungsdaten von Regionen massiver Sternformation angewendet. Die Analyse von Daten aus Richtung des berühmten Binärsystems η Carinae ergab eine Flussobergrenze, die im Vergleich mit Messungen des Fermisatelliten interessante Implikationen auf Beschleunigungsprozesse zulassen. Sehr ausgedehnte Gammastrahlungsemission wurde aus der Umgebung des massiven Sternhaufens Westerlund 1 detektiert. Detaillierte systematische Tests hinsichtlich der Morphologie und des Energiespektrums wurden durchgefuehrt. Ein Teil der Emission könnte in einem hadronischen Szenario erklärt werden. Schliesslich konnte mit Hilfe der BDT Analyse das erste Gammasignal von einer “Starburst” Galaxie – NGC 253 – nachgewiesen werden.

There is no all-seeing, all-loving god who keeps us free from harm; but atheism is not a recipe for despair – I think the opposite. By disclaiming the idea of a next life, we can take more excitement in this one. The here and now is not something to be *endured* before eternal bliss or damnation; the here and now is all we have – an inspiration to make the most of it. So atheism is life-affirming in a way religion can never be.

Look around you: nature demands our attention, begs us to explore, to question. Religion can provide only facile, ultimately unsatisfying answers. Science, in constantly seeking real explanations, reveals the true majesty of our world in all it's complexity. Sometimes people say, "There must be more than just this world, than just this life..." *But how much more do you want?*

We are going to die, *and that makes us the lucky ones.* Most people are never going to die because they are never going to be born. The number of people who could be here in my place outnumber the sand grains of Sahara. If you think of all the different ways in which our genes could be permuted, you and I are quite grotesquely lucky to be here – the number of events that had to happen in order for you to exist, in order for me to exist...

We are privileged to be alive, and we should make the most of our time on this world.

Richard Dawkins

Contents

List of Figures

List of Tables

Preface

In recent years, very high energy (VHE; $E > 100$ GeV) γ-ray astronomy has established as a new discipline in astronomy. Key instruments in this field, *Imaging Atmospheric Čerenkov Telescopes* (IACTs), devoted for the quest of the origin of Galactic cosmic rays (GCRs), opened a previously inaccessible window for the study of astrophysical objects at very high energies. Currently, the most successful IACT system is the *High Energy Stereoscopic System* (H.E.S.S.), which is situated in the Khomas Highlands in Namibia and comprised of four telescopes of same architecture. With its large field of view (f.o.v.), its high sensitivity and southern hemisphere location it is well suited for the search of new VHE γ-ray sources in a survey of the Galactic plane. Since 2004, when the deep and extensive Galactic Plane Scan (GPS) started, the number of detected γ-ray emitters in the Milky Way continuously increased and is to date reaching more than ≈ 50 sources. Of these, not only supernova remnants (SNRs) – which are believed to be a major source of GCRs – but also a rich diversity of other astrophysical objects could be identified as VHE γ-ray emitters. Even though a large part of the γ-ray source population remains unidentified in other wavelengths, a significant fraction of the identified objects, namely e.g. SNRs, pulsar wind nebulae (PWNe) and γ-ray binary systems, are associated to late stages of stellar evolution. Moreover, some sources are spatially coincident with massive star forming regions and massive stellar clusters, the birthplaces of SNR- and PWN progenitor stars.

Beyond individual γ-ray emitters in our Milky Way, extragalactic objects such as e.g. radio galaxies or Active Galactic Nuclei (AGN) were detected in the VHE regime as well. The variety of Galactic and extragalactic objects discovered so far, emit VHE γ rays at a flux level, which made their detection possible within a reasonably short amount of observation time. However, after five years of operation, H.E.S.S. is now getting into the regime where presumably all strong VHE γ-ray sources have been detected. Hence, a significantly larger amount of observation time is required to establish weaker sources as VHE γ-ray emitters. Especially extragalactic objects such as Starburst galaxies or Galaxy clusters and Galactic objects such as colliding wind binaries (CWB) are predicted to emit γ rays at a flux level which is right at the edge or slightly below the sensitivity of H.E.S.S.[1].

The sensitivity of IACTs is mainly determined by two components: The effective detection area, namely the area on ground which is covered by telescopes, and the effective discrimination of the vast hadronic background against the very rare γ-ray signal events. Therefore, a better sensitivity can be achieved by an increased number of telescopes spread over a larger area on ground and/or by an improved background reduction. Regarding the former, large arrays of telescopes are currently under study by different consortia and will most likely start operation within the next $10 - 15$ years. Still, the sensitivity of existing instruments can be considerably improved with a better γ/hadron separation.

[1] See Fig. 0.1 for a sketch of astrophysical objects detected in very high energies so far and yet undiscovered objects.

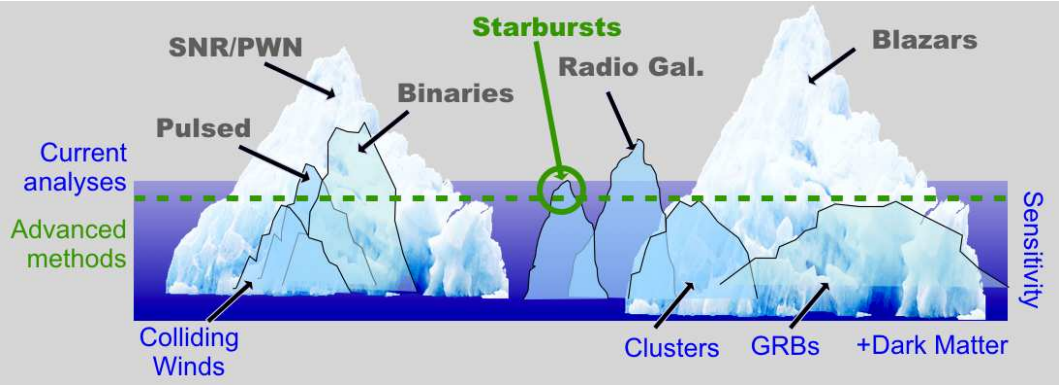

Figure 0.1: The tip of the iceberg of object classes already discovered and yet to be discovered in VHE γ-ray astronomy. Fig. adapted from Horan & Weekes (2004) and kindly provided by J. Hinton.

The development of such an advanced discrimination technique – called *Boosted Decision Trees* (BDT) – is one of the main goals of this work and addressed in the first part. In the second part of this work, the BDT method is applied to H.E.S.S. data obtained in observations of regions of massive star formation. On small scales, VHE γ-ray emission is searched for in the famous CWB η Carinae. Even though no significant excess was found, the derived flux upper limit in combination with the detection of high energy (HE; 100 MeV $\leq E \leq$ 100 GeV) emission by the Fermi satellite has interesting implications for the underlying physical processes in this system. Furthermore, extended VHE γ-ray emission from the vicinity of the massive stellar cluster Westerlund 1 has been detected. The spectral and morphological characteristics of the emission are presented and implications on the origin of the γ-ray excess are discussed. Ultimately, the detection of the first Starburst galaxy in VHE γ rays, namely NGC 253, nicely illustrates the potential of elaborated γ/hadron discrimination methods.

This work is organized as follows:

- ◇ In Chapter 1, the successful experimental imaging atmospheric Čerenkov technique is presented. The H.E.S.S. experiment, its calibration and data analysis scheme is discussed in more detail. The chapter concludes with a description of the successes and limitations of the *Hillas*-based γ/hadron separation.
- ◇ Chapter 2 focuses on the multivariate BDT method and its training, testing and evaluation with Monte-Carlo γ-ray simulations and real data. The performance improvements of this approach are validated with γ-ray data obtained in observations of various γ-ray sources.
- ◇ The theoretical background of physical processes at work in CWB systems, massive stellar cluster and Starburst galaxies is discussed in Chapter 3.
- ◇ In Chapter 4, γ-ray data of observations of η Carinae and the Carina star forming region are presented and discussed. An alternative HE γ-ray emission scenario is presented, which for the first time, tries to explain the γ-ray emission as resulting from particle acceleration in the expanding material which originates in the historical 1843 'giant eruption'.

- ◇ The detection of extended VHE γ-ray emission from the vicinity of the most massive stellar cluster Westerlund 1 is presented in Chapter 5. A detailed morphological and spectral analysis suggests particle acceleration in and around the cluster and γ-ray production in hadronic interactions with the surrounding material. Possible associations to objects which could also be responsible for the observed excess are discussed in more detail.

- ◇ Chapter 6 presents the BDT analysis results of extensive observations of the Starburst galaxy NGC 253 and its detection in VHE γ rays. The position of the signal of the weakest γ-ray source found so far is spatially coincident with the Starburst nucleus of the galaxy. The energy spectrum is compatible with results found by the Fermi satellite as well as with model predictions and suggest just a mildly calorimetric system in which major parts of the CR energy are diffusively and convectively lost and transported into the intergalactic medium (IGM).

- ◇ Chapter 7 summarizes the findings of this work and gives a brief outlook on the potential of the BDT method. The importance of future observations of the discussed objects in different wavelength bands is emphasized.

1 Detection of VHE γ rays with H.E.S.S.

The Earth's atmosphere is opaque to high-energy γ rays. When γ rays enter the atmosphere they induce electromagnetic particle cascades, also referred to as *Extensive Air Shower* (EAS), by interacting with molecules and atoms in air. While the detection of high-energy (HE; 1 MeV $\leq$ E $\leq$ 100 GeV) γ-ray primaries is led by satellite-based instruments like e.g. EGRET (Hartman et al. 1999), INTEGRAL (Winkler et al. 2003), AGILE (Tavani et al. 2009a) and the LAT instrument on board the recently launched Fermi satellite (Ritz et al. 2007), the steep decline of particle flux with increasing energy makes it more and more difficult for the m^2-sized detectors to collect a significant amount of photons with even higher energies within their typical operation time of $\mathcal{O}(10)$ years. Therefore, an indirect measurement using the atmosphere as integral part of the detector is required to compensate this declining particle flux with a tremendously increased detection area. In recent years, the Imaging Atmospheric Čerenkov Technique has proven to be the most successful experimental ground-based method to study VHE γ rays in the 100 GeV to 100 TeV regime. Čerenkov light emitted by the charged, relativistic particles in an EAS is measured by *imaging atmospheric Čerenkov telescopes* (IACTs), which then extract directional and spectral information about the primary particle. Whereas satellite-based instruments benefit from quasi background free observations with small detection areas, Čerenkov telescopes achieve the five order of magnitude increased detection area at the expense of a huge component of hadronic cosmic-ray (CR) background events. The sensitivity of IACTs is directly determined by the capability to suppress the CR background. The nature of the primary particle can be deduced using the shape of their induced EAS. The physical processes at work during the formation of EAS induced by VHE γ rays and hadronic CRs and their properties are reviewed in Section 1.1. The principle of the Imaging Atmospheric Čerenkov technique and the High Energy Stereoscopic System (H.E.S.S.), the currently most successful VHE γ-ray experiment, is introduced in Section 1.2. Finally, this chapter concludes with a description of the data analysis scheme applied to H.E.S.S. data, its successes as well as its limitations in terms of γ/hadron separation.

1.1 Air showers

When a high-energy particle (e.g. a CR nucleus or a photon) enters the outer layers of Earth's atmosphere it interacts with molecules and atoms in air and initiates a cascade of secondary particles – this cascade is also referred to as EAS. Depending on the type of the primary particle, the induced EAS can have two different components: in case a photon, electron or positron is impinging a shower of electromagnetic nature develops. On the other hand, if a CR nucleus interacts via the strong force, not only electromagnetic but also hadronic sub-showers develop. The basic properties of electromagnetic and hadronic showers are reviewed in the following.

1.1.1 Electromagnetic showers

The formation and dissolution of an electromagnetic particle cascade is characterised by three processes: Bremsstrahlung and pair production are responsible for the creation of secondary particles, whereas ionisation of air molecules leads at the same time to the expiration of the shower. A photon which enters the atmosphere creates an $e^{\pm}$ pair in the Coulomb field of a nucleus. The secondary electrons and positrons[1] get deflected by the charged nuclei and subsequently emit secondary Bremsstrahlung photons. Both processes build up a cascade of particles until the mean particle energy drops below ≈ 80 MeV. At this critical energy E_c the energy loss via ionisation of air molecules dominates over the creation of new particles via Bremsstrahlung and pair production. At this point the shower has reached its maximum particle number and starts to die out.

The characteristic length scale, or mean free path length, after which an electron lost all but $1/e$ of its initial energy due to the Bremsstrahlung process is called radiation length X_0. It is expressed as traversed atmospheric depth and measured in units of g cm^{-2}:

$$\left(-\frac{dE}{dx}\right) = \frac{E_0}{X_0}\,. \tag{1.1}$$

In air, the radiation length is $X_0 = 37.2$ g cm^{-2} for electrons emitting Bremsstrahlung photons and $X_{0,\gamma} = 9/7\ X_0$ for photons creating $e^{\pm}$ pairs. That implies that even if the electromagnetic cascades triggered by electrons and photons have similar shape due to the same underlying interaction processes, the first interaction of electrons occurs slightly higher in the atmosphere compared to γ rays, which makes them to some extent distinguishable. This discrimination becomes important in the analysis of CR electrons, where the diffuse γ-ray contribution needs to be estimated (Aharonian et al. 2008a).

Heitler (1954) introduced a simple model (illustrated in Fig. 1.1), which can be used to derive basic properties of an electromagnetic air shower using three simplifications: *(1)* The radiation length of electrons and the conversion length of photons are assumed to be equal, namely X_0. *(2)* Pair production and Bremsstrahlung are the only processes which create secondary particles. *(3)* The energy is shared equally between secondary particles after every interaction process. In this toy model, the shower consists of $N(x) = 2^{x/X_0}$ particles with energy $E(x) = E_0 \cdot 2^{-x/X_0}$ after a travelled distance x. The maximum number of particles $N_{\max} = 2^{X_{\max}/X_0} = E_0/E_c$ in the cascade is reached at the shower maximum at an atmospheric depth $X_{\max}$ of:

$$X_{\max} = \frac{\ln E_0/E_c}{\ln 2} \cdot X_0\ , \tag{1.2}$$

where the critical energy E_c is given by $E_c = E_0 \cdot 2^{-X_{\max}/X_0}$. In summary, this model predicts three important quantities; The number of particles in the shower grows exponentially until the shower maximum is reached. The number of particles in the shower is furthermore proportional to the primary particle energy. The depth of the shower maximum logarithmically depends on the primary particle energy.

The simple Heitler model illustrates the basic properties of a γ-ray induced EAS: A γ ray of 1 TeV energy entering the atmosphere will have its first interaction at ≈ 25 km height

[1] Positrons are from now on simply referred to as electrons.

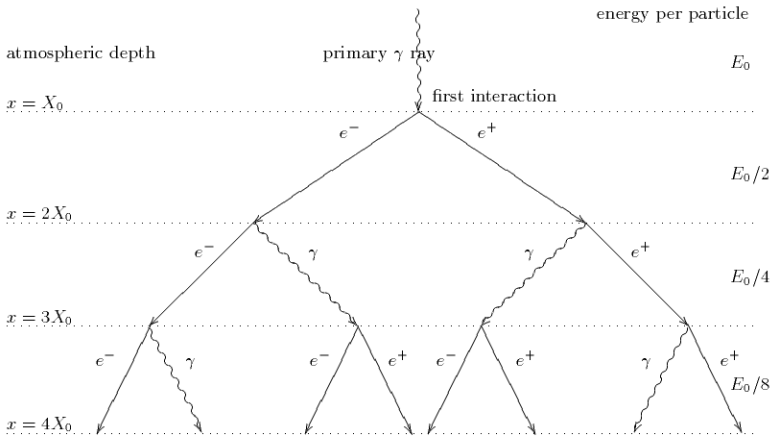

Figure 1.1: Toy model illustrating the electromagnetic shower development according to Heitler.

and will have produced the maximum number of secondary particles at $\approx$ 300 g cm^{-2} atmospheric depth, corresponding to a height of $\approx$ 10 km. The whole cascading process will last for $\approx 50\mu$s. Fig. 1.2 (a) illustrates the longitudinal shower development of a γ ray of 300 GeV energy entering the atmosphere.

1.1.2 Hadronic showers

When a cosmic ray nucleus enters the atmosphere it in-elastically scatters on nuclei in air and produces mesons (e.g. pions and kaons) as well as nucleons and hyperons. These strong force interactions give rise to the development of a hadronic particle shower. However, since the charged and neutral mesons decay into leptons and gammas, also electromagnetic sub-showers emerge and accumulate about $\approx$1/3 of the total primary energy. The electromagnetic shower component loses energy via ionisation of electrons, Bremsstrahlung and pair production, whereas hadronic sub-showers predominantly lose energy due to the production of muons and neutrinos in the decay of charged pions. In some cases most of the primary energy is transformed into a π^0 in one of the first interactions, leading to the development of an electromagnetic particle cascade, even if the incident particle is of hadronic origin. This fact is of relevance in the context of γ/hadron separation which is going to be discussed in more detail in Section 1.3.5.

In general, however, hadronic and electromagnetic air showers show distinct properties which are characteristic for the interaction processes at work during their formation. Due to the conversion of primary energy into the creation of muons and neutrinos as well as the dissipation of energy in nucleonic interactions, the number of charged particles in hadronic showers is about 1/3 of that of a γ ray with same primary energy. That means that a 1 TeV proton produces roughly the same amount of Čerenkov light as a 300 GeV γ ray. At the same time, this proton has a more than twice as large mean free path length compared to the electromagnetic radiation length, namely $\approx 80\,\mathrm{g\,cm^{-2}}$. Hence, hadronic showers do penetrate deeper into the atmosphere and have on average a larger shower

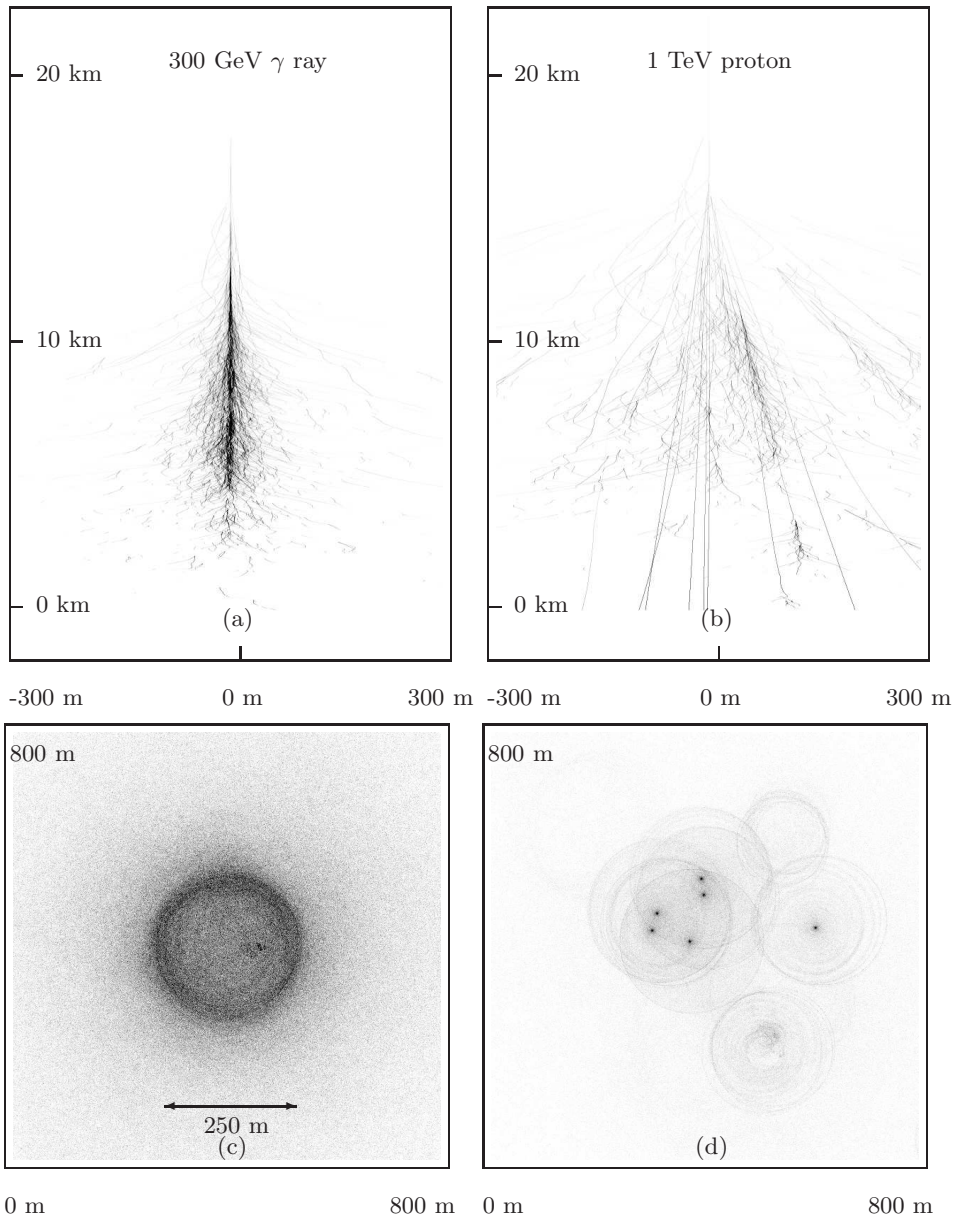

Figure 1.2: Comparison between Čerenkov emission originating from an electromagnetic air shower (a,c) induced by a 300 GeV γ ray and from hadronic shower (b,d) induced by a 1 TeV proton as obtained by Monte Carlo simulations (Bernlöhr 2000). The upper panel depicts the longitudinal development as a projection onto the (x,z) plane, whereas the lower panel depicts the lateral shower development as a projection onto the (x,y) plane.

maximum $X_{\max}$. The lateral extension of an EAS of hadronic origin is determined by the transverse momentum which secondary particles receive during their creation. In case of a electromagnetic cascade the lateral spread is mainly determined by multiple scattering and is in general very small, compared to hadronic showers. This is caused by the inelastic scattering on spatially extended targets via the strong interactions in hadronic showers,

why these transverse momenta are much larger compared to electromagnetic cascades. Whereas complex multi-particle interactions are characteristic for hadronic air showers, electromagnetic showers are dominated by three-particle processes. As a result, hadronic showers show a less pronounced radial symmetry with respect to the shower axis compared to electromagnetic showers (see Fig. 1.2 (c,d)).

1.1.3 Atmospheric Čerenkov light from air showers

At very high energies the majority of the charged secondary particles in the air shower will move with a velocity which is larger than the phase velocity of light in air. Thus, these highly-relativistic particles will emit Čerenkov radiation in a narrow cone with opening angle Θ_c with respect to the primary particle track. Θ_c depends on the velocity of the particle βc and the refractive index n:

$$\cos\Theta_\mathrm{c} = \frac{1}{\beta n}\,. \tag{1.3}$$

By definition $\cos\Theta_\mathrm{C}$ is smaller than 1, why there exists a threshold energy for Čerenkov-light emission. It depends on the particle mass m_0 and the refractive index n:

$$E_\mathrm{min} = \gamma_\mathrm{min}\, m_0\, c^2 = \frac{m_0\, c^2}{\sqrt{1-n^{-2}}}\,. \tag{1.4}$$

With an assumed refractive index of $n_\mathrm{air} = 1.00029$ at ≈ 7.2 km height, electrons moving in air have an E_min of ≈ 21 MeV whereas for protons E_min is ≈ 39 GeV, thus demonstrating that light particles such as electrons dominate the Čerenkov emission in air showers. Since the density of air varies with height, the refractive index and hence the threshold energy and opening angle of the Čerenkov emission vary as well. Light cones emitted by electrons in various heights have opening angles Θ_c of typically $1^\circ - 2^\circ$. This leads to a rather homogeneous light distribution on ground level with Čerenkov-ring radii of 80 m to 120 m. The Čerenkov photons emitted within the cascading process arrive in a very short time window of a few nanoseconds because the cascade basically develops along the Čerenkov-light path.

Emitted Čerenkov photons suffer from multiple Coulomb scattering which leads to a smeared-out light distribution on ground. Additionally, Čerenkov photons encounter scattering and absorption processes, which on the one hand reduce the measurable light intensity on ground level and on the other hand also modify the spectrum of the emitted photons. Due to Rayleigh and Mie scattering especially photons of short wavelength get scattered effectively, whereas photons below 200–300 nm are basically absorbed by the fission of ozon (O_3). These three processes lead to a shift of the peak of the emitted Čerenkov-light distribution from UV wavelengths to the optical blue band. For a 1 TeV γ ray typically just 100 photons per m^2 reach the ground, why large collection areas are necessary to accumulate enough photons to extract information about the shower geometry and the primary particle energy and direction.

1.2 H.E.S.S. instrument and Imaging Atmospheric Čerenkov technique

Currently the most sensitive instruments to detect VHE γ rays from astrophysical sources in the 50 GeV to 100 TeV domain are IACTs. They make use of the atmosphere as a calorimeter and utilise the imaging atmospheric Čerenkov technique to extract information about the incident primary particle by means of Čerenkov light emitted by secondary particles in the initiated EAS. Imaging comes into play when the Čerenkov photons, which are spread over an area of $\sim 10^5$ m^2 on ground, get focused with large mirrors onto a fast, optical camera operating on nanosecond timescales. The first system which utilised this technique was a single 10 m dish telescope operated by the Whipple collaboration. They detected the first VHE γ-ray source, the Crab nebula, two decades ago in 1989 (Weekes et al. 1989). The next step in technology was the installation of multi-telescope arrays like e.g. the HEGRA system in 1996 (Fonseca 1998). Such systems made use of the stereoscopic principle which has proven to be a very efficient way to lower the energy threshold[2] and to improve the shower reconstruction. This is mainly attributed to the fact that showers seen from different directions provide more information about their geometry, origin and energy, which can then be used for a more accurate reconstruction and improved γ/hadron separation. Telescope systems of the 3$^{\text{rd}}$ generation like e.g. H.E.S.S. (Hinton 2004), MAGIC (Lorenz 2004), VERITAS (Weekes et al. 2002) and CANGAROO-III (Kubo et al. 2004) utilise or plan to utilise the successful stereoscopic approach. While current telescope systems typically consist of 2 to 4 telescopes, large arrays comprised of $\mathcal{O}(20-200)$ telescopes are currently under study and going to be constructed within the next $10-15$ years[3]. These large arrays aim for an order of magnitude better sensitivity in a wider energy range and will achieve a much better angular resolution to avoid the problem of source confusion. In this section, the imaging atmospheric Čerenkov technique is discussed in more detail, before one of the world-wide leading IACTs, H.E.S.S., is presented.

1.2.1 Imaging Atmospheric Čerenkov technique

The IACT principle, which has demonstrated to be very successful in many aspects of VHE γ-ray astronomy, is going to be discussed in more detail in the following. To extract the information of the primary particle, which is inherently stored in the air shower, a telescope comprised of an array of large mirrors and a fast, optical camera is placed into the Čerenkov-light pool. The spherical or parabolic mirrors with typical areas of $\mathcal{O}(100)$ m^2 redirect the collected Čerenkov photons onto a pixelized camera placed in their focus. To be able to record the short light flashes, a photo-multiplier-tube (PMT) based camera is desirable since PMTs provide the required nanosecond resolution. The mapping principle allows to resolve and image the air shower and its spatial intensity distribution, thereby allowing to reconstruct important properties of the primary particle, such as e.g. its energy or incident direction.

[2] Less random triggers from night-sky background (NSB) photons allow to lower the pixel threshold and less muons are recorded, when requiring a two-telescope trigger.

[3] The optimum number of telescopes is currently evaluated in the design studies of the CTA (Hermann et al. 2008) and AGIS (Fegan et al. 2008) consortia.

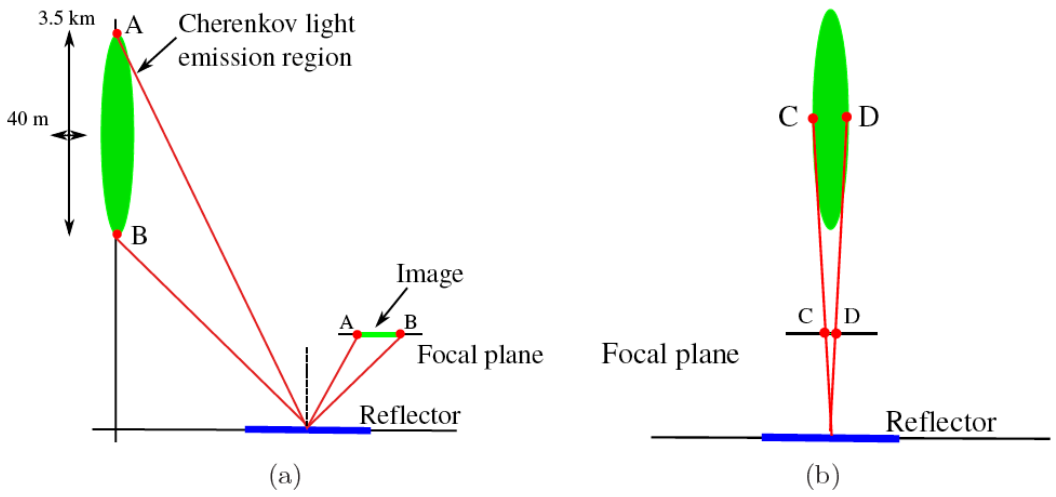

Figure 1.3: Sketch illustrating the principle of imaging an air shower onto a camera. (a) Mapping of the shower axis into the focal plane of a telescope. The orientation of the image depends on the inclination of the shower with respect to the telescope optical axis. (b) Shower as seen from the telescope position. The lateral spread of the shower translates into the width of the image in the camera. Image taken from Hoppe (2008).

Figure 1.3 illustrates the principle of imaging an air shower onto a camera. From representation 1.3 (a) it gets clear that the distance between the shower- and the reflector axis affects the position of the image in the camera. Furthermore, the major image axis points back to the origin of the primary γ ray, i.e. the *shower direction*, on the sky. Based on the telescope positions on ground, the major axis of the shower image in the camera plane points to the extrapolation of the primary particle course to the ground, i.e. the *shower impact position*. Depending on the inclination of the shower axis with respect to the telescope pointing direction the length of the shower image changes. Fig. 1.3 (b) illustrates how the lateral Čerenkov-light distribution translates into the width of the shower image. For a γ ray, the lateral shower extension is rather small and resembles an elliptically shaped camera image. Due to the aforementioned interaction processes, hadron induced showers in general exhibit a rather irregular lateral shape compared to γ-induced showers. Hence, their images are more irregular as well and they can be distinguished by their width from images of electromagnetic particle showers on a statistical basis. Furthermore, from the total recorded image intensity and the distance between the telescope and the reconstructed shower impact point, the energy of the primary particle can be estimated. Even though there exists an 180° ambiguity in the reconstructed direction of the primary particle, already with a single shower image, basic primary particle properties can be extracted utilising the imaging atmospheric Čerenkov technique.

By placing a second telescope into the Čerenkov-light pool, a stereoscopic viewing of the particle cascade from different directions allows to collect additional information about the shower geometry. Viewing the air shower from different sides improves the reconstruction of the incident particle direction and leads to an improved angular resolution of the instrument. Furthermore, the irregularity of hadronic particle cascades is more easily explored

Figure 1.4: H.E.S.S. telescopes during daytime.

with multiple telescopes, thus leading to a better γ/hadron separation.

1.2.2 The H.E.S.S. instrument

H.E.S.S. site

The High Energy Stereoscopic System – H.E.S.S.– is an array of four imaging atmospheric Čerenkov telescopes located in the Khomas Highlands of Namibia, 1800 m above sea level (23°16′17″S, 16°29′58″). Situated 100 km away from the Namibian capital Windhoek, the area close to the Gamsberg is well known for its outstanding astronomical conditions (Wiedner 1998) with ∼54% of the moon-less nights being cloudless with humidity of less than 90%. Additionally, the location of the H.E.S.S. array in the southern hemisphere makes this site perfectly suited for the study of a large number of potential VHE γ-ray sources located in the Milky Way, such as e.g. SNRs.

Array layout

The installation of the full four-telescope array started with the construction of the first H.E.S.S. telescope in summer 2002 and was completed in December 2003, when the last telescope started data taking. Figure 1.4 shows the H.E.S.S. array as of summer 2008 with all four telescopes during daytime. The four telescopes are arranged on a quadratic grid with 120 m side length. This separation is a compromise between a large light collection area with good stereoscopic viewing conditions on the one hand and the limitation due to the typical Čerenkov-light cone radius for γ rays of ≈120 m on the other hand. A larger spacing between telescopes would result in a significantly reduced number of multi-telescope triggers.

(a) (b)

Figure 1.5: (a) One of the H.E.S.S. telescopes with mirrors, mirror support structure and camera. (b) Maintenance of a camera inside the camera hut.

Mirrors and mirror support structure

All four telescopes are identical in construction and comprised of basically three main components: a camera, mirrors and a mirror support structure. The mirror support structure has a diameter of 13 m and accommodates 382 spherical mirrors, each with a diameter of 60 cm. The mirrors are made of ground glass and have been aluminized and quartz-coated in a second production step to obtain an optical reflectivity of ≈80% at blue wavelengths of ≈330 nm. Together, they add up to a total reflector area of 107 m^2. The mirror segments are arranged on a sphere of 15 m radius, the focal length of the telescope, on a Davies-Cotton reflector (Davies & Cotton 1957) of hexagonal shape. The Alt-Az mount rotates on a steel rail of 13.6 m diameter with a maximum speed of 100°/min. Thereby the telescopes can track any target position on the sky within less than three minutes. Since the telescope design aimed for the maximum possible rigidity, the total weight of the mirror support structure is 60 tons. However, the pointing accuracy of the telescopes is mainly limited by deformation of the supportive frame and the bending of the camera arm. Deep studies helped to understand these bending effects and to correct for them, thereby reducing the total systematic pointing error from ≈ 30″ to ≈ 9″ for observations where such an accuracy is desired (van Eldik et al. 2008). Figure 1.5(a) illustrates the design of a H.E.S.S. telescope.

Camera

The Čerenkov-light flashes of air showers last for just a few nanoseconds which makes it necessary to record the emitted photons with a camera of similar exposure time. The use of photo-multiplier tubes (PMTs) guarantees this very fast response and the desired sensitivity. The PMTs are organised in an hexagonal array of 960 pixels, each covering an area of 0.16° and with a read-out window of 16 ns. To reduce Čerenkov-light losses, Winston cones installed in front of the PMTs concentrate the Čerenkov light onto their active areas. They furthermore shield them against stray- and background light. The large field-of-view of 5° in diameter allows to resolve spatially extended sources. The camera is

organised in 60 drawers, each retaining a group of 16 PMTs and every drawer housing the high voltage supply of its PMTs, the trigger and read-out electronics. In Fig. 1.5(b) one of the four cameras with the PMTs in the hexagonal design is shown.

Trigger

The H.E.S.S. trigger system is separated in two levels, a camera trigger on single telescope level and a system-wide second level, the *central trigger system*. On the first level, the cameras are divided into 64 overlapping sectors which release a trigger if more than five pixels within 1.5 ns in one sector detect a signal of more than four photo-electrons (p.e.). Depending on the zenith angle of the observation this first level trigger occurs with a rate of a ≈300–500 Hz. As soon as one of the telescopes fulfils this trigger criterion, a signal is sent to the central trigger via an optical cable. If the central trigger receives within 50 ns a second trigger from one of the other telescopes, the information stored in every pixel of the triggered telescopes is read out and stored on data tapes in a computer farm. The coincidence trigger allows to effectively reduce the rate at which the telescope system records random NSB triggers. Furthermore, this multiplicity criterion reduces the number of single muon triggers already on the hardware level. Thereby, H.E.S.S. achieves a low trigger threshold of ≈ 100 GeV. The system trigger rate depends on the zenith angle of the observation and is of the order of 150–250 Hz.

1.3 H.E.S.S. data analysis

This section deals with the standard data analysis frame of H.E.S.S.. The subsequent steps starting from data taking over calibration, image processing to the point of background reduction and γ/hadron separation are discussed in more detail.

1.3.1 Data taking

H.E.S.S. is operated just during moon-less nights for data taking. The moon as additional light source would hamper the detection of the very faint Čerenkov-light flashes and hence higher the trigger threshold of the telescope system from ≈100 GeV to a few 100 GeV–1 TeV[4]. The data is recorded in bunches of 28 min long *(observation) runs* in which a given object or sky position is tracked by the telescopes. The data is stored on data tapes and gets shipped to Heidelberg (Germany) and Lyon (France) for further data analysis every four weeks. The total available dark time amounts to ≈ 1700 hours per year and is split more or less equally between observations of Galactic and Extragalactic objects.

[4] However, other IACTs, like MAGIC and VERITAS have successfully performed observations during moon-time at the expense of an increased energy threshold (MAGIC Collaboration 2007; Aliu et al. 2008; Wagner et al. 2009).

1.3.2 Data preparation

In a preparatory step, the recorded raw data has to pass some quality criteria and needs to get calibrated for further image analysis. Only data taken under stable weather conditions and with functioning hardware components are used for further data analysis. 'Good weather' in this regard is defined using cuts on the stability of the system trigger rate to exclude data where clouds passed through the f.o.v.. Additionally, a cut on the absolute trigger rate of the system excludes data, where e.g. dust or haze reduced the transparency of the atmosphere during observations. To assure that no artefacts are introduced in the event reconstruction, telescopes where more than 10% of the pixels in the camera were turned off due to bright stars, meteorites or technical problems get excluded from further data processing. Additionally, it is required that other hardware components like e.g. the tracking or trigger system behaved in a suitable way. Apart from these run-by-run variations of the telescope system and varying weather conditions, a long-term variability of the H.E.S.S. system response is apparent. Since the optical reflectivity of the mirrors degrades on timescales of years, one has to correct for the loss in reflectivity on a telescope basis. An efficient way to estimate the optical efficiency of single telescopes is based on muon images in hadron-induced air showers. Bolz (2004) has shown that the radius of the ring-shaped muon image and the light yield in the produced muon ring can be used to get an absolute calibration of the optical reflectivity of the mirrors.

All telescopes marked as good from observation runs taken under stable weather conditions and with properly working hardware are then used to reconstruct shower properties from the recorded EAS images. Beforehand, images get calibrated according to the H.E.S.S. standard calibration procedure (Aharonian et al. 2004b). Since the EAS images mostly contain pixels with NSB photons, those have to be excluded in an image cleaning procedure. For this purpose, just pixels which stored an intensity of 10 p.e. and have a neighbouring pixel with more than 5 p.e. (and vice versa) are kept for shower reconstruction. Additionally, pixels with intensities less than 3σ away from the pedestal RMS value are rejected. The resulting cleaned image consists of spatially connected pixels which depict the projected two-dimensional extended air shower intensity distribution. As visible from Fig. 1.2 (a,b), electromagnetic EAS exhibit a rather regular shape with a small lateral extension, whereas hadron-induced showers show a more irregular and diffuse structure. This behaviour is also clear from Fig. 1.6, where the pixel intensity distribution in the camera is shown for a VHE γ-ray-induced and proton-induced air shower before the image cleaning procedure has been applied.

1.3.3 Event reconstruction

γ-ray induced shower images obviously exhibit an elliptical shape and can be described by the first and second moments of an ellipse. This representation was first introduced by Hillas (1985), and therefore the parameters are also referred to as *Hillas parameters*. The first moment comprises the position of the ellipse or *centre of gravity* (COG), whereas from the matrix of second moments one obtains the length of the minor and major axis of the image, the *width* and *length* parameter, as well as its orientation ϑ. An additional quantity used in the reconstruction is the total intensity stored in the ellipse (*size* parameter). A schematic view of the Hillas parameters can be found in Fig. 1.7.

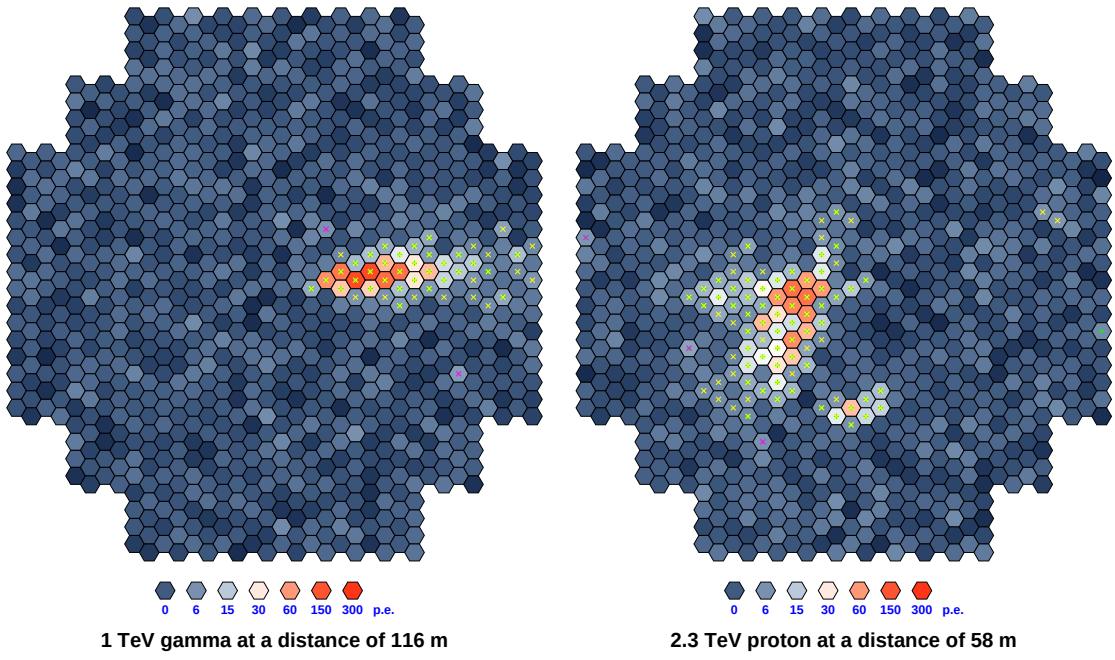

(a) (b)

Figure 1.6: Čerenkov-light distribution in the camera for a simulated γ-ray of 1 TeV energy (a) and for a simulated proton of 2.3 TeV energy (b). Pixels store intensities of up to 300 p.e. Pixels with an intensity of more than 5 p.e. or 10 p.e. are marked with a yellow and/or green cross and pixels which do not pass the pedestal RMS criterion are marked with a purple cross.

These five quantities inherently store information about the shower geometry, its spatial intensity distribution and information about the origin and energy of the primary particle. *Width* and *length* of the shower images contain information of the interaction processes at work during the shower development and can be used for γ/hadron separation. On the other hand is the *size* of the shower image connected to the primary particle energy. Combining the positional information COG and ϑ from multiple telescopes allows to geometrically reconstruct the incident direction and the shower impact point on ground.

As soon as a shower is observed with multiple telescopes from different directions, each pair of major image axes can be intersected in a common coordinate system[5] to obtain the shower direction. In case N telescopes are reconstructing the direction, all $N(N-1)/2$ possible estimated directions get weighted by the sine of the stereo angle between image axes, the ratio of *width* over *length* and by the *size* of the shower image. Thereby the fact is taken into account that bright, elongated images that are observed under larger angles allow a more precise determination of the shower direction. By averaging over all estimated positions, the final shower direction can be calculated. With this geometrical method[6] the achieved accuracy of the direction reconstruction is better than $\approx 0.1^\circ$ per

[5] This is the coordinate system in which all cameras are overlaid and which is perpendicular to the telescope pointing directions.

[6] The geometrical approach was introduced by Hofmann et al. (1999) as Algorithm 2.

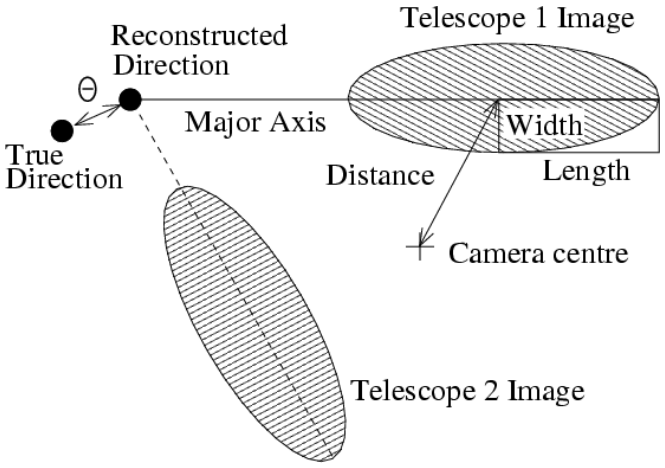

Figure 1.7: Sketch illustrating the Hillas parametrisation of a γ-ray induced air shower detected in two telescopes. Width and length as well as the distance between camera centre and *COG* are later used in the analysis to select γ-ray like events. Intersecting the major axes in a common coordinate system allows to reconstruct the shower direction on the sky as well as the shower impact point on ground (see text for further details). The Figure was taken from (Aharonian et al. 2006a).

event. The shower impact position on ground is reconstructed in a similar fashion but in an array-wide coordinate system with the telescope positions as reference. Also here the accuracy of the reconstruction is remarkable with less than ≈10 m for showers with impact distances of < 200 m away from the array centre. Additionally, the *length* and *COG* parameters provide information about the shower maximum X_{max}, which is also reconstructed stereoscopically. The geometrical reconstruction approach is illustrated in Fig. 1.7. The overall reconstruction accuracy can be further improved by taking into account not only the *width* over *length* ratio, the *size* and angle between shower images, but else the errors on all Hillas parameters. This approach corresponds to Algorithm 3 introduced by Hofmann et al. (1999) but is not utilised in this work.

The energy of the primary particle is – for constant zenith angle, distance between reconstructed shower direction and camera centre (this distance is henceforth referred to as *offset*) and for a given shower impact distance to the telescope – to first order linearly dependent on the measured *size* of the corresponding shower image. In contrast to the direction reconstruction, where the shower images stored all the necessary information needed for reconstruction, the energy reconstruction needs further input from Monte Carlo γ-ray simulations. For every reconstructed distance, *offset*, *size* and zenith angle of an event, look-up-tables filled with Monte Carlo γ-ray simulations are used to predict the primary particle energy under the a γ-ray hypothesis. Since the optical efficiency of the telescopes change with time, the simulated optical efficiency has to be scaled to the actual optical efficiency of the telescopes. This is done on the basis of muon images as discussed in Section 1.3.2. The energy resolution obtained with this method is on average $\mathcal{O}(15\%)$. However, the resolution changes with primary particle energy. Shower images of small intensity originate in general from showers of smaller energy which experience larger shower fluctuations. Hence, this results in a worse energy resolution for such events.

1.3.4 Shower shape parameters

As mentioned above, the shape of the shower images depends on parameters such as e.g. the zenith angle of the event, its distance to the telescope, *offset* and energy. Hence, a single shower seen from different sides has a different shape in every participating telescope. To discriminate the dominant component of hadron-induced air showers with on average broader and more irregular images compared to the elliptically-shaped γ-ray induced showers, the H.E.S.S. Standard Analysis follows the *mean reduced scaled width* approach explained by Aharonian et al. (2006a). For an image of given *offset*, impact distance, *size* and zenith angle, the measured width W_i is compared to the width $< W_i >$ as expected from Monte Carlo γ-ray simulations yielding the *reduced scaled width* RSW_i for telescope i:

$$RSW_i = \frac{(W_i - < W_i >)}{\sigma_i} \ . \tag{1.5}$$

Here, σ_i is the spread of the width as obtained from Monte Carlo γ-ray simulations $< W_i >$. To be independent of the number of telescopes which recorded an air shower, one estimates the *mean reduced scaled width* MSW by averaging the RSW over all participating telescopes:

$$MRSW = \frac{1}{\sum\limits_{i \in N_{tel}} \omega_i} \cdot \sum_{i \in N_{tel}} (RSW_i \cdot \omega_i) \ . \tag{1.6}$$

The spread in expected width is taken into account by introducing a weighting factor ω_i, which is defined as $\omega_i =< W_i >^2 / \sigma_i^2$. The *mean reduced scaled length* $MRSL$ is calculated in a similar way and used for γ/hadron separation as well. Like the reconstructed energy, also the expected width and length values are obtained from look-up-tables. These are filled with Monte Carlo γ-ray simulations for a range of zenith- and *offset* angles, reconstructed impact distances and *size* values. Compared to the application of telescope-wise cuts on the image shape parameters, the averaging approach has several advantages. First of all, statistical fluctuations of image shape parameters are included in the estimation of the *MRSW* (*MRSL*). Moreover, hadron-induced showers, which look from one side like an electromagnetic cascade and from another side like a hadronic cascade, can be effectively suppressed. The viewing from different directions makes their classification easier and constitutes one of the big advantages of ground-based IACTs using the stereoscopic approach. Fig. 1.8 shows the *MRSW* and *MRSL* parameter distributions for Monte Carlo γ rays, Monte Carlo protons and *Off data*. *Off data* is obtained from observations of sky regions without any γ contamination and therefore consists of dominantly hadronic cosmic rays, thus background events. The difference between Monte Carlo protons and *Off data* can be understood by the cosmic-ray composition. Heavier nuclei exhibit larger shower fluctuations during the cascading process, which leads to even more irregular shower images compared to protons. As a consequence, shower shape parameters are on average larger.

1.3.5 Event selection

After the shower geometry has been reconstructed and the primary particle properties have been estimated, one has to effectively reduce the vast hadronic background in the data. This background is a factor of $\mathcal{O}(10^3)$ larger compared to the number of γ rays from

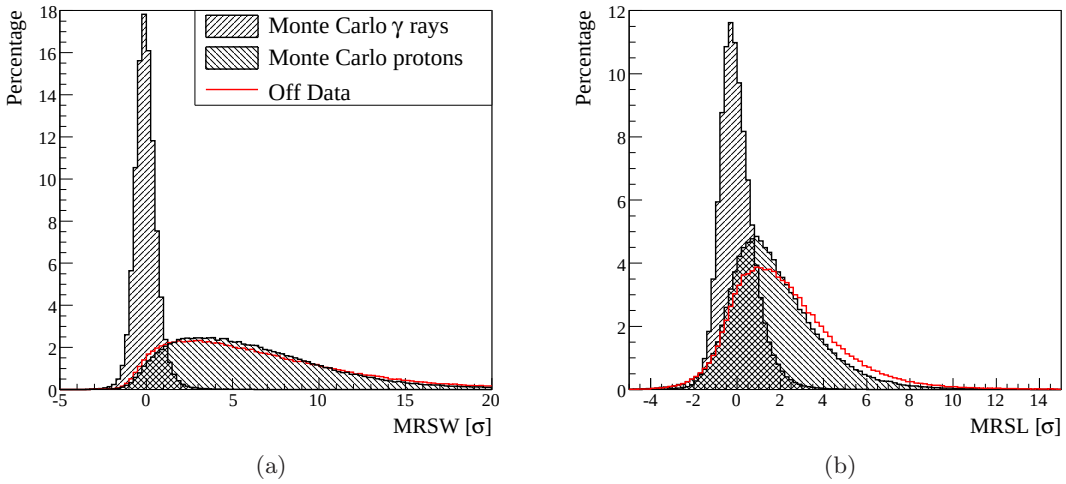

Figure 1.8: (a) *MRSW* and (b) *MRSL* distribution of Monte Carlo γ rays and Monte Carlo protons simulated at a zenith angle of 20° compared to *Off Data* at zenith angles of $15° - 25°$. Shown are all events which pass the *size* cut and the *local distance* cut of configuration *standard* in the H.E.S.S. Standard Analysis. See text and table 1.1 for further details.

the strongest steady know γ-ray emitting objects. The application of cuts to select γ-ray like events in the H.E.S.S. Standard Analysis is performed in two stages:

- ◇ In the *Preselection*, a cut on the minimum image *size* guarantees that showers can be properly parametrised. Furthermore, a cut on the maximum distance between the *COG* and the camera centre (*local distance* cut) rejects images that are truncated close to the camera edge. Considered in the analysis, they would result in misreconstructed shower directions and underestimated primary particle energies.

- ◇ Direction reconstruction is performed for all events for which two or more telescopes fulfil the *Preselection* conditions. For those events, the shower shape parameters are estimated. As obvious from Fig. 1.8, there is an enormous separation potential between γ-induced and hadron-induced air showers just from the image shape parameters introduced in Section 1.3.4. Therefore, a cut on *MRSW* and *MRSL* applied in the *Postselection* step effectively reduces the hadronic contribution. Since the cosmic-ray background events arrive at Earth isotropically, a cut on the distance between the assumed source position and the reconstructed shower direction (this distance is henceforth referred to as θ) can further suppress the hadronic background for point-like sources.

Depending on the assumed source spectrum and strength, two sets of selection cuts are applied in the H.E.S.S. Standard Analysis. They simultaneously optimise cuts on the *size* of the shower images and the *MRSW*, *MRSL* and θ^2 parameters to obtain the maximum significance per observation time. The *standard* cuts are optimised for a source of 10% of the integrated flux of the Crab nebula above 200 GeV and with an energy distribution $\mathrm{dN/dE} \sim \mathrm{E}^{-\Gamma}$ with spectral index $\Gamma = 2.6$ (Aharonian et al. 2004a). They are used for

Configuration	*MRSW* Max σ	*MRSL* Max σ	θ^2_{cut} Max (deg^2)	Size Min (p.e.)
standard	0.9	2.0	0.0125	80
hard	0.7	2.0	0.01	200

Table 1.1: Selection cuts optimised for Configuration *standard* (strong, steep spectrum sources) and *hard* (weak, hard spectrum sources) for the H.E.S.S. Standard Analysis. Minimum cuts on *MRSW* and *MRSL* of -2.0 are applied for both configurations (Aharonian et al. 2006a).

spectral analysis since they provide a lower energy threshold and more γ-ray statistics. This is achieved at the expense of a lower signal-to-noise (S/N) ratio. The *hard* selection cuts are optimised for a source with spectral index $\Gamma = 2.0$ and a flux of 1% of the integrated Crab flux above 200 GeV (Aharonian et al. 2004a). They are commonly used for morphological studies since they provide a smaller point-spread-function (PSF) and better S/N ratio. However, these improvements are achieved at the expense of lower γ-ray statistics and a higher energy threshold.

1.3.6 Limitations of the shower shape cuts

Cuts on the aforementioned shower shape parameters have proven to effectively reduce the hadronic cosmic-ray background independent of the observational conditions and primary particle energies. However, it is clear that the Hillas parametrisation just employs global shower properties, such as the width and length of the images. Shower properties on the pixel level are not taken into account by the Hillas approach. Also the stereoscopic information is not fully employed by the $MRSW$ and $MRSL$ parameters. As mentioned in Section 1.1.2, the subclass of hadronic cosmic rays, which transfer most of their energy into the electromagnetic part of the shower are not easily distinguishable from γ-ray induced showers. Information stored in the image shape parameters is not sufficient to identify this class of background events. However, there is some potential to discriminate those by using the shower maximum $X_{\max}$ as a discriminating parameter.

In the next chapter not only the shower maximum but also additional parameters with classification power are introduced and combined in a multivariate analysis method which is based on decision trees. The applicability of this approach and its enormous potential in terms of γ/hadron separation is demonstrated. Moreover, the improvement in sensitivity due to additional parameters and due to the method are examined separately.

2 Improved γ/hadron separation using a multivariate analysis technique

As shown in Chapter 1, cuts on the *MRSW* and *MRSL* parameters can suppress a large fraction of cosmic-ray background events. This approach has proven to be robust and has been successfully applied in the analysis of H.E.S.S. data. H.E.S.S. scanned the inner parts of the Milky Way and established more than ~ 50 new sources of different type as VHE γ-ray emitters, such as e.g. SNRs, PWNe or γ-ray binaries. VHE γ-ray emission was also detected from extragalactic objects such as Active Galactic Nuclei (AGN) or Radio galaxies (see e.g. Hinton & Hofmann 2009, for a recent review). All these sources emit VHE γ rays at a flux level, which made their detection possible with H.E.S.S. within observation times of 25 hours or less – a significantly smaller amount of time than the available dark time per year of $\approx$1700 hours. However, after five years of operation, H.E.S.S. is now getting into the regime, where presumably all strong VHE γ-ray sources have been detected and where a significantly larger amount of observation time is needed to establish weaker sources as VHE γ-ray emitters. Especially extragalactic objects such as Starburst galaxies or Galaxy clusters and Galactic objects such as colliding wind binaries (CWB) are predicted to emit γ rays at a flux level which is right at the edge or slightly below the H.E.S.S. sensitivity[1]. In order to increase the sensitivity of IACT systems, additional telescopes, spread over a larger area on ground are needed. The next generation of ground-based VHE γ-ray telescope systems is currently being studied by the CTA (Hermann et al. 2008) and AGIS (Fegan et al. 2008) consortia and will start operation within in the next $10 - 15$ years.

Still, the sensitivity for existing instruments can considerably be improved by an increased background reduction. Compared to the Hillas approach which utilises the two-dimensional shape of the recorded EAS images in the camera for shower reconstruction and γ/hadron separation, more elaborated analysis methods have been developed and successfully employed. The *3D Model Analysis*, introduced by Lemoine-Goumard et al. (2006), compares the recorded images with a three-dimensional photosphere model of the shower, achieving a similar performance as the H.E.S.S. Standard Analysis. Beyond that, the application of multivariate analysis (MVA) techniques, such as Random Forests (RF) (Breiman 2001), have been studied and successfully applied to a single IACT recently (Bock et al. 2004; Albert et al. 2008). RFs have also been utilised in H.E.S.S., in an analysis especially designed for the study of cosmic-ray electrons (Egberts 2005, 2009). The H.E.S.S. result, presented in Aharonian et al. (2008a), had strong impacts on the field of dark matter physics and was highly regarded in the astronomical and physics community.

In this chapter the application of the *Boosted Decision Tree* (BDT) method (which is

[1] Here, sensitivity is defined as the minimum flux F_γ emitted by a source which is measured on Earth as signal N_γ at a given confidence level.

integrated in the TMVA package (Hoecker et al. 2007)) to data obtained by H.E.S.S. is discussed. The method presented in the following can be applied for γ/hadron separation and the study of VHE γ-ray sources, independent of the number of telescopes. Beyond the first performance studies of a telescope-independent, decision-tree-based γ/hadron separation in ground-based VHE γ-ray astronomy, presented in Ohm (2007), this work focuses on a thorough systematic study of shower shape parameters with classification potential and their integration in the BDT method, taking into account the dynamical properties of the recorded data such as the zenith angle or event energy (Section 2.1). The basic working principle of the BDT and its advantages compared to other MVA methods is discussed in Section 2.2, before in Section 2.3 the training and evaluation of the BDT method is described. Section 2.4 presents detailed systematic tests using H.E.S.S. data based on observations of several astrophysical objects. Finally, the performance and increased sensitivity of the BDT approach using Monte Carlo γ-ray simulations and background data is discussed in Section 2.5[2].

2.1 Parameters with γ/hadron separation potential

In the H.E.S.S. Standard Analysis cuts on the shower shape parameters *MRSW* and *MRSL* are applied to select γ-ray like events and to reject the hadronic background. The separation potential is illustrated in Fig. 2.1(a), where the distribution of the two parameters is shown for Monte Carlo γ rays and *Off data*. Although the application of these *box cuts* suppresses a large fraction of the charged cosmic rays, they apparently do not fully explore the available information stored in the two parameters. An improvement could already be achieved, if a cut on *MRSW* as a function of the *MRSL* value would be applied.

Apart from these two shower shape parameters, which utilise the *width* and *length* of the EAS image in the camera, more information about the shower origin, its spatial intensity distribution and interaction processes during the shower development are stored in the recorded images. In this section, additional shower shape parameters which are based on the Hillas parameters and have γ/hadron separation potential are introduced and their properties are investigated. These parameters are then fed into the BDT algorithm, which is presented in Section 2.2.

2.1.1 Classifying variables

Similar to the *MRSW* and *MRSL* parameters do the variables discussed in the following take advantage of the stereoscopic approach and are either defined as average value over all telescopes considered for reconstruction[3] or they are reconstructed stereoscopically, combining the information from multiple telescopes which have recorded a single EAS, in one number. Thereby, the classifying variables are independent of the number of telescopes which have recorded an EAS and can be used to describe events of different multiplicity.

The classifying variables which are later used for the training of the BDT are introduced

[2] The studies presented in the following are summarised in the paper: "γ/hadron separation in Very-High-Energy γ-ray astronomy using a multivariate analysis method" (Ohm et al. 2009b).
[3] Where the number of considered telescopes is also referred to as *multiplicity*

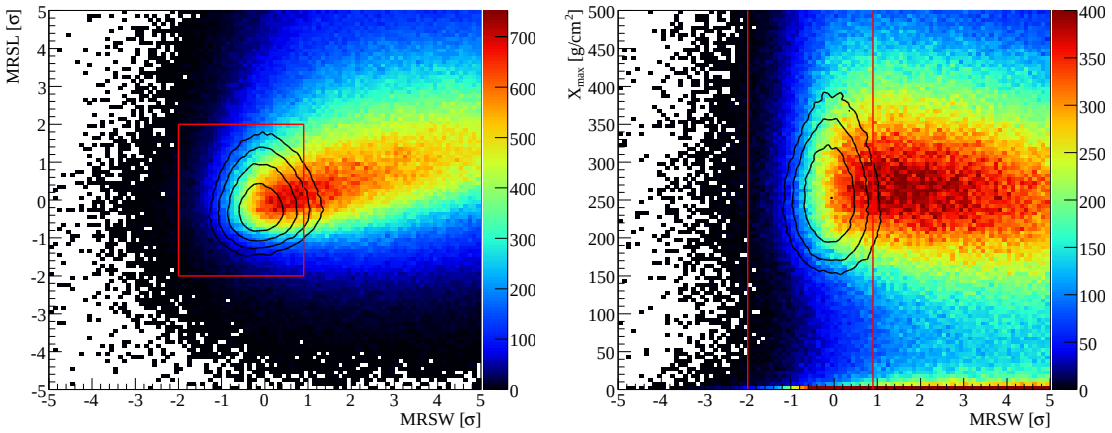

(a) (b)

Figure 2.1: Distribution of (a) *MRSL* versus *MRSW* and (b) X_{max} versus *MRSW* of hadronic cosmic rays in the $15-25°$ zenith angle range (colour scale) and Monte-Carlo γ rays simulated at 20° zenith angle with an offset of 0.5° (black contours). Indicated as red lines are the shower shape cuts applied in the H.E.S.S. Standard Analysis to select γ-ray-like events. Note the large population of cosmic rays with reconstructed shower maxima ($0 \leq X_{max} \leq 150$) g cm^{-2} and $X_{max} \geq 400$g cm^{-2} which do not get excluded by the *MRSW* cut.

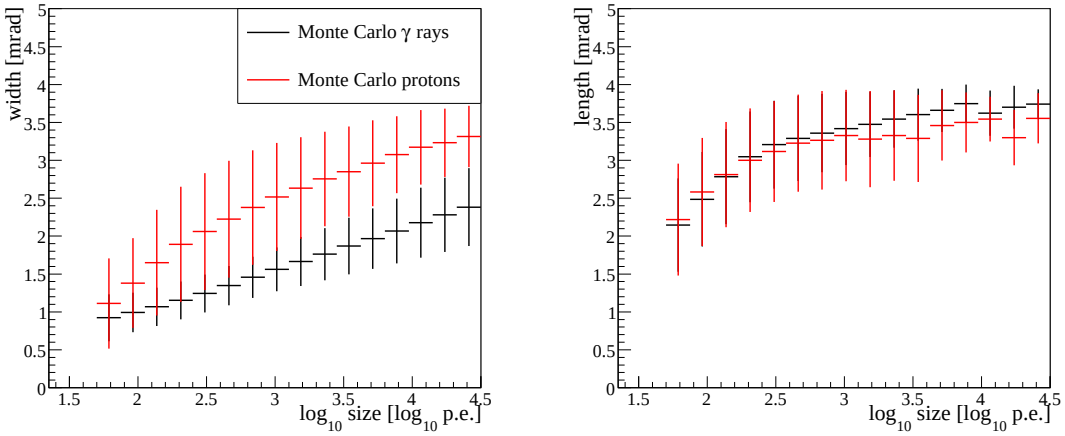

(a) (b)

Figure 2.2: Profile of (a) *width* versus $\log_{10}$(*size*) and (b) *length* versus $\log_{10}$(*size*) of Monte Carlo γ rays and Monte Carlo protons, both simulated at 20° zenith angle. Error bars denote the spread of the corresponding distribution (Figure adapted from Ohm 2007).

in the following:

◇ One type of variables is based on the shower shape parameters introduced in Section 1.3.4. They are calculated as the weighted average difference between the mea-

sured width (length) of an image of given *size* and corresponding impact distance and the expectation for a hadronic event (instead of a γ ray as done in the H.E.S.S. Standard Analysis). According to the $MRSW(L)$ parameters are the *mean reduced scaled width off* ***MRSWO*** and *mean reduced scaled length off* ***MRSLO*** parameters defined as the average $RSWO$ and $RSLO$ over all triggered telescopes:

$$MRSWO = \frac{1}{\sum\limits_{i \in N_{tel}} \omega_i} \cdot \sum_{i \in N_{tel}} (RSWO_i \cdot \omega_i) \ . \tag{2.1}$$

ω_i is a weighting factor which takes into account the spread in expected width (length) of the *Off data* in a particular look-up bin (see also Section 1.3.4). Introducing these two quantities provides information about the separability of gammas and hadrons of given image *size*. From Fig. 2.2 it gets clear, that for images of small intensity, the expected width as obtained from proton and gamma simulations is not very different. However, for increasing image sizes, the expected width for a proton and a gamma significantly differ and the two distributions are more and more separable.

- ◇ The radiation length of hadrons is on average larger compared to the radiation length of electrons and photons (see also detailed discussion in Section 1.1.2). Hence, hadronic cosmic rays penetrate deeper into the atmosphere and have on average a larger $\mathbf{X}_{\max}$. Because of the non-regular structure of hadronic showers and their not well defined Hillas parameters which are used for the stereoscopic reconstruction of X_{max}, the spread in reconstructed shower maxima is larger for hadrons compared to VHE γ rays. This behaviour is illustrated in Fig. 2.1(b) where the large spread in X_{max} for hadronic showers is clearly visible. Also note the population of hadronic showers (and the lack of γ-ray showers), for which X_{max} was badly reconstructed, resulting in values close to 0.

- ◇ Especially the stereoscopic viewing of showers can be further used to examine the shower structure for irregularities in the Čerenkov light distribution caused by weak- and strong-force interactions in hadron-induced EAS. Since the energy of a incident particle in the H.E.S.S. Standard Analysis is reconstructed for every telescope independently, the aforementioned irregularities in the shower shape would lead to a larger spread in the reconstructed energy for a hadronic cosmic ray. Therefore, the $\mathbf{\Delta E/E}$ parameter, expressed as the average spread in reconstructed energies over all participating telescopes, provides additional γ/hadron separation potential.

Fig. 2.3 illustrates the distribution of variables introduced before using the example of Monte Carlo γ-ray simulations and *Off data* for primary particle energies of 0.5 TeV $\leq$ E $\leq$ 1.0 TeV and zenith angles of $(15 - 25)^\circ$. Clearly, all parameters show a more or less pronounced γ/hadron separation potential which can be utilised for background reduction in the analysis. Their properties are examined in the following in more detail.

2.1.2 Properties of classifying variables

The aim of any classification procedure in ground-based VHE γ-ray astronomy is to guarantee a stable γ-ray selection efficiency over the dynamical range of the telescope system.

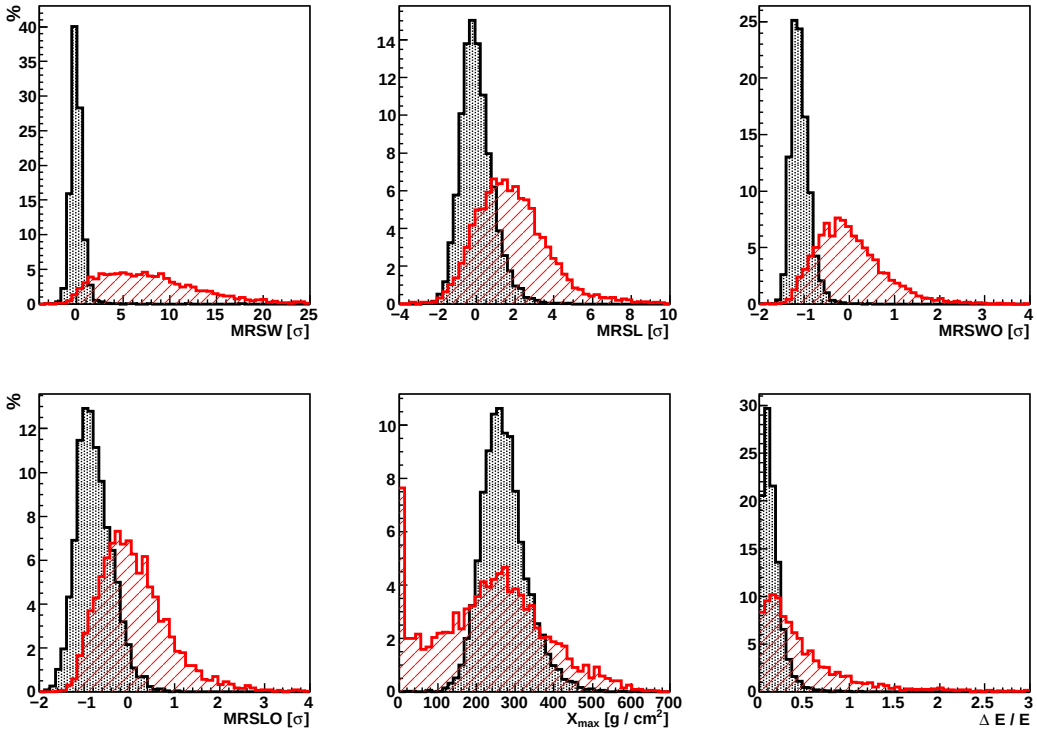

Figure 2.3: Distribution of variables with γ/hadron separation potential for reconstructed energies between $(0.5 - 1.0)$ TeV in the zenith angle range $(15 - 25)^\circ$ for Monte Carlo γ-rays (black) and cosmic-rays from *Off data* (red).

In the case of the H.E.S.S. Standard Analysis it was shown by Berge (2006), that the *MRSW* and *MRSL* parameters are well behaved for all zenith and offset angles. The distributions are centred around 0 and have just a slightly increasing Gaussian width for increasing zenith angles. For this reason, cuts on these two parameters lead to a stable γ/hadron separation for varying zenith and offset angles.

Fig 2.4 illustrates the zenith dependence of the mean and Gaussian width values of *MRSW* and *MRSL* as well as for all other parameters discussed in Section 2.1. As for the *MRSW* and the *MRSL*, the evolution of mean and Gaussian width values with zenith angle of the *MRSWO* and *MRSLO* parameters show a stable evolution with increasing zenith angle.

From Eq. 1.2[4] and the fact that the energy threshold of the telescope system increases with zenith angle, one would expect a logarithmically increasing reconstructed X_{max} for increasing zenith angles. However, the reconstructed depth of the shower maximum X_{max} decreases with increasing zenith angle contrary to the expected behaviour. Since the simulated X_{max} values show the expected characteristic while the reconstructed, as shown in Fig. 2.4, do not, this is indicative for a systematic feature in the geometrical reconstruction for events of large zenith angles. This effect is not apparent in the case of CTA Monte Carlo γ-ray simulations and the reconstruction of X_{max} as weighted average mean value instead of the geometrical reconstruction using pairs of telescopes as in the H.E.S.S.

[4] From now on, X_{max} denotes the actual thickness transversed by the shower as Eq. 1.2 divided by $\cos(\Theta_z)$.

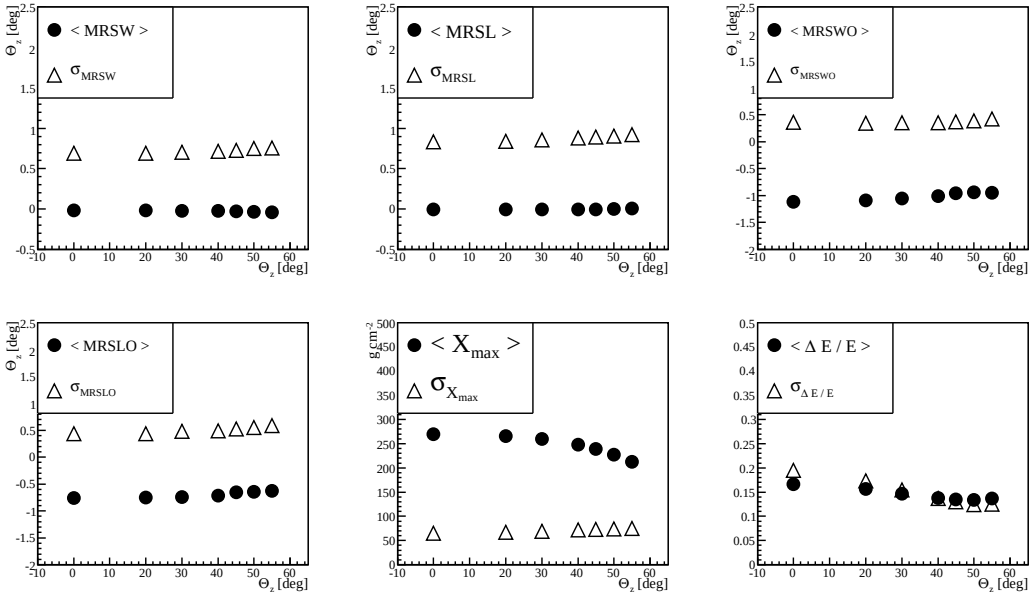

Figure 2.4: Zenith dependence of mean (filled circles) and Gaussian width (open triangles) of variables with γ/hadron separation potential for Monte Carlo γ rays, simulated at an offset of 0.5° and at zenith angles ranging from 0° to 55°.

Standard Analysis (Bernlöhr 2010, priv. comm.). Given the fact that γ rays and hadrons are treated in the same way in the reconstruction, and that X_{max} is just slowly declining with increasing zenith angle, this feature is not of imminent importance for the studies presented in the following and could be addressed in a future project.

The mean and Gaussian width of ΔE/E is decreasing with increasing zenith angle, pointing to the fact, that for larger zenith angles, the energy threshold of the telescope system increases and at the same time the difference in reconstructed energies between telescopes is getting smaller. This behaviour was already visible in Fig. 2.4.

The zenith- and offset angle are not the only parameters which change on an event-by-event basis during observations. Obviously the reconstructed event energy changes as well and should also be well behaved to not introduce artifacts in the analysis, like e.g. steps in γ-ray efficiency over energy in the γ/hadron separation. Fig. 2.5 shows the energy dependence of the mean and Gaussian width values for all parameters discussed in the previous section.

The *MRSW* and *MRSL* parameter distributions show a rather stable characteristic for all reconstructed event energies. In the case of the *MRSW* the mean is centred around zero for energies up to 10 TeV. At larger energies the mean value systematically deviates from 0 to negative *MRSW* values. This behaviour could be suggestive for the effect, that events of lower energy and very high energy populate the same regions of *size* and reconstructed impact distance in the shower shape look-up tables. Since the Monte Carlo γ rays are simulated according to a power-law in energy $dN/dE \sim E^{-\Gamma}$ with index $\Gamma = 2.0$, the total number of low energy events with mis-reconstructed impact distances, even though their fraction is small, is comparable to the total number of properly reconstructed events of

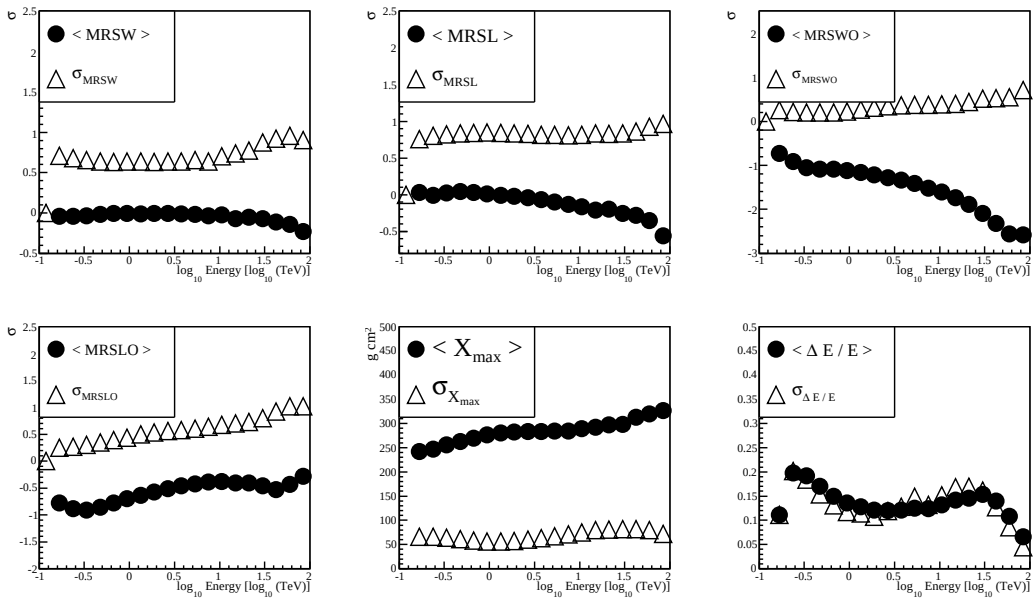

Figure 2.5: Energy dependence of mean (filled circles) and Gaussian width (open triangles) of variables with γ/hadron separation potential for Monte Carlo γ-rays, simulated at an offset of 0.5° and a zenith angle of 20°.

high energy. For this reason the expected width is overestimated and hence the *MRSW* for high energy events underestimated. The same effect is apparent for the *MRSL* parameter. Also here the mean is well centred around 0 for reconstructed event energies of up to $\approx$ 3 TeV and shows a decline for events of larger energy. The Gaussian width of both distributions shows as well a stable behaviour and is just slowly increasing with energy.

The *MRSWO* and *MRSLO* parameters are constructed in a similar fashion as *MRSW* and *MRSL*, respectively, but compare the measured quantities *width* and *length* to the expectation as obtained from background data instead of using Monte Carlo γ-ray simulations. Thereby, the mean values of both *MRSWO* and *MRSLO* naturally change with the reconstructed event energy. The Gaussian width of the two distributions increases with energy in the same manner as for *MRSW* and *MRSL*.

As obvious from Equation 1.2, the depth of the shower maximum X_{max} increases logarithmically with event energy. This is also clear from Fig. 2.5: X_{max} linearly increases with the logarithm of the reconstructed event energy, at the same time the spread stays constant over the whole energy range.

The ΔE/E parameter is defined as the mean difference in reconstructed event energies between all triggered telescopes. Even though the difference in reconstructed telescope energies is normalised to the mean reconstructed energy, the effect of shower fluctuations manifests itself in a change of mean and width with energy for ΔE/E. Low energy showers exhibit larger fluctuations in the recorded image intensities and hence show a larger spread in the reconstructed telescope energies. With increasing energy, these fluctuations get smaller and hence ΔE/E does. Due to the asymmetric shape of the ΔE/E distribution, the spread of the corresponding distribution is also getting smaller with increasing event

energies.

Given the results of the afore-made studies, it gets clear, that parameters with γ/hadron separation potential show a partial zenith- and energy dependence. Hence, an analysis which aims for an improved and stable γ-ray response over the whole dynamical range of the telescope system, namely in energy and zenith angle, has to take these effects in the γ/hadron separation into account. The consideration of those dependencies for six parameters makes the choice of appropriate cuts complicated. Apart from the already reached complexity of the problem, another challenging difficulty in the γ/hadron separation is the consideration of (non-)linear correlations between the parameters. As will be seen later, the desired separation improvements cannot be achieved with a simple box-cuts-based selection as applied in the H.E.S.S. Standard Analysis. More elaborated methods, such as e.g. Likelihood classifiers, Artificial neural networks or decision-tree based classifiers, can help to explore the full available information and to deal with the complexity and (non-) linearity of the selection. In the next section, the Boosted Decision Tree method – an multivariate analysis technique, integrated in the TMVA (Hoecker et al. 2007) package – is introduced and its basic functioning is discussed in detail.

2.2 Classification using Boosted Decision Trees

The software package TMVA (Hoecker et al. 2007) provides a generic scheme in which different multivariate classification methods can be trained, evaluated and tested in parallel. As of version 3.8.4 (the version used in this work) the following algorithms are included in different representations: Rectangular cut optimisation, Projective Likelihood estimator, Multidimensional Likelihood estimator, k-Nearest Neighbour Classifier, H-Matrix discriminant, Fisher discriminant, Function Discriminant Analysis, Artificial Neural Networks (ANN), Support Vector Machine, Boosted Decision Trees and Predictive learning via rule ensembles (see Hoecker et al. 2007) for further details and different classifier training options). Even though the aforementioned methods have a different response to (non)-linear correlations and different robustness in terms of e.g. overtraining or weakly classifying variables, they all share the property of being basically extensions of one-dimensional cut-based analysis techniques to multivariate algorithms. Multivariate analysis (MVA) methods can be divided into two different types: those, which consider non-linear correlations between input parameters in the classification (like e.g. ANN and BDT) and those which do not (like e.g. Likelihood-, Fisher- and Cuts-based methods). Given the considerations made in the previous section, former algorithms are expected to be preferable for the purposes of this work, a hypothesis which is going to be tested in Section 2.6. While boosted decision trees effectively ignore weakly- or non-classifying variables in the separation, neural networks could suffer from those, leading to a degraded performance or unexpected behaviour of the ANN response.

MVA classifiers are commonly utilised in natural sciences and sociology for complex problems, such as e.g. classification of events of different type using a set of input variables. In particular, the BDT algorithm has been successfully utilised for particle identification in high energy physics (Yang et al. 2005; Abazov et al. 2008) and for supernova searches in optical astronomy (Bailey et al. 2007).

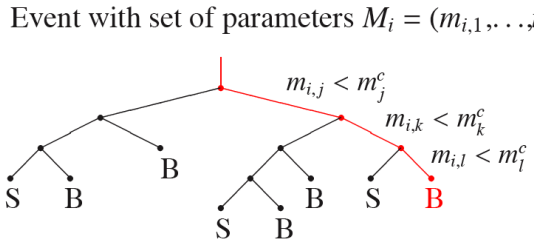

Figure 2.6: Sketch of a decision tree. An event, described by a parameter set, $M_i = (m_{i,1},\ldots,m_{i,6})$, undergoes at each node a binary split criterion (passed or failed) on one of its parameters until it ends up in a *leaf*. This leaf marks it as signal (S) or background (B) (Figure adapted from Ohm 2007; Ohm et al. 2009b).

2.2.1 Basics of the Decision Tree algorithm

A decision tree can be depicted by a two-dimensional structure like the one shown in Fig. 2.6. At each branching, a binary split criterion (passed or failed) on one of the characterising input parameters is applied, thereby classifying events of unknown type as signal- or background-like. The *training* of a decision tree is the process of determining these split criteria with a training set consisting of events of known type. Since single trees suffer from statistical fluctuations, the single tree is extended to a *forest* of decision trees to achieve a stable response and an improved performance. All trees of a BDT differ in the binary split criteria; the final response is calculated as the weighted mean vote of the classification of all single trees. This vote is the output of the BDT and is referred to as ζ variable in this work – it describes the background- or signal-likeliness of an event. The forest of trees is generated from the initial single tree by a process called "boosting".

2.2.2 The training procedure for a single tree

In the following, the training or building of a single tree is described in more detail. During the training process appropriate splitting criteria for each node in a tree are determined using a training sample S of events of known type. This training sample consists of a signal training sample S_1 and a background training sample S_2, which are again comprised of N_1 signal events and N_2 background events, respectively. Each event in the training set is characterised by a set of input parameters M_i and a weighting factor ω_i. A single decision tree is build from such a training sample by performing the following steps:

- ◇ The training samples are normalised to the total number of signal and background events in such a way that all signal events have the same weight $\omega_i(S_1) = 1/N_1$ and all background events have the same weight $\omega_i(S_2) = 1/N_2$.
- ◇ The tree-building procedure starts at the root node (top node in Fig. 2.6), where the variable and split value that provides the best separation of signal and background

events is determined. Correspondingly, S is divided into two subsets of events that either pass or fail this splitting criterion. Each subset is fed into a child node where again the cut parameter which separates signal and background events best is determined.

- ◇ This process is applied recursively until one of two stop criteria is fulfilled. Tree building is stopped if further splitting would not increase the separation, or if a preassigned minimum number of events is reached in the child node. Thereby overtraining due to statistically insignificant leaves is avoided. According to the majority of signal and background events, the last-grown nodes (which are called leaves) are assigned signal- (S) or background (B) type, respectively (see Fig. 2.6).

2.2.3 Boosting

Single decision trees are sensitive to statistical fluctuations in the training sample, hence a boosting procedure is applied which extends a single tree to a forest of trees. Thereby, the stability of the method is increased. In the boosting procedure, events that got misclassified in the building of the $(n-1)^{\text{st}}$ tree are multiplied with a *boost weight*, α_n, thereby getting a higher weight in the training of the n^{th} tree. Hence, the boosting is applied to all trees except for the first one. This method is known as *AdaBoost* or adaptive boost (Freund & Schapire 1997), where α_n is calculated from the fraction of misclassified events in all leaves of the tree $n-1$, err_{n-1}:

$$\alpha_n = \frac{1 - err_{n-1}}{err_{n-1}} \ . \tag{2.2}$$

The mis-classification error $err_{i,n-1}$ in a single node i in tree $n-1$ is calculated using the number of signal events $S_{i,n-1}$ and background events $B_{i,n-1}$ in that node:

$$err_{i,n-1} = 1 - \max\left(p, 1-p\right), p = \frac{S_{i,n-1}}{S_{i,n-1} + B_{i,n-1}} \tag{2.3}$$

After having applied α_n to each misclassified event, the training samples of signal and background events are re-normalised to retain the sum of weights of all events in a decision tree constant.

2.2.4 BDT settings

The BDT method used in this work is provided by the TMVA package (in version 3.8.4). The decision tree settings are mostly default values, and have been optimised and tested by the TMVA developers. They guarantee a fast training process and at the same time a stable response of the classifier and are marked with a * in the following:

- ◇ The total number of trees in the forest was chosen to be 200*, a good compromise between maximum separation performance and at the same time adequate processing power consume. Varying this number in a wide range does not change the presented results significantly.

- ◇ The separation type used for the BDT training is the *Gini Index**. It calculates the inequality between signal and background distributions for each possible split value to find the best cut. Other separation types, which e.g. utilise the mis-classification error, were tested and found to achieve similar results.

- ◇ Splitting was stopped when the number of events in a node fell below $(N_1 + N_2)$ / $(10 \cdot N_{par}^2)$*. Thereby the training statistics and the number of training parameters is taken into account for the determination of insignificant nodes in the tree. Typical values are between 100 and 1000 for the smallest and largest data set, respectively.

- ◇ The step size used to scan the parameter space for the best splitting criterion was increased from 20 steps for the covered parameter space, the default value for the BDT training, to 100 in this work, to adequately cover training parameters with a large range of values.

2.3 Training and Evaluation of the BDT method

After the discussion of the basic BDT-working principle and the tree growing procedure in the last section, this section concerns the training and evaluation of the BDT classifier with H.E.S.S. data by means of the event classifying parameters introduced and discussed in Section 2.1. First of all, the training set used to teach the BDT the difference between signal and background is presented, before the training process itself is discussed. Finally, the classifiers response is tested and the importance of the training parameters for various observational conditions is examined.

2.3.1 Training sample

The parameters which are used to teach the BDT the differences between EASs initiated by VHE γ rays and cosmic rays have been discussed in Section 2.1. These six event classifying variables (*MRSW*, *MRSL*, *MRSWO*, *MRSLO*, X_{max}, $\Delta E/E$) are describing the training set, which consists of Monte Carlo γ-ray simulations, representing signal events, and *Off data* as charged cosmic-ray background. Whereas point-like source γ rays are simulated at a fixed offset of 0.5° away from the camera centre, cosmic rays reach the Earth isotropically and are hence distributed homogeneously over the field of view of the camera. The simulated γ rays follow an energy distribution $dN/dE \sim E^{-\Gamma}$ with index $\Gamma = 2.0$. Not all signal and background events which triggered the telescope system are used for the training procedure. As well as for the H.E.S.S. Standard Analysis, *Preselection* cuts on the minimum image intensity of 80 p.e. and the maximum distance between *COG* and camera centre of 2.25° are applied to the cleaned images to assure a good shower reconstruction and to reduce image truncation effects at the edge of the camera.

2.3.2 Training

The aim of a BDT classification is a stable and improved γ/hadron separation over the whole dynamical range of an IACT system. In particular, this concerns its accessible

E_{reco} [TeV] / Θ [°]	0.1 – 0.3	0.3 – 0.5	0.5 – 1.0	1.0 – 2.0	2.0 – 5.0	5.0 – 100.0
0.0 – 15.0	120k/240k	55k/110k	55k/115k	35k/70k	25k/45k	15k/25k
15.0 – 25.0	95k/190k	60k/120k	65k/125k	40k/85k/	30k/55k	15k/35k
25.0 – 35.0	60k/120k	65k/130k	70k/135k	50k/95k	35k/70k	20k/45k
35.0 – 42.5	-/-	75k/150k	75k/155k	55k/115k	45k/95k	35k/65k
42.5 – 47.5	-/-	55k/105k	95k/195k	75k/145k	60k/125k	50k/100k
47.5 – 52.5	-/-	-/-	140k/275k	100k/200k	95k/185k	80k/165k
52.5 – 60.0	-/-	-/-	50k/100k	70k/140k	70k/135k	70k/140k

Table 2.1: Number of signal- (first value) and background training events (second value) in all trained zenith angle- and energy bands. Events with small energy and large zenith angle cannot be reconstructed since the energy threshold of the H.E.S.S. array increases with zenith angle.

energy range and the zenith angle of the observation. As demonstrated in Section 2.1, all training variables exhibit a more or less pronounced zenith angle and energy dependence. Hence, the classifiers response will change with zenith angle and energy as well. Especially the increasing energy threshold of the telescope system with increasing zenith angle of the observation combined with the rather strong energy dependence of the *MRSWO*, *MRSLO*, X_{max} and $\Delta E/E$ parameters suggests a training of the BDT in bands of energy and zenith angle to achieve the best performance. H.E.S.S. is operating in the energy range between $\approx$100 GeV and $\approx$100 TeV and usually performs observations at zenith angles between 0° and 60°. The dynamical range was divided into seven zenith angle bands which again are subdivided into six energy bands, such that sufficient statistics for the training process was available and at the same time it was guaranteed that the input parameter distributions do not change significantly within the corresponding band. An overview of all chosen zenith angle and energy bands used for training with the corresponding training statistics can be found in Table 2.1. Note the decreasing number of low energy events with increasing zenith angle, which is a direct consequence of the increasing energy threshold of H.E.S.S. for larger zenith angles. Moreover is the number of training events also decreasing with reconstructed event energy as a result of the declining particle number due to the power-law energy spectra of the training sample. The maximum number of training events in bands of low energy is limited by the statistics of the γ-ray simulations, whereas at high energies, the limiting factor is the statistics of charged cosmic rays due to the different energy spectra of γ rays and cosmic rays ($\Gamma_\gamma = 2.0$ vs. $\Gamma_{CR} = 2.7$). The ratio between N_γ and N_{CR} in each band was chosen to be always in the same range of ($\sim 1:2$). Changing this ratio from e.g. 1:10 to 10:1 from band to band would change the BDT response in terms of mean and sigma values of the BDT output distributions considerably and is therefore not recommended. During the training process a mis-classification rate for every single tree according to Eq. 2.3 is evaluated using the training sample. Table 2.2 summarises the mean fraction of mis-classified events over all trees in the forest during the training procedure with all signal events having the same weight ω_1 and all background events having the same weight ω_2[5]. Even though the absolute number of mis-classified events

[5] Within the TMVA framework this information is not available for the independent test sample. However, as long as the BDT output distributions of both samples agree, also the mis-classification rates should

E_{reco} [TeV] / Θ [°]	0.1 – 0.3	0.3 – 0.5	0.5 – 1.0	1.0 – 2.0	2.0 – 5.0	5.0 – 100.0
0.0 – 15.0	0.054	0.037	0.027	0.019	0.012	0.0084
15.0 – 25.0	0.053	0.037	0.03	0.023	0.016	0.01
25.0 – 35.0	0.054	0.04	0.034	0.029	0.024	0.014
35.0 – 42.5	-/-	0.047	0.035	0.032	0.03	0.023
42.5 – 47.5	-/-	0.053	0.037	0.035	0.036	0.026
47.5 – 52.5	-/-	-/-	0.044	0.035	0.038	0.03
52.5 – 60.0	-/-	-/-	0.047	0.037	0.039	0.028

Table 2.2: Mean fraction of mis-classified events over all trees for all zenith- and energy bands used for training as described in Table 2.1.

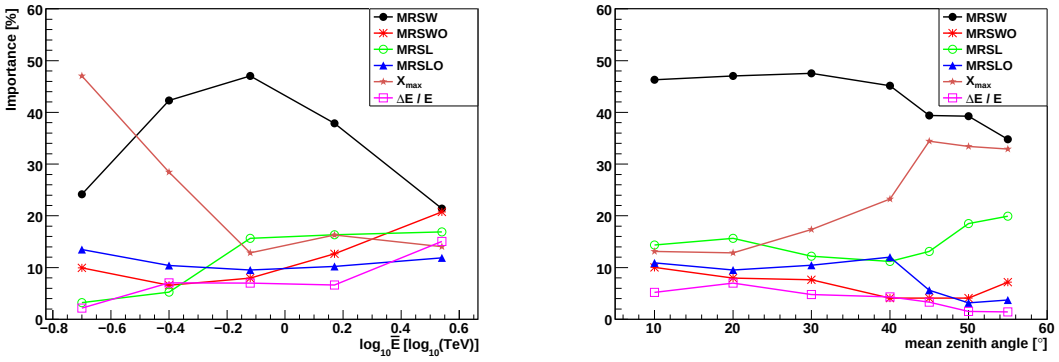

(a) (b)

Figure 2.7: Importance (as defined in the main text) of the training parameters as a function of (a) mean reconstructed energy in the $15° - 25°$ zenith angle band and (b) as a function of mean zenith angle for reconstructed energies between $(0.5 - 1.0)$ TeV (Ohm et al. 2009b).

depends on the performance of the BDT training itself[6], some global properties of the classification performance of the BDT can be deduced. Independent of the zenith angle of the observations a general trend from larger mis-classification rates at low energies (which reaches ≈ 5 % at the lowest energies) to smaller mis-classification rates at high energies (which reaches ≈ 0.8 % at the highest energies) is clearly visible. This illustrates, that even if a training in zenith and energy bands is performed, the separability of γ rays and hadrons changes with energy (for this set of training parameters) and hence the signal-to-background ratio will change as well if a cut on the BDT output at a fixed γ-ray efficiency is applied.

2.3.3 Importance of training variables

As already visible from Fig. 2.3 the input variables show a more or less pronounced γ/hadron separation potential for events of given zenith angle and energy. This characteristic reflects itself in a difference of *importance* of the variables for the building of the BDT. The importance is calculated by counting each occurrence of a classification parameter for splitting during the growing of the forest, weighted by the squared separation-gain and the number of events in each corresponding child node (Breiman et al. 1984). Given the zenith and energy dependence of the training parameters, it is also likely that a certain variable is important for the classification at low energies but adds little classification potential at higher energies. Fig. 2.7 illustrates that the relative importance of the input parameters change with energy and zenith angle from band to band.

From Fig. 2.7(a) it gets clear, that for medium energies between ≈ 300 GeV and ≈ 3 TeV the *MRSW* variable is the most import classification parameter. Even though all other parameters on their own add just little information for the classification, all together have the same importance for the classification as the *MRSW*.

Below a few hundred GeV γ-initiated and hadron-initiated EAS look similar (cf. Fig. 2.2(a) and Sobczynska (2007); Maier & Knapp (2007)), what makes their discrimination challenging using just the shape of the Čerenkov-light images in the camera. Since X_{max} carries information about the primary particle interaction length and is just marginally correlated with the shower shape parameters it adds crucial information about the origin of the primary particle in this low energy regime.

For events with reconstructed energies ≥ 3 TeV the ΔE/E parameter becomes increasingly important for the classification. Whereas γ-initiated showers show a regular structure, hadron-initiated particle cascades exhibit large fluctuations during the shower development and hence have a larger spread in reconstructed energy between triggered telescopes.

Although the *MRSWO* and *MRSLO* variables suffer from larger fluctuations of hadronic showers which were used to fill the corresponding look-up tables, they contribute significantly to the γ/hadron separation, especially for events of higher energy. Fig. 2.7(b) illustrates the development of importance of the training variables for events with energies of $(0.5-1.0)$ TeV as a function of zenith angle. The increasing energy threshold of the telescope system becomes manifest in the increasing importance of X_{max} and the decreasing importance of ΔE/E with zenith angle.

Beyond the variables used in this work, additional parameters which parametrise the intrinsic image properties (e.g. like those obtained for the 3D Model analysis (Lemoine-Goumard et al. 2006)) are sensitive to different shower properties and could further improve the BDT classification. Another method, developed by de Naurois & Rolland (2009) was successfully utilised just recently and uses a similar approach as described in Lemoine-Goumard et al. (2006). de Naurois & Rolland (2009) compare the uncleaned shower images in the camera with the prediction from simulations, which also take into account the night sky background level of the observation. Thereby, the information stored in the tails of the

be the same.

[6] A perfectly trained forest would contain no mis-classified events in the training sample but on the other hand is highly overtrained.

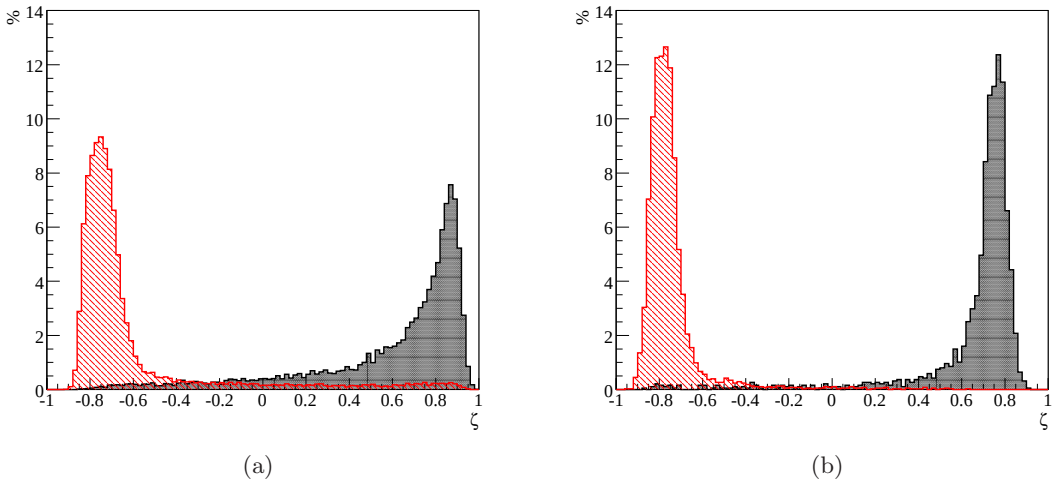

Figure 2.8: BDT output for an independent test sample for events in the 20° zenith angle band (a) with energies of $(0.1-0.3)$ TeV and (b) for energies $(5.0-100.0)$ TeV.

EAS image is not lost in the image cleaning procedure. Parameters which contain this information could be also used for the BDT training, however, their inclusion in the BDT used here is beyond the scope of this work.

2.3.4 BDT response

After the forest of trees has been grown, the BDT classifier's response was tested for all zenith angle and energy bands with an independent test sample, consisting of signal and background events with 10% of the size of the corresponding training sample. Fig. 2.8 illustrates the response of the classifier in the 20° zenith angle band for events of small energy $(0.1-0.3)$ TeV, Fig. 2.8(a)) and very high energy $(5.0-100.0)$ TeV, Fig. 2.8(b)) by means of the result of the BDT classification of the independent test sample. Several characteristic features are apparent in the shape of the distributions. First of all, an in general excellent classification power for low-energy events as well as for high-energy events is obvious. However, as outlined in the last section, the fraction of misclassified events changes with event energy. Whereas in the low-energy band a significant amount of signal (background) events is located in the background (signal) regime of the BDT output, this effect is much smaller at high energies. Moreover does the shape of the distributions change with energy band. While the signal and background distributions at low energies show a broad behaviour, the BDT output distributions at high energies are shifted in terms of their mean values and become at the same time narrower. This effect is related to the distinguishability of- and the ratio between signal and background events[7]. Furthermore, the more events are available to teach the BDT the difference between γ rays and hadronic CRs the better is the achievable classification power[8]. Additionally does the ratio between

[7] The better the overall separation, the smaller the contamination with background events in the signal regime of the BDT output and vice versa.

[8] Up to a limit, where increased training statistics does not further increase the separation. Different training sample sizes have been tested. Reducing the training statistics by e.g. 50% in the lowest-energy

signal and background events determines which class' properties are predominantly learnt by the BDT. The fact that the signal and background ζ distributions look different for events of varying zenith angle and energy, requires zenith angle- and energy-dependent cuts on ζ in the analysis, to make the γ/hadron separation independent of these quantities (see Section 2.5).

2.4 Systematic studies using H.E.S.S. data

The consistent description of VHE γ-ray data by Monte Carlo simulations is one of the key aspects for the analysis of γ-ray sources. VHE γ-ray observations usually cover a broad range in energy and are performed under varying observational conditions such as the zenith angle of the observation, the telescope configuration or the offset between the observation position (the telescope pointing position) and the expected VHE γ-ray source position. To confirm the robustness of the BDT classification with respect to different observational properties, a comparison between Monte Carlo simulations and the VHE γ-ray excess obtained in H.E.S.S. observations of the Galactic Centre (GC) region is investigated.

2.4.1 Background estimation with H.E.S.S.

In order to evaluate ζ for a primary particle which initiated an EAS, its shower properties are reconstructed stereoscopically, considering all telescopes, which pass the *Preselection* (cf. Section 1.3.5). The event with all its characterising input parameters gets fed into the BDT of the corresponding zenith angle range and energy, and gets classified by the trees in the forest. Prior to the comparison between the ζ distributions of simulations and γ-ray-like events from a VHE γ-ray source, one has to estimate the background level which is apparent in the data sample. Therefore, the *Reflected* and *Ring* background methods, which are used in this section and later in the analysis[9], are shortly summarised in the following:

- ◇ VHE γ-ray observations with H.E.S.S. are generally performed in the so-called *Wobble mode*, where at the same time events from the expected source region and from background control regions are recorded. This principle is schematically illustrated in Fig. 2.9, for the *Reflected* and *Ring* background model.
- ◇ A circle around the expected source position defines the *On-Region*. From this region, a VHE γ-ray excess is expected. Here, the radius of the On-Region depends on the expected extension of the VHE γ-ray source.
- ◇ Depending on the model, background control regions are defined: In case of the *Reflected* background model, *Off-Regions* are defined as circles with same radius

band at 0° zenith angle reduces the background rejection efficiency at 90% γ-ray efficiency from 98% to 96%, independent of the ratio between γ rays and hadrons. The effect of a training with even more events was not possible due to the limited available statistics but could be addressed in a future work.

[9] For a detailed discussion of background estimation methods widely used in ground-based VHE γ-ray astronomy see Berge et al. (2007)

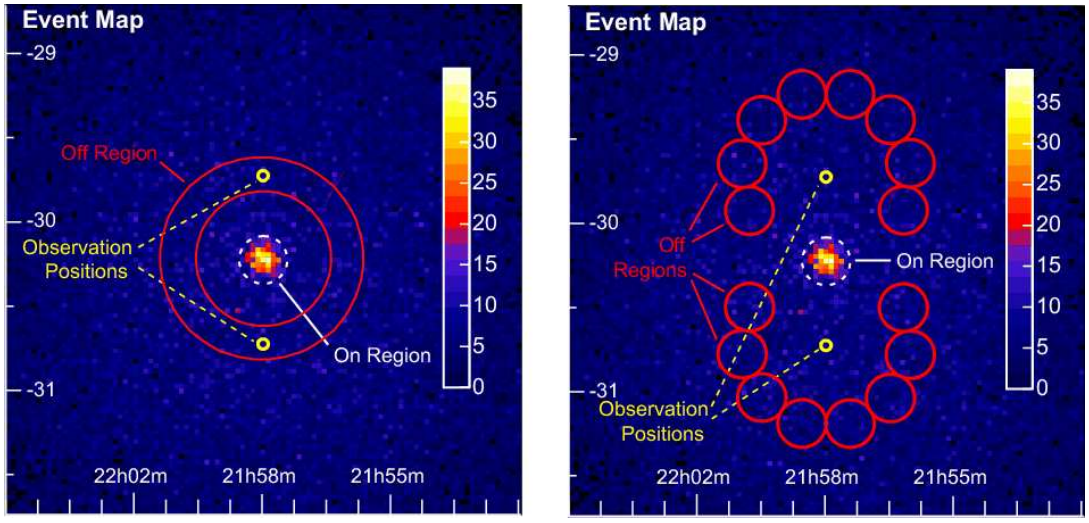

Figure 2.9: VHE γ-ray count map from five hours of H.E.S.S. observations of the active galactic nuclei PKS 2155-304 (Aharonian et al. 2005b). The Ring- (left) and Reflected- (right) background methods are illustrated schematically (Figure taken from Berge et al. (2007)). Yellow circles denote the observation positions at a given wobble offset from the expected source region *(On-Region)*. Red circles in the case of the Reflected method and a ring in the case of the Ring background method denote the *Off-Regions*, used for background estimation.

as the On-Region. The On- and Off-Regions are placed at equal distance to the telescope pointing position. This distance is also referred to as *Wobble offset*. For the Ring background model a ring of given radius and width (concentric around the On-Region) is defined. To reduce the effect of statistical fluctuations in the background sample, it is advisable to choose a large area as Off-Region.

◇ The VHE γ-ray excess from the expected source region is then calculated as

$$N_\gamma = N_{On} - \alpha \cdot N_{Off} \ , \tag{2.4}$$

with N_{On} and N_{Off} being the number of events from the On-Region and Off-Regions, respectively. α is a normalisation factor which accounts for different geometrical areas and acceptance of the On- and Off-Regions.

2.4.2 Comparison between simulations and data

The data set used in the following is based on observations of the GC from 2004, 2005 and 2006 (Aharonian et al. 2009a). The data accumulates to a total live time[10] of 47.4 hours (compared to 93 hours in the published work) and was selected by zenith angle to cover a smaller range of $0° \leq \Theta_z \leq 15°$[11]. Thereby, mixing of γ-ray simulations was

[10] Live time is defined as the observation time, corrected for the dead-time of the telescope system.

[11] The data set used in Ohm et al. (2009b) comprises just a subset of the data used for the earlier H.E.S.S. publication from 2006 (Aharonian et al. 2006b) which adds up to a total live time of 11.4 hours. For the sake of completeness can the comparison between simulations and data for this data set be found in Appendix A.

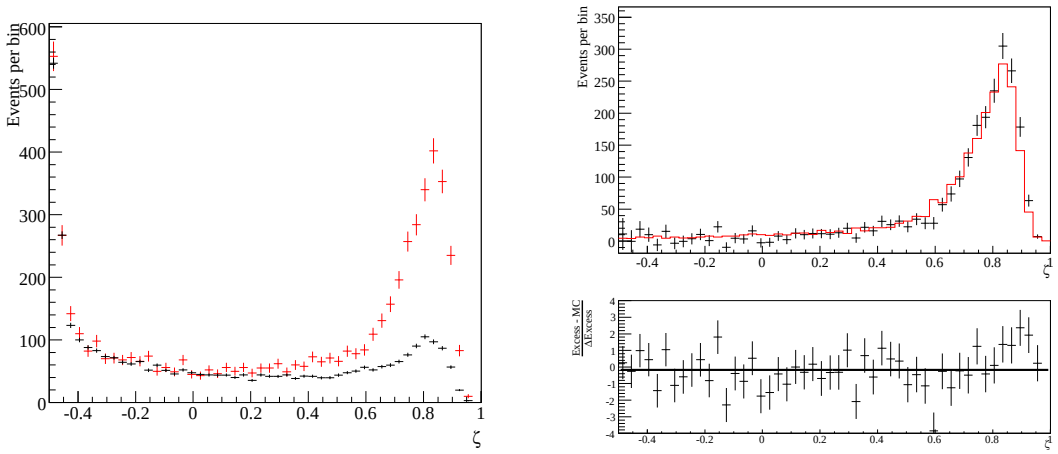

(a) (b)

Figure 2.10: (a): ζ distribution for events from the On-Region (red) and events from the Off-Regions (black), weighted by α, from HESS J1745–290 observations. (b) Comparison between Monte Carlo γ-ray simulations (red curve) and VHE γ-ray excess, normalised to the number of events in the range ($0 \leq \zeta \leq 1$). Also shown are the residua between the two distributions and the result of a fit of a constant, which is compatible with 0 residuum within the statistical errors and has a χ^2/ndf of 58/48.

avoided when comparing results at different zenith angles. Since the HESS J1745–290 data set is comprised of GC region- and nearby target observations, the mean offset of the observations is with 0.8° slightly larger as the nominal wobble offset of 0.5° – 0.7° as in observations of other point-like sources. In the following the VHE γ-ray excess from the GC source HESS J1745–290 is compared to the prediction as obtained from Monte Carlo γ-ray simulations at a fixed zenith- and offset angle of 0° and 1°, respectively. The energy spectrum of HESS J1745–290 is equally well described by a broken power law (with spectral indices $\Gamma_1 = 2.0$, $\Gamma_2 = 2.6$ and a break energy of 2.6 TeV) and an exponential cut-off power law (with spectral index $\Gamma = 2.1$ and a cut-off energy $E_c = 15.8$ TeV) (Aharonian et al. 2009a). For an appropriate description of the data, the Monte Carlo γ rays are simulated according to an exponential cut-off power law with same E_c and Γ as found by Aharonian et al. (2009a).

The ζ distributions of events originating from the On-Region and from the background control regions (Off-Regions), scaled by α, are shown in Fig. 2.10(a). The VHE γ-ray excess is calculated using the number of events coming from the On-Region N_{On}, the normalisation factor α and the number of events coming from the Off-Regions N_{Off} as $N_\gamma = N_{On} - \alpha \cdot N_{Off}$. Fig. 2.10(b) reveals an excellent agreement between γ-ray simulations and VHE γ-ray excess, confirming the robust classification of the BDT for simulations and real data in a broader energy range. The comparison between VHE γ-ray excess events with zenith angles $15° \leq \Theta_z \leq 25°$ and Monte Carlo γ-ray simulations at 20° zenith angle also revealed an excellent agreement in terms of a fit of constant to the residua distribution, demonstrating the robustness of the BDT classification in two different zenith angle bands.

As aforementioned, the BDT method is able to classify events of different *multiplicity*.

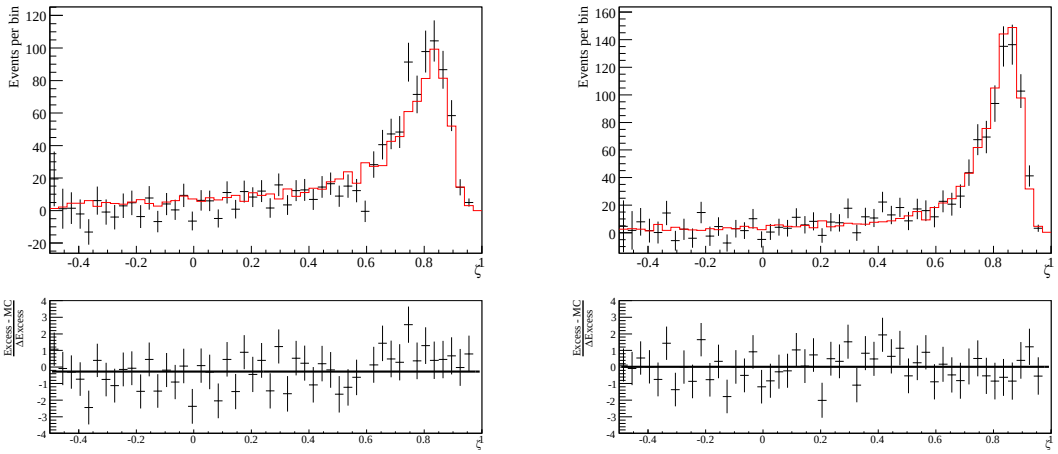

Figure 2.11: Comparison of ζ distributions for Monte Carlo γ-ray simulations and VHE γ-ray excess (a) for events with a multiplicity of 2 and (b): for events with reconstructed energies 0.2 TeV $\leq$ E $\leq$ 0.4 TeV. The lower panel again shows their residua and the result of a fit of a constant. Both fits are compatible with 0 residuum within the 2σ statistical errors and have a χ^2/ndf of 60/48 and 36/49, respectively.

Especially events whose EAS is reconstructed using just two telescopes are difficult to classify, given the limited separation information stored in the input parameters. Nevertheless, these kind of VHE γ-ray excess events are considerably well described by the simulations and show just a slight shift towards negative values ($p_0 = -0.28 \pm 0.15$) in the residual distribution (Fig. 2.11(a)). Due to the larger fluctuations in showers of low energy are events of smaller energy difficult to classify as well. Fig. 2.11(b) demonstrates, that also for events with energies 0.2 TeV $\leq$ E $\leq$ 0.4 TeV, the BDT classification works in the same way for γ-ray excess and γ-ray simulations. The fit of a constant to the residua distribution is compatible with 0 residuum within statistical errors and has a excellent χ^2/ndf of 36/48.

As discussed in Sec. 1.3.2, the optical reflectivity of the H.E.S.S. mirrors changes on time scales of months and years due to seasonal effects and mirror degradation. Hence, the response of the telescope system is changing and leads to a varying trigger threshold with time. Therefore, the stability of the BDT classification for data sets, accumulated in observations which span several years, is crucial. Fig. 2.12 shows the residua distribution for the complete HESS J1745–290 data set from 2004 to 2006 and split by year for events of all *multiplicity* and with reconstructed energies 0.2 TeV $\leq$ E $\leq$ 10.0 TeV. All distributions show 0 residuum (within 2σ statistical errors) and a satisfactory χ^2/ndf $\leq$ 1.5.

The considerations made before have demonstrated that the VHE γ-ray excess measured from HESS J1745–290 is well classified by the BDT and is consistently described by γ-ray simulations with the same properties as the data. Especially the stability of the classification with respect to different observation times and different observational conditions such as e.g. the zenith angle or energy of the event has been shown and motivates the use of the BDT approach for the analysis of VHE γ-ray sources.

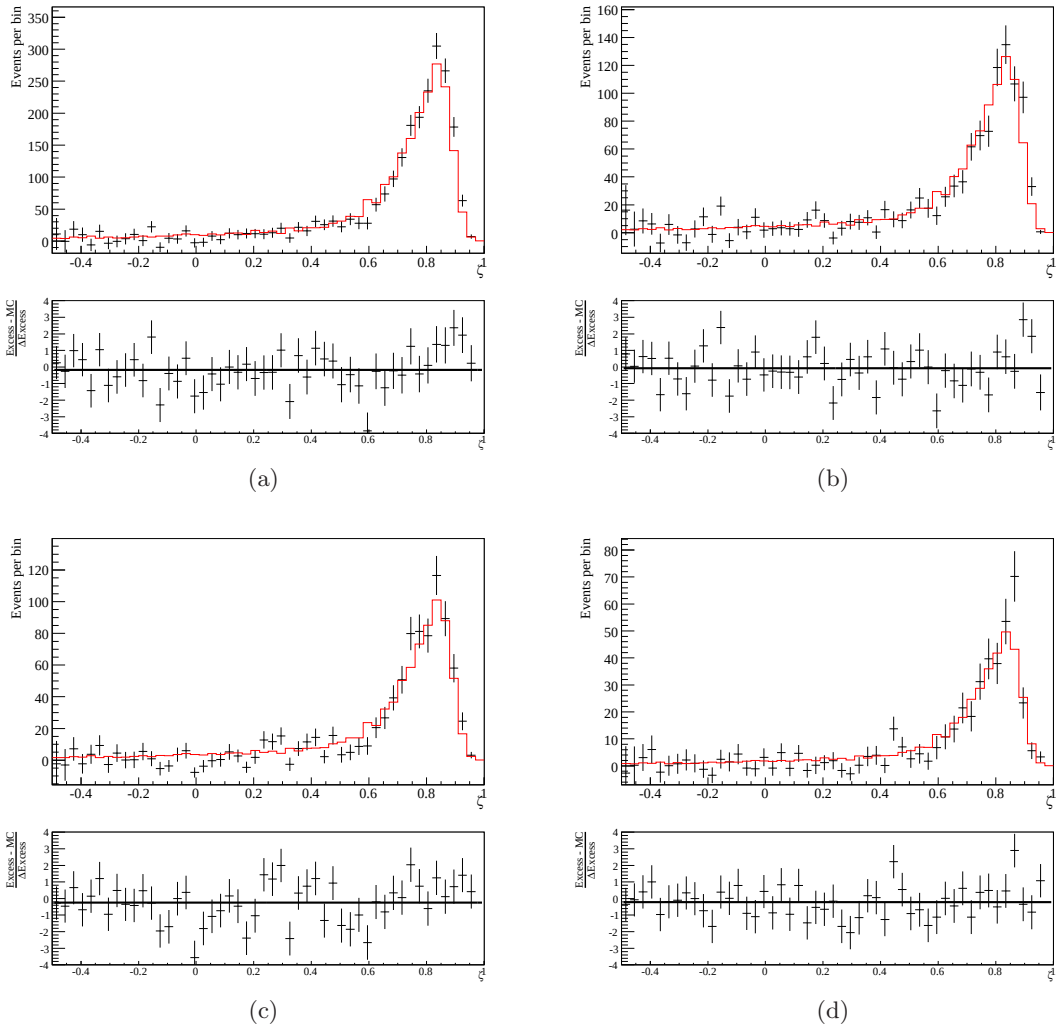

Figure 2.12: Comparison of ζ distributions for Monte Carlo γ-ray simulations and VHE γ-ray excess for the complete data set (a) and for the 2004 (b), 2005 (c) and 2006 (d) data. All fits are compatible with 0 residuum within 2σ statistical error and have a χ^2/ndf of 58/48, 60/48, 72/48 and 45/48, respectively $(\mathrm{a}-\mathrm{d})$.

2.5 Performance of a BDT classification

The last section demonstrated the applicability of the BDT approach in terms of classification of γ-ray-like events under varying observational conditions such as the observation time, the covered energy range or the zenith angle of the observation. As illustrated in Section 2.1 and in Figures 2.4 and 2.5, the more or less pronounced energy- and zenith-dependence of the input parameters leads to a zenith- and energy-dependent classification of the BDT (see Fig. 2.8 for an example). Hence, a fixed cut on ζ would accordingly lead to different γ-ray selection efficiencies, depending on the observational conditions. This problem is circumvented by assigning a γ-ray efficiency for every possible ζ cut in each trained zenith- and energy band using the independent test sample. Thereby, for a given γ-ray efficiency $\epsilon_\gamma(\zeta)$ one unique ζ value exists, which represents the ζ cut value associated

Configuration	$\epsilon_\gamma(\zeta)$ Max	θ^2_{cut} Max (degrees^2)	Size Min (p.e.)
Standard	0.84	0.0125	60
Hard	0.83	0.01	160
Weak	0.80	0.01	80

Table 2.3: Selection cuts optimised for Configuration Standard (strong, steep spectrum sources), Hard (weak, hard spectrum sources) and Weak (very weak, steep spectrum sources) for the ζ analysis. $\epsilon_\gamma(\zeta)$ corresponds to the γ-ray efficiency after application of the *Preselection*.

E_{reco} [TeV] / Θ [°]	0.1 – 0.3	0.3 – 0.5	0.5 – 1.0	1.0 – 2.0	2.0 – 5.0	5.0 – 100.0
0.0 – 15.0	0.28/0.31	0.59/0.61	0.63/0.64	0.52/0.59	0.61/0.62	0.63/0.64
15.0 – 25.0	0.27/0.29	0.56/0.58	0.61/0.63	0.56/0.57	0.56/0.57	0.60/0.61
25.0 – 35.0	0.22/0.25	0.51/0.53	0.59/0.60	0.55/0.57	0.48/0.51	0.54/0.56
35.0 – 42.5	-/-	0.45/0.48	0.58/0.60	0.52/0.53	0.44/0.46	0.43/0.45
42.5 – 47.5	-/-	0.25/0.28	0.54/0.56	0.54/0.56	0.42/0.45	0.39/0.42
47.5 – 52.5	-/-	-/-	0.47/0.50	0.48/0.51	0.36/0.39	0.38/0.41
52.5 – 60.0	-/-	-/-	0.29/0.32	0.46/0.48	0.38/0.40	0.35/0.37

Table 2.4: ζ cuts in all zenith angle and energy bands which correspond to an $\epsilon_\gamma(\zeta)$ cut of 0.84 (ζ std-cuts, first value) and 0.83 (ζ hard-cuts, second value).

to this $\epsilon_\gamma(\zeta)$. According to the procedure described in Sec. 1.3.5, γ-ray selection cuts are optimised simultaneously on *size*, θ^2 and $\epsilon_\gamma(\zeta)$ (compared to *size*, θ^2, *MRSW* and *MRSL* in the H.E.S.S. Standard Analysis) to achieve the maximum possible significance per observation time for two combinations of source strength and source spectra (strong, steep spectrum sources and weak, hard spectrum sources). Additionally, to address the problem of more and more very weak VHE γ-ray sources with H.E.S.S., a set of *Weak* cuts, optimised for 0.5% of the integrated Crab flux above 200 GeV and spectral index $\Gamma = 2.6$, has been developed for the BDT analysis. These three sets of cuts are presented in Table 2.3. The ζ cut values which correspond to the $\epsilon_\gamma(\zeta)$ cuts of configuration Standard and Hard are summarised in Table 2.4[12].

Depending on the γ-ray selection cuts used in the analysis, basic parameters, like e.g. the energy threshold, the point-spread-function (PSF) or the effective γ-ray detection area A_{eff} change. In the following a comparison between the H.E.S.S. Standard Analysis and the developed ζ cuts regarding basic performance parameters of the telescope system is employed.

[12] For comparability and lucidity, the systematic tests presented in the following are done for configuration Standard and Hard. Nevertheless, they have also been performed for Configuration Weak and found to give consistent results.

2.5.1 Energy reconstruction

The energy of a VHE γ ray impinging Earths atmosphere and initiating an EAS is reconstructed following the procedure described in Sec. 1.3.3, using look-up tables, which return the expected energy of the event under a γ-ray hypothesis taking into account the intensity measured in the telescopes, the reconstructed distance of the shower impact point on ground to the corresponding telescope and the zenith- and offset angle of the event. The error on the reconstructed energy of an event ΔE is defined as the relative difference between true Monte Carlo Energy E_{true} and reconstructed energy E_{reco} of the event: $\Delta E = (E_{reco} - E_{true})/E_{true}$. Fig. 2.13(a) depicts the distribution of the relative bias ΔE as a function of simulated energy for the two sets of cuts and the ζ analysis and the H.E.S.S. Standard Analysis exemplarily for γ-ray simulations at 20° zenith- and 0.5° offset angle with a simulated spectral index $\Gamma = 2.0$. All distributions behave like as described in Aharonian et al. (2006a), with a positive bias at low energies as a consequence of a selection effect and a negative bias at very high energies due to a degeneracy in the reconstruction of far away, high-energy showers. In the spectral analysis (see later this section), an adequate energy range, avoiding too large energy bias values, has to be defined (Aharonian et al. 2006a). This *safe threshold* value is defined as the upper edge of the first bin in the energy bias distribution for which $\Delta E < 0.1$, plus 10% of this energy. The *safe threshold* values are exemplarily indicated as vertical lines in Fig. 2.13(a) for a fixed zenith- and offset angle of 20° and 0.5°, respectively, and for zenith angles $0° \leq \Theta_z \leq 60°$ and an offset of 0.5° in Fig. 2.13(b). Apart from a general agreement in the shape of the ΔE distributions, it is noticeable to mention the slightly (about 5% – 7%) smaller energy thresholds of the ζ cuts compared to the cuts applied in the H.E.S.S. Standard Analysis for zenith angles of $\leq 45°$. This feature is a direct consequence of the lower *size* cuts applied in case of the ζ analysis.

The ΔE distribution for Monte Carlo γ-ray simulations at 20° zenith- and 0.5° offset angle is shown in Fig. 2.14(a) for the cuts applied in configuration Standard and Hard of the H.E.S.S. Standard Analysis and the ζ analysis, respectively. Both show similar characteristics. The energy resolution is defined as the width of a Gaussian fit to the ΔE distribution and reaches, averaged over all simulated energies, 15% in case of configuration Standard and 13% in case of configuration Hard. This is remarkable, given the lower energy threshold of the ζ cuts and the at the same time difficult energy reconstruction at low energies. Fig. 2.14(b) further reveals, that the energy resolution of the ζ cuts is even better than the cuts applied in the Standard Analysis for certain energy ranges.

2.5.2 Angular resolution

The angular resolution of H.E.S.S. is defined as the radius which contains 68% of all reconstructed events, which were simulated at a certain position on the sky at a given zenith- and offset angle. The whole function which describes the angular distribution of events is referred to as point-spread-function (PSF) of the instrument and is important in terms of point-source sensitivity (the smaller the PSF, the smaller the amount of underlying diffuse hadronic background in the analysis) and for morphological studies. It is particularly important for the analysis of extended sources such as Westerlund 1 (see Chapter 5), that the PSF is well behaved also at larger offsets. In Fig. 2.15 the PSF as resulting from the

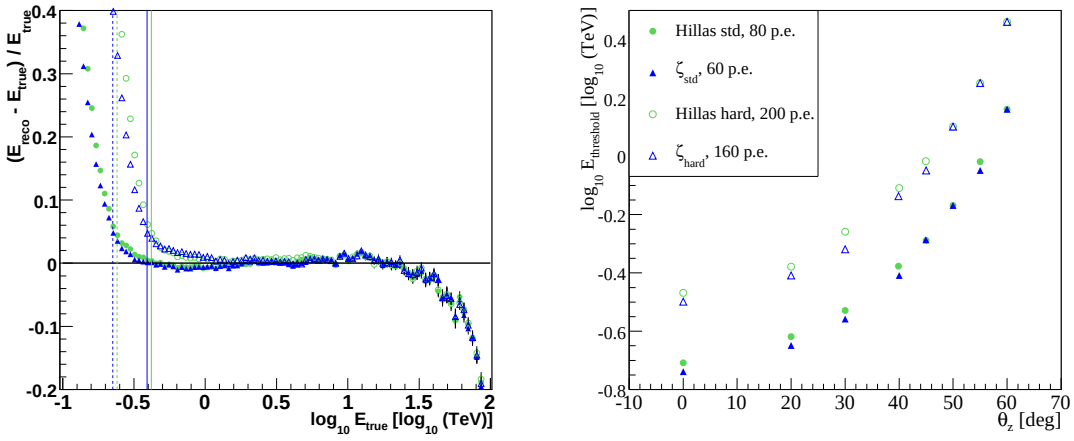

(a) (b)

Figure 2.13: (a) Comparison of ΔE as a function of true energy for Monte Carlo γ-ray simulations at 20° zenith- and 0.5° offset angle for the cuts applied in the H.E.S.S. Standard Analysis and in the ζ analysis. Vertical lines indicate the *safe threshold* as applied in the spectral analysis for the four sets of cuts. Straight lines correspond to Configuration Hard, dotted lines to configuration Standard, blue stands for cuts applied in the ζ analysis, green for cuts applied in the Standard Analysis. (b) *Safe threshold* as a function of simulated zenith angle for the four sets of cuts.

cuts applied to Monte Carlo γ-ray simulations with spectral index $\Gamma = 2.0$ in the ζ- and H.E.S.S. Standard Analysis is shown for all zenith- and offset angle combinations. Characteristic for all offset angles is a stable PSF for zenith angles $\leq$50°. At larger inclinations, the PSF gets considerably worse due to the increasing number of mis-reconstructed events. For offsets $\leq 1.5°$, the Standard Analysis and the ζ analysis perform equally well. At larger offset angles, however, the BDT approach clearly outperforms the Standard Analysis and proves to be particularly suitable for the analysis of VHE γ-ray sources which exceed 2° in size for all zenith angles. This is indicative for a selection effect, as resulting from the rejection of more mis-reconstructed events at large offset angles for the ζ analysis (see Fig. 2.16(a)). The relative acceptance for γ-ray like events for offsets $\geq$1.5° is significantly lower for the ζ analysis compared to the Standard Analysis, both for the Hard- as well as for the Standard cuts configuration, supporting the interpretation of the improved PSF for the ζ analysis as a selection effect. Fig. 2.16(b) depicts the evolution of the PSF as a function of simulated Monte Carlo energy for the ζ- and Standard Analysis. For configuration Standard and the ζ analysis an improvement in angular resolution of $\mathcal{O}$(10%–15%) for medium energies 0.5 TeV $\leq$ E $\leq$ 30.0 TeV is achieved. On the other hand, the PSF for configuration Hard and the ζ analysis is improving for energies $\geq$ a few TeV compared to the Standard Analysis.

The expected performance in terms of angular resolution from simulations can be compared to the angular distribution as obtained from observations of VHE γ-ray sources. Fig. 2.17 conducts this comparison with data obtained in observations of the AGN PKS 2155–304 during a high state in summer 2006, and observations of the Crab nebula, the standard

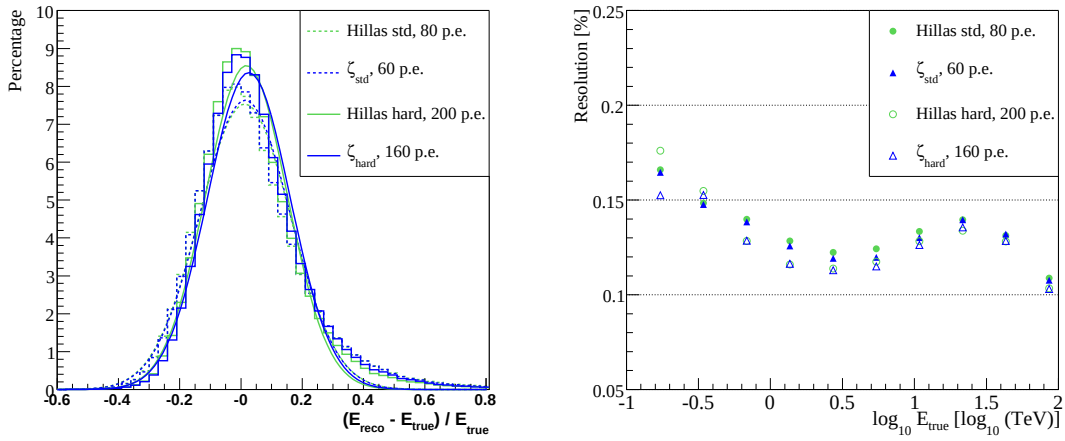

(a) (b)

Figure 2.14: (a) Comparison of the relative error in the reconstructed event energy for the cuts applied in the ζ analysis and the H.E.S.S. Standard Analysis for the same set of Monte Carlo γ-ray simulations as described in Fig. 2.13. The width of a Gaussian fit is 15% in case of Standard cuts and 13% in case of Hard cuts. (b) Energy resolution, defined as the width of a Gaussian fit, as a function of simulated energy for the four sets of cuts. The Hard cuts suffer from events with poorly reconstructed directions in the lowest-energy bin, which reduces the energy resolution.

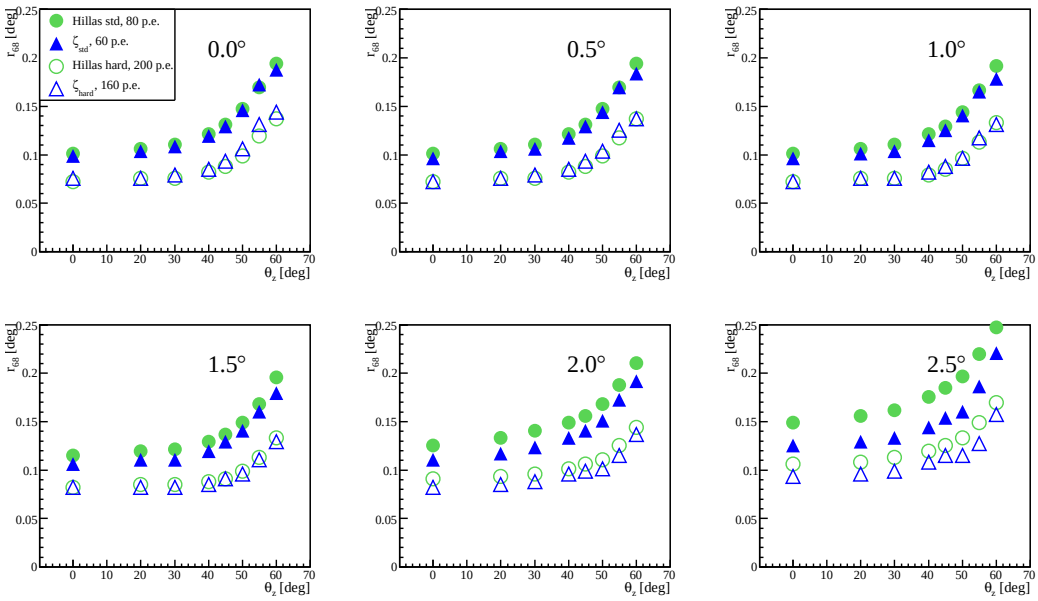

Figure 2.15: Angular resolution, defined as the 68% containment radius r_{68} as a function of zenith angle for all simulated offset angles from 0° to 2.5° in steps of 0.5° (from top left to bottom right).

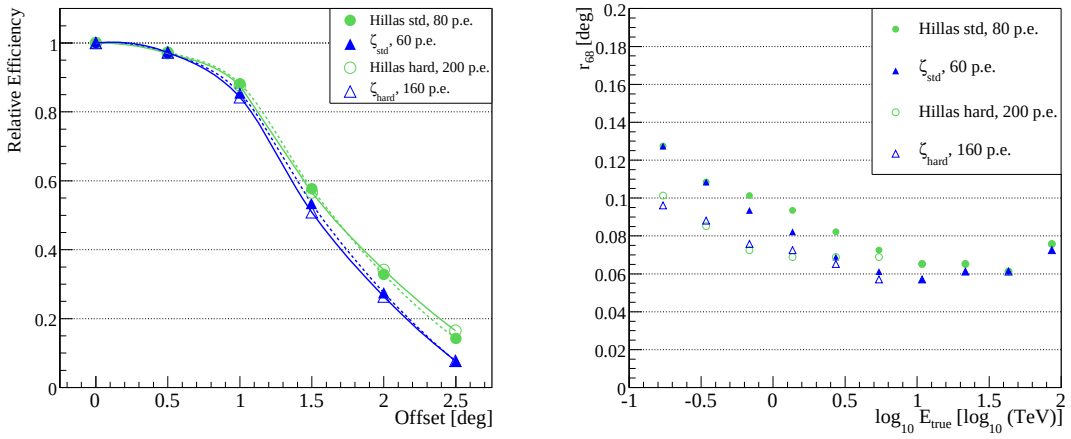

(a) (b)

Figure 2.16: (a) γ-ray acceptance, defined as the fraction of events passing cuts over all simulated events for Monte Carlo γ rays at 20° zenith angle, relative to 0° offset. (b) Angular resolution r_{68} as a function of simulated energy for Monte Carlo γ rays at 0.5° offset angle and 20° zenith angle.

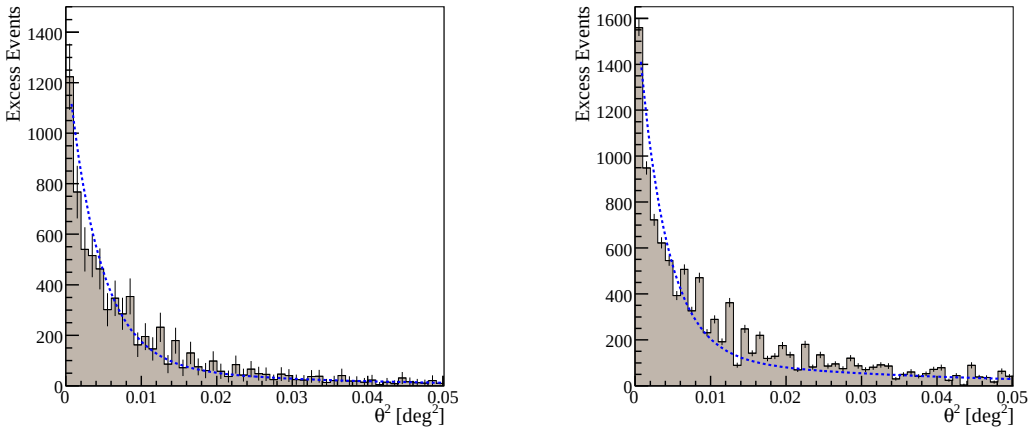

(a) (b)

Figure 2.17: Squared angular distribution θ^2 of γ-ray excess events coming from the direction of (a) the AGN PKS 2155–304 and (b) the Crab nebula after application of ζ_{std} cuts with a minimum image *size* of 60 p.e.. The blue dotted line indicates the θ^2 distribution as expected from Monte Carlo γ-ray simulations with same properties as the recorded data, scaled to match the first bin.

candle in VHE γ-ray astronomy, over a five-year period. Both data samples reveal an excellent agreement between the angular distribution of γ-ray excess and Monte Carlo prediction, confirming the applicability of the BDT classifier for morphological studies.

2.5.3 Effective detection area

The differential flux of a γ-ray source is estimated using the number of collected γ rays which pass the applied selection cuts N_γ, the corresponding effective γ-ray collection area A_{eff} for the given data set and the live time of the observation t. The differential flux is calculated from the number of γ-ray excess events according to Eq. 2.4, per reconstructed energy E and time t, weighted by A_{eff}:

$$F(E) = \frac{1}{A_{\text{eff}}(E, \Theta_z, \psi, \nu_{az})} \frac{d^2 N_\gamma}{dE dt} \ . \tag{2.5}$$

A_{eff}, the area to which the instrument is sensitive for the detection of incoming particles, is a function of the event energy E and furthermore depends on the azimuth angle ν_{az}, the zenith angle Θ_z and offset angle ψ of the event as well as the optical response of the telescopes and is modelled from Monte Carlo simulations. The effective detection area is calculated as the fraction of simulated events that pass a certain set of selection cuts N_{pass} over all simulated events N_{MC}, multiplied by the simulated area A_{MC}. Fig. 2.18(a) depicts the energy distribution of Monte Carlo γ rays which pass the four sets of cuts as applied in the Standard Analysis and the ζ analysis compared to the total number of simulated events as a function of energy. The steep decline of events with low energies, passing selection cuts is due to the trigger criterion. Again, the lower *size* cuts in the ζ analysis translates into lower energy thresholds and an increased number of events passing the selection at these energies. The resulting effective detection area A_{eff} is shown in Fig. 2.18(b) and can be further investigated by comparing the relative difference between A_{eff} as obtained for ζ cuts and Standard Analysis cuts. Fig. 2.18(c) illustrates that the relative difference in A_{eff}, $\Delta A_{\text{eff}} = (A_{\text{eff,std}} - A_{\text{eff},\zeta})/A_{\text{eff,std}}$ is never larger than 20% for all energies above the *safe threshold*. It is also obvious, that for small energies E $\leq$ 0.2 (0.7) TeV in configuration Standard (Hard) and for energies E $\geq$ 10 TeV the A_{eff} for the ζ cuts is in general larger compared to the A_{eff} as achieved with the Standard Analysis.

Since the studies presented before just concern Monte Carlo simulations, the applicability of the BDT approach for the spectral analysis of real VHE γ-ray sources is performed in the following. Differential energy spectra as obtained for the ζ analysis are compared to published results for three sources of different extension (point like vs. extended), spectral index (hard vs. steep spectra) and γ-ray flux (weak vs. strong) and for observations lasting for years and performed at different zenith angles and with different telescope pointing strategies. Fig. 2.19(a) illustrates the offset distributions of events originating from HESS J1745–290, the Crab nebula and HESS J1023–575, unveiling different source extensions and pointing strategies. Fig. 2.19(b) elucidates the difference in covered zenith angle during the observations.

HESS J1745–290

The data set used to derive the differential energy spectrum of HESS J1745–290 was presented in Sec. 2.4.2 and accumulates to a total live time of 109 hours[13]. Compared to

[13] The 10% difference in total live time between the data set used in the following and the one used in Aharonian et al. (2009a) is due to different run quality selection criteria.

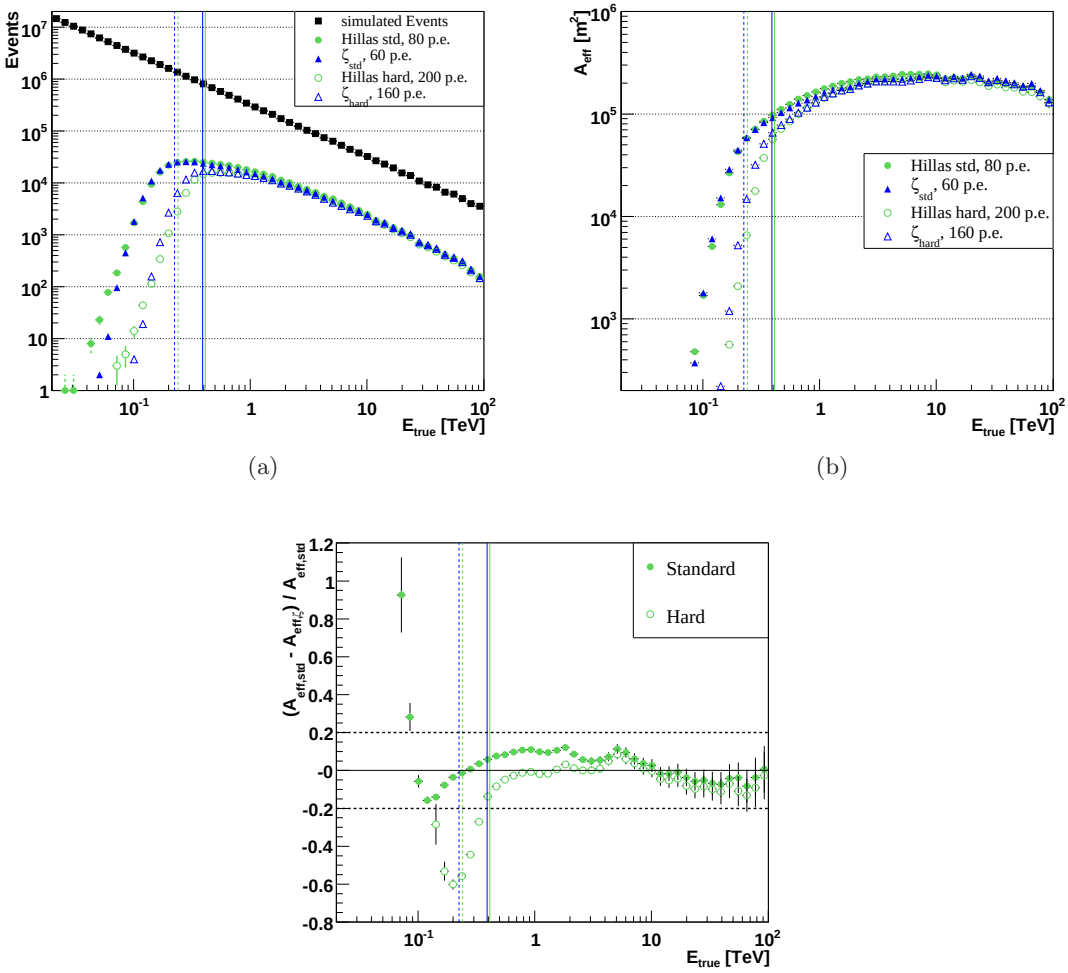

Figure 2.18: (a) Energy distribution of simulated Monte Carlo γ-ray events and number of events passing certain cuts and (b) Effective detection area $A_{\rm eff}$as a function of simulated energy for Monte Carlo γ rays at 20° zenith angle and 0.5° offset. (c) Relative difference in $A_{\rm eff}$ between Standard Analysis and ζ analysis for configuration Standard and Hard. Dashed, horizontal lines denote a 20% relative difference in $A_{\rm eff}$. Vertical lines indicate the *safe thresholds*.

the systematic studies performed in Sec. 2.4.2, the observations used for spectral analyses were not selected by zenith angle of the observation and cover a broader range $5° \leq \Theta_z \leq 60°$. Even though the observations were to a large extent conducted in wobble mode, a significant fraction of the data was obtained in observations of nearby sources or Galactic Scan observations at larger offsets to HESS J1745–290 (see also Fig. 2.19(a)). The differential spectra as resulting from the ζ- and Standard Analysis are shown in Fig. 2.20(a). The fit of an exponential cutoff power law to the ζ_{std} spectrum is indicated as black line. Table 2.5 summarises the obtained fit results with the spectral estimates as given in Aharonian et al. (2009a). Although the observations of the GC source were conducted over three years in a broad zenith angle range with several pointing offsets, the

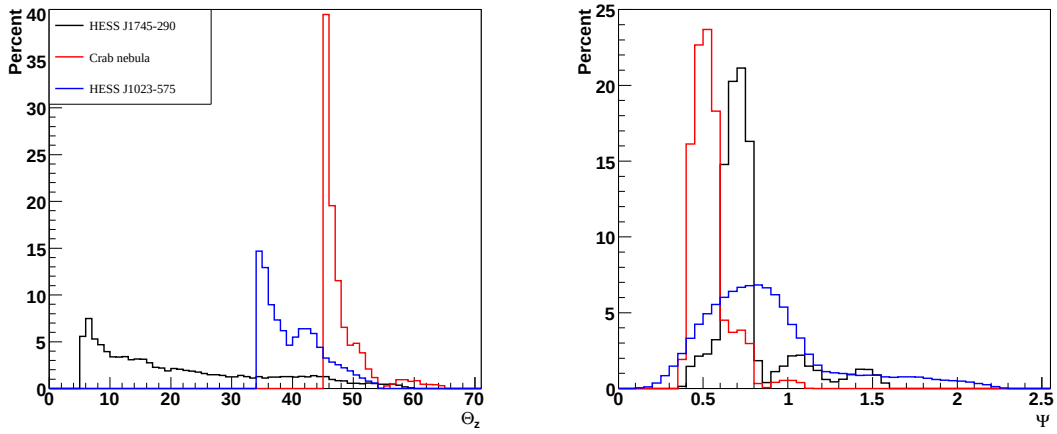

(a) (b)

Figure 2.19: (a) Zenith- and (b) offset distribution of events originating from HESS J1745–290, the Crab nebula and the extended source HESS J1023–575. The difference in the zenith distributions concern the covered range and the centroid. The broad offset distribution of HESS J1023–575 illustrates the extended nature of the source. HESS J1745–290 observations were conducted at different pointing positions.

Cuts	Φ_0 (10^{-12} TeV^{-1} cm^{-2} s^{-1})	Γ	E_{cut} (TeV)	$I(\geq 1$ TeV) (10^{-12} cm^{-2} s^{-1})	χ^2/d.o.f.
ζ_{std}	2.56 ± 0.07	2.17 ± 0.04	16.5 ± 3.2	1.83 ± 0.09	33/25
std	2.69 ± 0.08	2.10 ± 0.04	13.5 ± 2.3	1.92 ± 0.09	29/24
paper	2.55 ± 0.06	2.10 ± 0.04	14.7 ± 3.4	1.99 ± 0.09	23/26

Table 2.5: Flux and spectral measurements of the Galactic Centre source HESS J1745–290 for a power-law fit with exponential cutoff. Results obtained with the Standard Analysis and the ζ analysis are compared to the measurement given in Table 2 in Aharonian et al. (2009a).

resulting spectrum for the ζ analysis is in excellent agreement with the two other analyses. Moreover does the differential spectrum covered by the ζ_{std} cuts extends to energies of 30 TeV, compared to the Standard Analysis which just provides significant excess up to energies of 10 TeV.

Crab nebula

The data set used to derive the energy spectrum of the Crab nebula comprises observations conducted over a five-year period from 2004 to 2009, which add up to 21 hours live time[14]. The Crab nebula is a steady and strong VHE γ-ray emitter which is visible to H.E.S.S. at large zenith angles $\Theta_z \geq 45°$ due its northern-hemisphere position on the sky. It is

[14] The data set used in Aharonian et al. (2006a) also accumulates to 21 hours live time, but obtained in observations from late 2003 to late 2004.

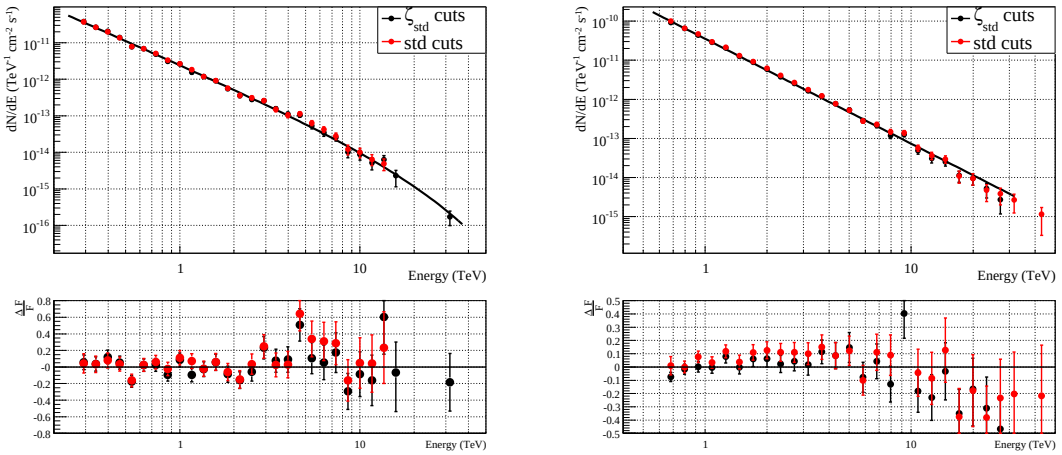

Figure 2.20: Differential energy spectrum and residua distribution of (a) HESS J1745–290 and (b) the Crab nebula as obtained with the ζ_{std}- and std cuts with 1σ statistical errors. The black line denotes the fit of a power law to the ζ_{std} spectrum in case of the Crab analysis and an exponential cutoff power law in case of the HESS J1745–290 analysis. All spectral points have a minimum significance of 2σ. Residua distributions show the difference between the best fit to the ζ_{std} points and the measurements.

hence a perfect target to test the spectral reconstruction and possible systematic effects of the ζ analysis at large zenith angles and with data with strongly varying thresholds. The differential spectra are shown in Fig. 2.20(b). Table 2.6 compares the results of a power-law spectral fit to the ζ_{std}- and std-cuts to the published measurements from H.E.S.S. (Aharonian et al. 2006a) and VERITAS (Celik 2008). Even though the published H.E.S.S. results and all other results agree with each other, one has to note that the large difference in fit quality (an exponential cutoff power law fit to the H.E.S.S. data yields a much better χ^2/d.o.f. of 16/9) could be explained by a different calibration procedure which was applied in the analysis of the original H.E.S.S. data compared to the calibration used in this work. Furthermore, a study performed by Meyer et al. (2010) compares the theoretical expectation of HE and VHE emission from the Crab nebula and measurements performed by the Fermi LAT instrument with the measured VHE γ-ray emission of different instruments, in order to cross-calibrate ground-based IACTs. Their analysis suggests a scaling factor of 0.97 in absolute flux for the spectrum published in Aharonian et al. (2006a) as well as a steeper spectral index without exponential cut off compared to the theoretical prediction. However, the spectra for the ζ_{std}- and std-cuts agree well with each other, the VERITAS spectrum and the studies performed in Meyer et al. (2010).

HESS J1023–575

A VHE γ-ray source coincident with the RCW 49/Westerlund 2 region has been detected in observations conducted by H.E.S.S. in 2006. The total live time of the data set accu-

Cuts	Φ_0 (10^{-12} TeV^{-1} cm^{-2} s^{-1})	Γ	$I(\geq 1$ TeV) (10^{-12} cm^{-2} s^{-1})	χ^2/d.o.f.
ζ_{std}	33.9 ± 0.8	2.64 ± 0.03	20.7 ± 0.6	73/51
std	34.5 ± 0.8	2.63 ± 0.03	21.2 ± 0.6	63/45
H.E.S.S. (PL)	34.5 ± 0.5	2.63 ± 0.01	21.1 ± 0.3	104/10
VERITAS	36.3 ± 1.5	2.54 ± 0.05	23.5 ± 1.2	19/15

Table 2.6: Flux and spectral measurements of the Crab nebula for a power-law fit. Results obtained with the Standard Analysis and the ζ analysis are compared to the H.E.S.S. results given in Table 6 in Aharonian et al. (2006a) and to the VERITAS measurement (Celik 2008).

Cuts	Φ_0 (10^{-12} TeV^{-1} cm^{-2} s^{-1})	Γ	$I(\geq 1$ TeV) (10^{-12} cm^{-2} s^{-1})	χ^2/d.o.f.
ζ_{std}	4.50 ± 0.30	2.58 ± 0.08	2.85 ± 0.24	18/8
std	4.42 ± 0.42	2.47 ± 0.10	3.00 ± 0.35	1.8/4
paper	4.50 ± 0.56	2.53 ± 0.16	2.94 ± 0.48	

Table 2.7: Flux and spectral measurements of HESS J1023–575 and a power-law fit with exponential cutoff. Results obtained with the Standard Analysis and the ζ analysis are compared to the results given in Aharonian et al. (2007a).

mulates to 13 hours and the source is found to be clearly extended with respect to the H.E.S.S. PSF. Since most of the Galactic sources detected by H.E.S.S. are of extended nature, HESS J1023–575 represents another type of objects, whose energy spectrum is repeatedly studied and can be checked for consistency with the ζ analysis. Additionally to the published data set, another 19 hours of data from observations performed in 2008 are considered, when extracting the spectrum. Table 2.7 summarises the results of a spectral fit to the data. Clearly, within statistical errors all fit parameters agree with each other and confirm, that the spectrum extracted with the ζ_{std} cuts well reproduces the published results. Furthermore shows the comparison with the H.E.S.S. Standard Analysis in Fig. 2.5.3 that the energy range covered by the ζ analysis is much larger. The fact, that the spectrum extracted from the ζ_{std} cuts is comprised of ten flux points which have a significance which exceeds 2σ, compared to six points in case of the std cuts already indicates that the BDT cuts have better sensitivity compared to the std cuts. The next section will qualitatively study the performance and sensitivity of the ζ analysis to consolidate and quantify the first hints of an improved γ/hadron separation apparent in the spectral analyses.

2.6 Sensitivity of the BDT classifier

The last sections demonstrated the applicability of the BDT approach for the analysis of VHE γ-ray data taken under various observational conditions and for spectral studies of sources with different characteristics. Some of the spectral results already indicated the improved separation power of the ζ cuts which is going to be investigated quantitatively in this section.

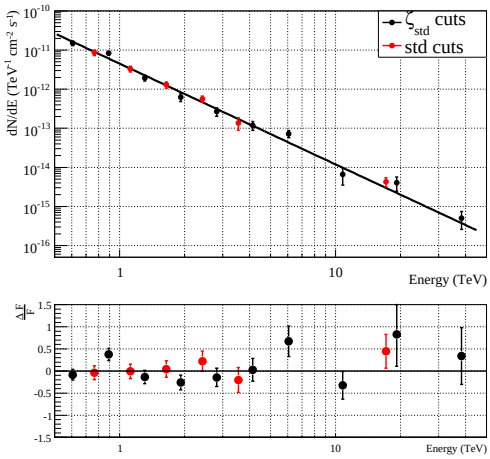

Figure 2.21: Differential energy spectrum and residua distribution of HESS J1023–575 as described in Fig. 2.20.

2.6.1 Separation power of ζ cuts

A parameter commonly used e.g. in particle physics and astronomy to quantify the quality of analysis cuts is the *quality factor* Q (e.g. (Bugayov et al. 2002)), defined as[15]:

$$\mathrm{Q} = \frac{\epsilon_\gamma}{\sqrt{\epsilon_{CR}}}, \tag{2.6}$$

$$\text{with} \qquad \epsilon_i = \frac{\hat{N}_i}{N_i} \qquad (i = \gamma \text{ or } CR). \tag{2.7}$$

Here, the cut efficiency ϵ_i is defined as the number of events passing certain cuts $\hat{N}_i$ divided by the number of events before applying the selection criteria N_i. Since the quality factor is independent of the count rate, it is a suitable parameter to quantify the quality of selection cuts, independent of the strength of a potential VHE γ-ray source.

Fig. 2.22 illustrates the dependence of the ratio Q_ζ / Q_{std} as a function of zenith angle, reconstructed energy and offset for configuration Standard and Hard after application of the *Preselection* cuts as well as image shape and ζ cuts, respectively (cuts summarised in Table 1.1 and 2.3). The training in energy- and zenith-angle bands provides a stable improvement in separation potential for the BDT classifier as a function of energy and zenith angle and proves the applicability of zenith- and energy-dependent cuts on ζ for the γ/hadron discrimination. Notably, for events of energies below $\approx$ 500 GeV and energies larger than a few TeV, the BDT clearly outperforms the H.E.S.S. Standard Analysis. This behaviour was already suggested by the spectral analyses presented in the previous section, were, especially for the case of HESS J1023–575, a remarkably wider energy range could be explored in the case of the ζ_{std} cuts. Since the BDT was trained with Monte Carlo γ rays at a fixed offset of 0.5°, the performance of the ζ cuts compared to the Standard Analysis is reduced for events with offsets $\geq$ 1.5° and becomes even worse than the hard-cuts in the case of the ζ_{hard} cuts (see Fig. 2.22(c)). However, the training in offset bands resulted in

[15] The definition of the quality factor Q is just valid in the background-dominated regime, for which $N_\gamma \ll N_{CR}$.

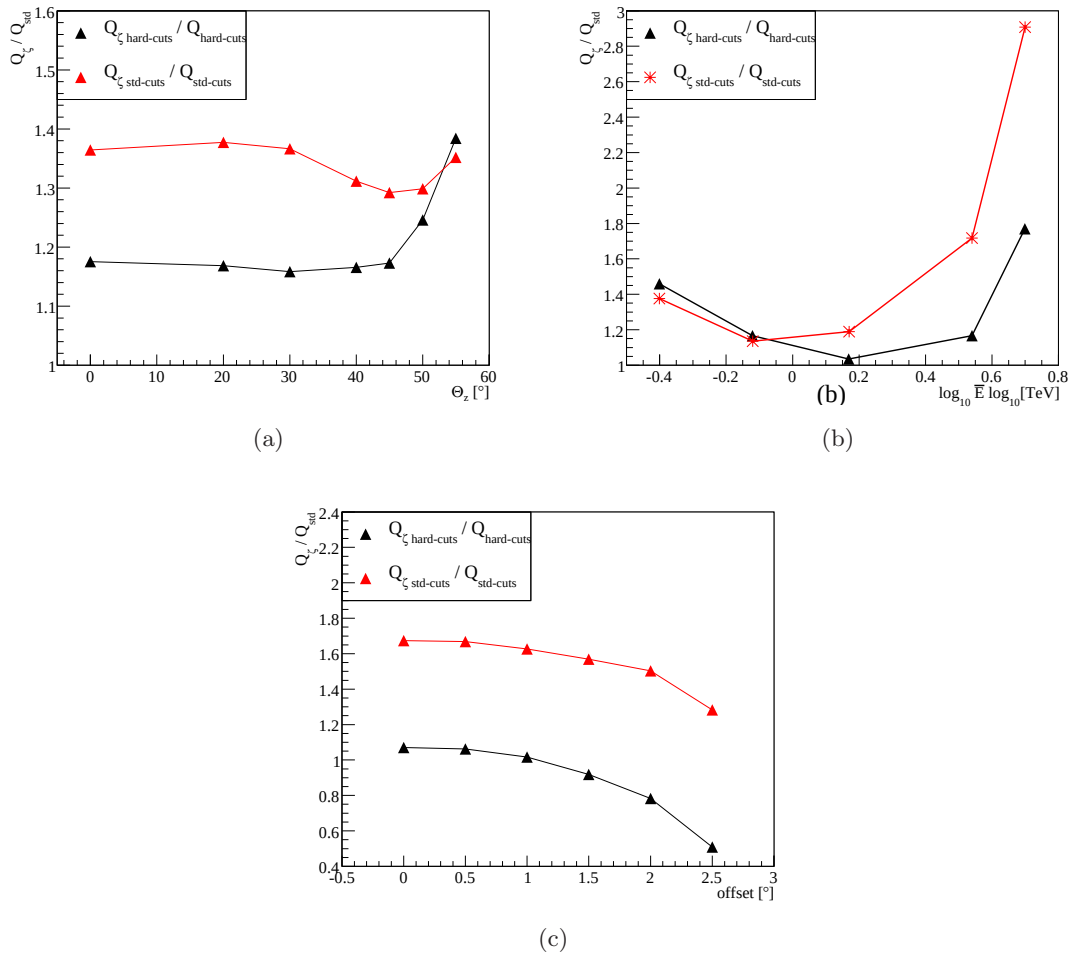

Figure 2.22: Improvement in Q-factor, defined as Q_ζ / Q_{std} (Q-factor described in the main text) versus (a) zenith angle, (b) reconstructed energy and (c) offset for the ζ analysis compared to the H.E.S.S. Standard Analysis. The values for Q are determined using the cut efficiencies for γ rays from simulations and background events from off source data in the specific zenith-angle-, reconstructed energy- and offset range (Figure (a) and (b) taken from Ohm et al. (2009b)).

an offset dependent γ-ray selection efficiency across the field-of-view and hence in artifacts in the description of the radial camera acceptance and is therefore not further employed in this work.

In order to further quantify the improvement in separation power, Table 2.8 summarises the signal and background statistics as obtained from the Reflected background method for the ζ cuts and the cuts applied in the H.E.S.S. Standard Analysis for HESS J1745–290, the Crab nebula and HESS J1023–575. The ζ cuts yield a γ-ray selection efficiency comparable to that obtained for the Standard Analysis, but with a greatly improved background rejection of the order of 1.5 (Crab nebula), 1.9 (HESS J1023–575) and 2.0 (HESS J1745–290) for configuration Standard. The situation is different in case of configuration Hard; here the background level for the Crab analysis is the same, whereas the γ-ray efficiency

Source	Analysis	N_{On}	$\alpha \cdot N_{Off}$	γ	σ	S/N
HESS J1745–290	std-cuts	12256	6968	5288	54.8	0.8
HESS J1745–290	hard-cuts	2963	667	2296	61.6	3.4
HESS J1745–290	ζ_{std}	8254	3519	4735	64.7	1.3
HESS J1745–290	ζ_{hard}	3070	693	2377	62.6	3.4
HESS J1745–290	ζ_{weak}	5786	2099	3687	63.1	1.8
Crab nebula	std-cuts	7753	722	7031	138	9.74
Crab nebula	hard-cuts	2725	71	2654	103	37.4
Crab nebula	ζ_{std}	7424	467	6957	149	14.9
Crab nebula	ζ_{hard}	3256	73	3183	114	43.6
Crab nebula	ζ_{weak}	6276	342	5934	139	17.4
HESS J1023–575	std-cuts	15065	13359	1706	12.8	0.13
HESS J1023–575	hard-cuts	2190	1574	616	12.8	0.39
HESS J1023–575	ζ_{std}	8633	7132	1501	15.1	0.21
HESS J1023–575	ζ_{hard}	2265	1666	599	12.2	0.36
HESS J1023–575	ζ_{weak}	6095	4916	1179	14.2	0.24

Table 2.8: Number of γ-ray-like and background events along with the performance of the applied cuts measured in significance, γ-ray excess and signal-to-noise ratio S/N. The results were obtained in the analysis of the data sets, introduced in Section 2.5.3.

is 20% higher in case of the ζ_{hard} cuts. Noticeably, the performance of the ζ_{hard} cuts is rather similar to the performance achieved with hard-cuts in case of HESS J1023–575 and HESS J1745–290. This effect can be understood as due to the extended nature of HESS J1023–575 and as resulting from the telescope pointing's at different offsets in case of the GC source. As already indicated in Fig. 2.22(c) the training of the BDT with Monte Carlo γ rays as resulting from a point-like source at an offset of 0.5° leads to a reduced performance at larger offsets, especially for the ζ_{hard} cuts.

2.6.2 Sensitivity of ζ cuts

Following the first performance tests based on VHE γ-ray data in the last section the optimised ζ cuts are subsequently applied to Monte Carlo γ-ray simulations and *Off data*, and their sensitivity for strong, std-spectrum and faint, hard-spectrum sources is going to be investigated in this section. As epitomised at the beginning of this chapter, a gain in separation information can be achieved in two ways: Either by introducing discrimination variables with additional separation power, or by using a classifier, which is able to properly treat non-linear correlations between input parameters in the classification. In order to disentangle the performance improvement from these two contributions in the BDT method, the sensitivity for optimised box cuts on all training parameters is examined as well. These box cuts are all optimised simultaneously to obtain the best separation between signal and background in every zenith angle- and energy band. Fig. 2.23 demonstrates the gain in separation power of the ζ cuts compared to the cuts applied in the H.E.S.S. Standard Analysis. Depicted is the observation time required for a detection of a point-like

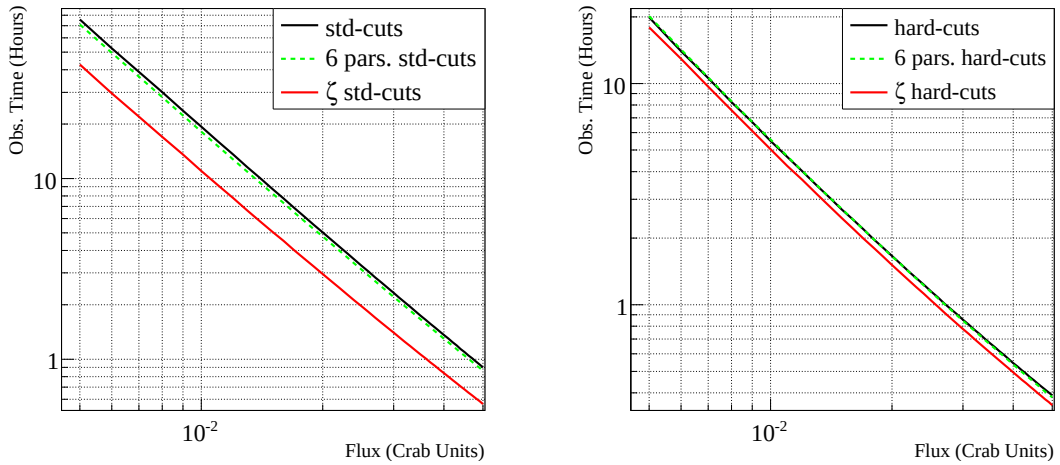

Figure 2.23: Improvement in Q-factor, defined as Q_ζ / Q_{std} (Q-factor described in the main text) versus (a) zenith angle and (b) reconstructed energy for the ζ analysis compared to the H.E.S.S. Standard Analysis. The values for Q are determined using the cut efficiencies for γ rays from simulations and background events from off source data in the specific zenith-angle- and reconstructed energy range (Figure taken from Ohm et al. 2009b).

VHE γ-ray source (signal with more than 5σ above background) with a flux between 0.5% and 5% of the flux of the Crab nebula, assuming a power law in reconstructed energy with a spectral index of $\Gamma = 2.63$ (as measured for the Crab nebula (Aharonian et al. 2006a), see Fig. 2.23(a)) and for a hard spectrum source with index $\Gamma = 2.0$ (see Fig. 2.23(b)) for the above mentioned sets of selection cuts. Notably, the optimised ζ cuts show the highest sensitivity over a wide range of source strengths. The required observation time for the ζ analysis is up to 45% and 20% less compared to the H.E.S.S. Standard Analysisfor configuration Standard and Hard, respectively. This gain in observation time translates into a point-source sensitivity, which is 20% and 10% better in the case of ζ_{std} and ζ_{hard} cuts, respectively. From Fig. 2.23 it gets also clear, that box cuts add just little to the overall separation gain, since they ignore non-linear correlations in the six training parameters.

Since the X_{max} parameter contributes especially at energies below a few hundred GeV to the classification (see Fig. 2.7 for comparison) and cuts optimised for hard-spectrum sources tend to reject low-energy events, the sensitivity improvement of the ζ_{hard} cuts is only 10% compared to the H.E.S.S.hard-cuts. Even though they have the weakness of the reduced performance at larger offsets, the improvement is stable over a wide range of fluxes for point-like sources. One possibility to further improve the BDT performance for hard-spectrum sources is to find the best match between size cut applied to select the training sample (see Section 2.3 for comparison) and size cut optimised for a given source type in an alternating process.

2.6.3 Conclusions and future prospects

In this chapter, the applicability of a decision-tree-based multivariate analysis method, namely the BDT, has been demonstrated on the basis of Monte Carlo simulations and real γ-ray data. The BDT approach leads to a significantly increased separation power compared to the H.E.S.S. Standard Analysis. Especially in the case of weak, steep spectrum sources, the ζ_{std} cuts have proven to achieve a 20% gain in sensitivity (or 45% in observation time). The zenith- and energy-dependent γ/hadron separation has proven to give a stable performance improvement for a wide range of observational conditions. As shortly outlined in Section 2.3 the inclusion of additional parameters with discrimination potential, as e.g. obtained in the Model3D or Model++ analysis, in the training process can further improve the BDT performance. Whereas the BDT used in this work utilises shower shape parameters which describe the global shower shape, parameters obtained in the Model++ and Model3D parameters store intrinsic shower properties on the camera pixel level and are hence only weakly correlated to the Hillas parameters. First tests of a BDT training including Hillas-based as well as Model3D parameters showed a greatly improved separation potential (Fiasson et al. 2010) and resulted in a sensitivity comparable to that obtained in the currently most sensitive analysis, the Model++ analysis (de Naurois & Rolland 2009). Another possible quantity, provided by an extended version of the Model3D method (Naumann-Godó et al. 2009), which can be utilised in the training of the BDT and which is not correlated to any other parameter discussed so far is the light yield as expected from the Model3D in non-triggered telescopes.

Systematic studies performed in this chapter and the achieved classification power demonstrate that an MVA approach such as the BDT is well suited for the analysis of γ-ray data measured with IACTs like H.E.S.S.. Near- and mid-term projects like H.E.S.S. II, MAGIC II, CTA and AGIS will extent the accessible energy range of IACTs as the reachable sensitivity increases. Multivariate methods can play a major role for the analysis and particularly for the γ/hadron separation, since the majority of the events will be recorded below a 100 GeV, where γ/hadron separation gets increasingly difficult. Parameters such as X_{max} demonstrate the ability to improve the performance of IACTs, especially for the separation at low energies.

3 Particle acceleration in massive star-forming environments

The long-standing mystery about the origin and acceleration mechanism of hadronic Galactic cosmic rays (GCRs) is still not fully settled. Though, the detection of VHE γ-ray emission from shell-type supernova remnants in the Milky Way such as e.g. Cassiopeia A (Aharonian et al. 2001; Albert et al. 2007a; Ergin & VERITAS Collaboration 2008; The VERITAS Collaboration et al. 2010), RX J1713–3946 (Aharonian et al. 2004c), RX J0852.0–4622 (Aharonian et al. 2007b), RCW 86 (Aharonian et al. 2009b) or SN 1006 (Naumann-Godó et al. 2008) supports the widely accepted idea that SNRs are indeed acceleration sites of GCRs. The underlying theory assumes that GCRs are injected into SNR shock fronts where they get accelerated via the diffusive shock acceleration (DSA) process up to energies of 10^{15} eV (Krymskii 1977; Axford et al. 1977; Bell 1978; Blandford & Ostriker 1978). In interactions with the ambient matter they then produce VHE γ rays which can be detected by IACT systems such as H.E.S.S..

It is commonly accepted that the bulk of the core-collapse SN progenitor stars form in groups and evolve from collapsing gas condensations inside giant molecular clouds (see e.g. Zinnecker & Yorke 2007, for a recent review). Depending on the total mass of the group of stars, these systems either form loosely bound *associations* or gravitationally bound *stellar clusters*. It was Montmerle (1979), who noted a correlation of some of the *COS-B* HE γ-ray sources with regions of massive star formation. Namely, the spatial coincidence of an SNR, associated with an OB association[1], and a nearby giant molecular cloud (a so-called "SNOB"). IC 443 and W 28 are such prototypal objects and have been detected and resolved with the new generation of HE γ-ray telescopes Fermi LAT (Abdo et al. 2010) and AGILE (Pittori et al. 2009). Interestingly, these two objects have also been detected in the VHE range by MAGIC (Albert et al. 2007b) and VERITAS (Acciari et al. 2009) in the case of IC 443 and by H.E.S.S. in the case of W 28 (Aharonian et al. 2008b). The measured γ-ray emission from MeV- to TeV energies seems to support the idea of GCRs accelerated in SNRs, producing π^0-decay γ rays in molecular cloud interactions.

On the other hand, SNR shells are not the only sites in the Galaxy in which particles can be accelerated via DSA to very high energies. An alternative scenario is particle acceleration in strong shocks in colliding wind binaries (CWBs). Massive stars do not only occur in associations and stellar clusters, they are also to a large extent bound in binary systems (e.g. Zinnecker 2003; Gies 2008). Generally, they exhibit a high mass-loss rate ($\dot{M} \approx 10^{-5} - 10^{-3}\ M_{\odot}\ \mathrm{yr}^{-1}$) and drive strong supersonic winds with terminal velocities $\mathrm{v}_{\infty} \approx 10^3$ km s^{-1}. When these winds in a binary system collide, they form a wind-wind interaction zone where charged particles can be accelerated to high energies

[1] O- and B stars are very hot, luminous and massive stars of spectral type O or B and usually form in groups or associations.

(e.g. Eichler & Usov 1993)). Electrons can then up-scatter stellar photons present in the wind collision zone via the Inverse Compton (IC) process to GeV energies (Mücke & Pohl 2002; Benaglia & Romero 2003; Reimer et al. 2006). On the other hand, relativistic nucleons can inelastically collide with thermal particles in the dense wind and produce π^0s which subsequently decay into VHE γ rays at a flux level, predicted to be detectable by state-of-the-art IACTs (Bednarek 2005).

Massive stars and CWBs mostly occur in stellar clusters or associations and predominantly stay their whole life close to their birthplaces, therefore, they strongly influence their environment. When the stellar winds of multiple massive stars in such systems collide, they form a collective bubble, also referred to as superbubble, filled with a hot ($T \sim 10^6$ K) and tenuous ($\rho \sim 5{\times}10^{-3}$ cm^{-3}) plasma (e.g. Weaver et al. 1977). At the wind interaction zones turbulences in the form of magneto-hydrodynamic (MHD) fluctuations and weak reflected shocks can build up. Unlike SNR shock-fronts and CWBs where GCRs are accelerated diffusively, turbulences in superbubble interiors can stochastically accelerate particles to very high energies (e.g. Bykov 2001). Moreover, massive stars undergo SN explosion after a few Myrs in the thin and hot superbubble environment, which might result in efficient particle acceleration at the boundary of the superbubble and/or at MHD turbulences, and further amplifies the already existing MHD turbulences (Bykov 2001; Parizot et al. 2004; Tang & Wang 2005; Higdon & Lingenfelter 2005; Dwarkadas 2008).

The most massive stellar clusters are also known as Starburst clusters, which refers to their galactic-scale twins, the Starburst (SB) galaxies. SB galaxies undergo an evolutionary phase of enhanced star formation and are characterised by an highly increased supernova rate in a very localised region compared to galaxies such as the Milky Way. Starburst regions are promising sites for particle acceleration and provide at the same time a high density of target material for *pp* interaction and the production of π^0-decay γ rays. Moreover, they drive kiloparsec-scale Galactic winds (Lehnert & Heckman 1996) induced by the SB activity in the Galactic nucleus. At the boundary between the Galactic wind and the cold inter-galactic medium, a strong shock is believed to form at which CRs can be re-accelerated to ultra high energies (UHE; $E > 10^{18}$ eV) efficiently.

In the following, the theoretical background of particle acceleration, propagation and HE/VHE γ-ray production in massive star forming environments is discussed in more detail. Starting from stellar-size systems, namely CWBs in Section 3.1, Section 3.2 addresses massive stellar clusters on intermediate scales, before in Section 3.3 the largest star-formation systems, namely SB galaxies are discussed.

3.1 VHE γ-ray emission from Colliding Wind Binaries

From the observational side, particle acceleration in the wind collision region of massive binary systems is suggested by the detection of non-thermal radio emission in a handful of objects (see De Becker 2007, for a collection). This indicates the existence of high-energy electrons with GeV energies in these systems. Furthermore, extended X-ray emission from the colliding wind region (CWR) of the Wolf-Rayet[2] (WR) binary WR 147 has been

[2] Wolf-Rayet stars represent the last evolutionary stage of massive stars before they end their lives as supernovae. Their upper layers have been peeled off by the strong winds of the star during the O or B

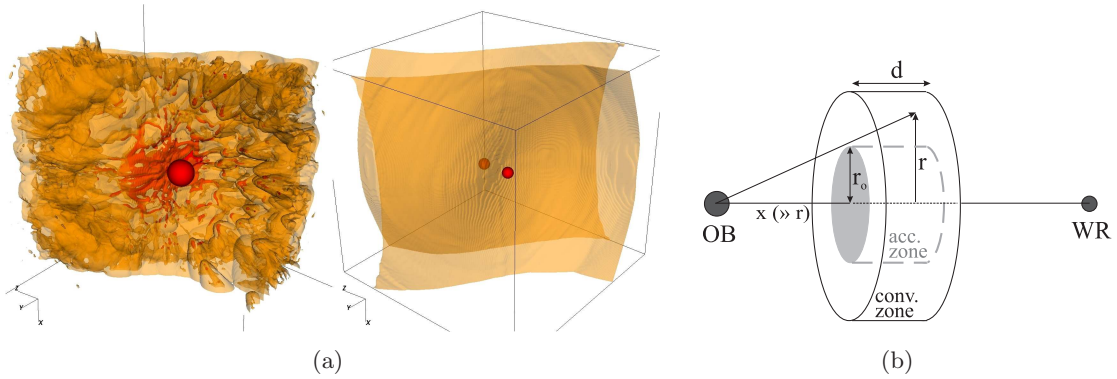

Figure 3.1: (a) 3D density contours with temperature and density surfaces shown in orange and red, respectively, for two different CWB systems, illustrating the complexity of current colliding wind hydrodynamical simulations (Figure taken from Pittard 2009). (b) 2D model, illustrating the geometry of the CWR with the acceleration- and convection zone (Figure taken from Reimer et al. 2006).

detected in observations with the Chandra satellite (Pittard et al. 2002).

The theory of particle acceleration to GeV energies in colliding winds of early type massive stars was developed in the early 1990's (e.g. Chen & White 1991; White & Chen 1992; Eichler & Usov 1993). Since then, further developments regarding more and more comprehensive modelling of production-, propagation- and energy-loss processes within these systems (see e.g. Mücke & Pohl 2002; Benaglia & Romero 2003; Reimer et al. 2006; Pittard et al. 2006) were undertaken, reaching a very high level of complexity. The 3-dimensional hydrodynamical simulations e.g. performed by Pittard (2009) incorporate wind driving, gravity, orbital motion of the two companion stars as well as radiative cooling of the shocked plasma (see Fig. 3.1(a) for illustration). In this section, a simple geometrical model of a CWB is presented. In this framework, acceleration- as well as energy-loss processes for electrons and protons are derived. The spectral energy distributions (SEDs) of HE- and VHE γ rays as resulting from IC scattering of electrons and π^0 decay of proton interactions and their detectability with IACTs is discussed in more detail.

3.1.1 Geometrical model of a stellar wind collision region

Let's assume an early-type, massive binary system, composed of two stars of WR- and OB-type, which exhibit mass loss rates $\dot{M}_{\rm OB,WR}$ and drive radially outflowing winds, which have reached their terminal velocity $v_{\rm OB,WR}$. When the two winds collide, they form a contact discontinuity (CD) with forward and reverse shock at the location of ram pressure balance. The distance from the shock front to the two stars $x_{\rm WR,OB}$ is then defined as:

$$x_{\rm WR} = \frac{D}{1+\sqrt{\eta}}\ , \qquad x_{\rm OB} = \frac{D\sqrt{\eta}}{1+\sqrt{\eta}}\ , \tag{3.1}$$

phase.

with the dimensionless parameter η, describing the wind-momentum ratio of the two stars, and the binary separation D:

$$\eta = \frac{\dot{M}_{\rm OB} v_{\rm OB}}{\dot{M}_{\rm WR} v_{\rm WR}} \ , \qquad D = x_{\rm WR} + x_{\rm OB} \ . \tag{3.2}$$

The magnetic field strength B near the CWR depends on the distance to the star r, its radius r_s, surface magnetic field B_s, surface rotation velocity v_s and the Alvén radius r_A:

$$B \approx B_s \times \begin{cases} (r_s/r)^3 & \text{for} \quad r_s \leq r \leq r_A \ \text{(dipole)} \\ r_s^3/(r_A r^2) & \text{for} \quad r_A < r < r_s(v/v_s) \ \text{(radial)} \\ (v_s r_s^2)/(v r_A r) & \text{for} \quad r_s(v/v_s) < r \ \text{(toroidal)} \end{cases} \tag{3.3}$$

Even though surface magnetic fields of early-type stars are not well known, reasonable estimates suggest B_s of $\mathcal{O}(100)$ G. Depending on the binary separation, this implies magnetic fields at the CD of $\mathcal{O}$(1–10) G for close and wide binary systems, respectively (Eichler & Usov 1993). The CWR can be described as consisting of two distinct zones, which are illustrated in Fig. 3.1(b). In the *acceleration zone*, thermalized stellar-wind particles in the CWR gain energy via the DSA process. Subsequently, spatial diffusion efficiently transports these particles outwards to the boundary of the acceleration region. In the adjacent *convection zone*, particle streaming along the CD occurs and dominates over diffusion processes. The characteristic radius r_0 between acceleration- and convection zone is defined as the radius, where the diffusion timescale $\tau_{\rm diff}$ is equal to the convection timescale $\tau_{\rm conv}$. In the following, the particle acceleration process in the acceleration zone is discussed in more detail.

3.1.2 Particle acceleration and HE/VHE γ-ray spectra

The idea of particle acceleration in astrophysical shocks via Fermi acceleration was originally introduced by Fermi (1949) and further developed to the diffusive shock acceleration theory by several independent groups (Krymskii 1977; Axford et al. 1977; Bell 1978; Blandford & Ostriker 1978). Particles in the acceleration zone in the CWB with energy E_0 are accelerated via the DSA process at a rate of $\dot{E} = aE$, where a depends on the compression ratio and upstream velocity of the shock and the diffusion coefficient perpendicular to the wind CD κ_d. Burst-like injected particles[3] gain energy via DSA and diffuse out of the acceleration region within the escape time $T_0 = r_0^2/(4\kappa_d)$, where r_0 is defined as free-escape boundary as illustrated in Fig. 3.1(b). Solving the corresponding continuity equation, the energy distribution of particles is than given as (Reimer et al. 2006):

$$N(E) \propto E^{-s} f_c(E) \ . \tag{3.4}$$

Equation 3.4 has a power-law form with index $s = (aT_0)^{-1} + 1$ and a modification term $f_c(E)$ which accounts for radiative losses. These radiative losses can be strong in this environment given the high radiation fields in the stellar winds. At the point where convection of particles along the wind CD is faster than diffusion of particles, the continuity equation

[3] Burst-like injection is a good approximation since the accelerated particle spectrum is mainly determined by the parameters describing the acceleration process, rather than the injection spectrum of particles (Reimer et al. 2006).

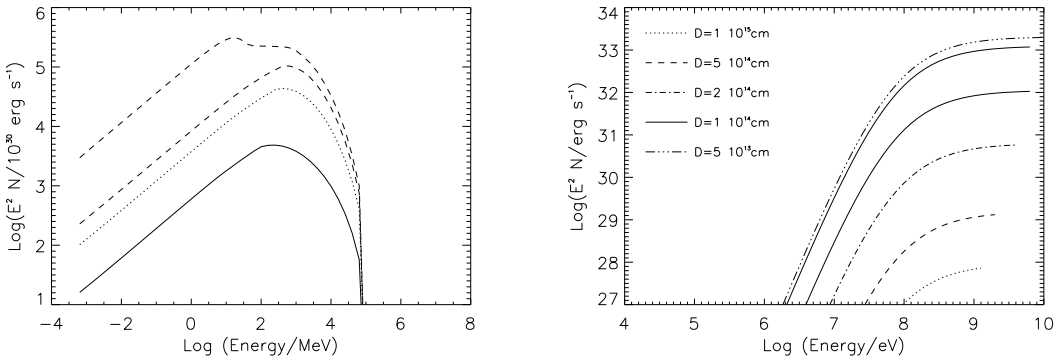

(a) (b)

Figure 3.2: (a) IC γ-ray spectra from the acceleration region for various orbital phases (defined as the angle between the line connecting the two stars and the line of sight of the observer ϕ) as obtained by Reimer et al. (2006). The solid line represents a geometry, where the WR star is placed in front of the observer $\phi = 0°$. The dotted line is $\phi = 90°$, the lower dashed line $\phi = 180°$. The upper dashed line represents the volume-integrated, combined IC γ-ray spectrum from acceleration- and convection region for $\phi = 180°$. (b) π^0-decay γ-ray spectra for varying binary separations from 5×10^{13} cm to 1×10^{15} cm. Note the increasing maximum γ-ray energy with increasing binary separation.

has to be modified to additionally include adiabatic energy losses. At r_0, diffusion- and convection timescales are equal and allow to derive the power-law index s. Interestingly, Reimer et al. (2006) find a hard index $s \leq 2$ assuming isotropic diffusion and strong shocks.

The accelerated electrons lose energy via three processes: At low energies Bremsstrahlung and Coulomb losses dominate, whereas at high energies electrons predominantly lose energy via IC scattering off UV photons in the dense photospheric radiation field. Fig. 3.2(a) illustrates the resulting IC γ-ray spectra from keV to TeV energies. Clearly, for a given binary separation, the maximum flux depends on the orbital phase of the CWB system. On the other hand, the maximum γ-ray energy changes with the orbital separation of the two stars. Note, the peak of the IC γ-ray spectra is around 100 MeV and at a flux level of $\mathcal{O}(10^{32} - 10^{35})$ ergs s^{-1}. In this model, the maximum γ-ray energy from IC scattering of electrons is with ~ 100 GeV right at the edge between the HE regime, covered by Fermi, and the VHE regime, with IACTs operating at 100 GeV – 100 TeV energies.

On the other hand, also protons are accelerated in the CWR and can interact with particles in the stellar winds, apparent in the shock region. These collisions are very rare (a few times per year for gas densities typical for long-period binaries such as WR 140) and occur with an energy-loss rate which is approximately:

$$\dot{E} = -b_{\rm pp} E \ , \tag{3.5}$$

above the threshold energy for pion production $E > E_{th} \simeq 0.28$ GeV. $b_{\rm pp}$ linearly depends on the inelastic proton-proton cross section $\sigma_{\rm pp}$, the target ion density $N_{\rm H}$ and the proton-to pion mass ratio m_π/m_p[4]. The resulting proton spectra in the acceleration region show

[4] At energies below ~ 10 GeV this linear relation is just an approximation. Furthermore, Coulomb losses

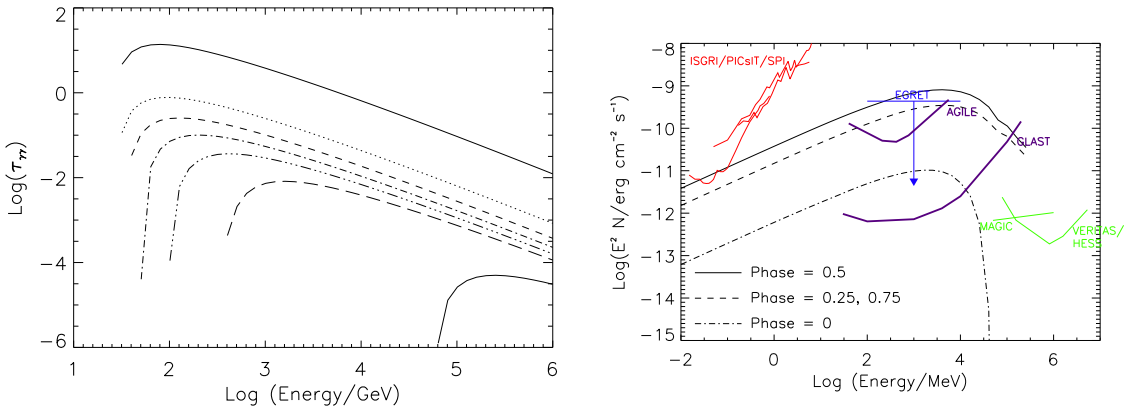

(a) (b)

Figure 3.3: (a) $\tau_{\gamma\gamma}$ as a function of γ-ray energy for a fixed binary separation and the line-of-sight angle θ_L for $\theta_L = 0°$ (lower solid line), $\theta_L = 30°$ (long-dashed line), $\theta_L = 60°$ (double-dot-dashed line), $\theta_L = 90°$ (dashed-dotted line), $\theta_L = 150°$ (dotted line), and $\theta_L = 180°$ (upper solid line) (Figure taken from Reimer et al. 2006). (b) IC spectra as resulting from the model presented in Reimer et al. (2006) for WR 147 at different orbital phases.

a similar power-law form as the electron spectra, but without the modification at the high-energy end since energy losses via *pp*-interactions and energy gain via DSA have the same energy dependence. The resulting π^0-decay γ-ray spectra for different CWB binary separations are shown in Fig. 3.2(b). Protons only transfer a fraction of $\kappa_\pi \approx 0.17$ of their kinetic energy into the production of pions in *pp* interactions (Aharonian 2004). This leads to a maximum π^0-decay γ-ray energy considerably lower than the threshold energy of IACTs of $\sim$ 100 GeV. Moreover, the low collision rates result in a π^0-decay γ-ray luminosity of $\mathcal{O}(10^{33})$ ergs s^{-1} for typical CWBs parameters, which is two orders of magnitude lower than the maximum reachable luminosity in case of the IC process.

Above energies of $\approx$ 100 GeV, photons generated via IC scattering of highly-relativistic electrons and via decay of π^0's produced in *pp*-interactions suffer from $\gamma\gamma$ absorption in the dense stellar radiation fields of the stars. This modifies the VHE γ-ray spectrum as $\exp(-\tau_{\gamma\gamma}(E_\gamma))$. As illustrated in Fig. 3.3(a), both, the amplitude and peak of the $\gamma\gamma$ pair production opacity changes with the line-of-sight angle θ_L. The larger θ_L, the lower $\tau_{\gamma\gamma}$ and the higher the peak energy of $\tau_{\gamma\gamma}$.

3.1.3 Detectability with IACTs

Exemplarily, Fig.3.3(b) shows the broadband SED of the CWB WR 147 for the IC contribution of electrons at different orbital phases. The flux variations are due to the anisotropic nature of the IC scattering for an assumed inclination of the system of $i = 90°$ and eccentricity of $e = 0$ (see Reimer et al. 2006, for further information). In the HE γ-ray domain, this system is predicted to be detectable with Fermi and AGILE during all orbital periods. Although a cut-off around a few hundred GeV is predicted, flux levels are,

in the dense photosphere of the winds will modify the proton injection spectrum at MeV energies.

for certain orbital phases, at a level detectable by state-of-the-art IACTs. In the VHE domain, the detection of a CWB would put strong constrains on the maximum reachable particle energy and hence the acceleration efficiency in such a system. However, from the observational side, only upper limits have been reported by the MAGIC collaboration for VHE γ-ray emission from WR 146 and WR 147 (Aliu et al. 2008). The H.E.S.S. collaboration observed another CWB, namely η Carinae, and Chapter 4 in this work is dedicated to the search of VHE γ-ray emission from this system, which is visible for H.E.S.S. due its southern-hemisphere location on the sky.

3.2 VHE γ-ray emission from young massive stellar clusters

As outlined in the beginning of this chapter, massive stars form and evolve predominantly in (OB-) associations and stellar clusters. Moreover, a large fraction of these stars are bound in binary systems in which particle acceleration as described in Section 3.1 can occur. After the formation of massive stars from the natal molecular cloud, their strong winds blow the remaining cloud material away which leads to the formation of a *superbubble*, filled with a hot and tenuous plasma (Weaver et al. 1977). After $\sim 1 - 10$ Myrs, massive stars end their lives as supernova explosions in this environment. Higdon & Lingenfelter (2005) derive that a fraction of 75% of all Galactic supernovae occur within these environments. Therefore, it is suggestive that a major fraction of GCRs could have their origin in superbubbles. This section focuses mainly on large scale particle acceleration in the superbubble interior. First, a geometrical model of a bubble blown by a single massive star is introduced and then generalised to the case of a superbubble. The density and temperature inside a superbubble and the effect on SN evolution, particle acceleration as well as γ-ray-production are discussed in more detail.

3.2.1 Formation of a superbubble

Weaver et al. (1977) introduced a simple model, describing the geometry and physical properties of a bubble blown by a single massive star under the assumption of a steady, radially symmetric wind with terminal velocity v_∞, which interacts with the surrounding ISM of constant-density. The resulting interstellar bubble consists of four different zones which are exemplarily shown in Fig. 3.4(a). Starting from the stars position it is *(a)* the supersonically expanding stellar wind region, *(b)* the region of the shocked stellar wind, *(c)* the shocked stellar gas, arranged in a shell and *(d)* the surrounding ISM. A short period of very fast expansion of the bubble, where radiative losses do not have enough time to affect the structure and evolution of the system, lasts for $\mathcal{O}(10^3)$ yrs (see Weaver et al. 1977, and references therein). This period is followed by a semi-adiabatic phase in which radiative losses cause the pushed-away, high-density material to collapse, forming a thin shell of shocked gas. The energy stored in the shocked stellar wind region, however, is not radiated away and gets conserved in this region. In a last evolutionary stage, radiative losses also influence the shocked stellar wind region and its dynamics.

Following Parizot et al. (2004), the outer radius of the shocked interstellar gas is a function

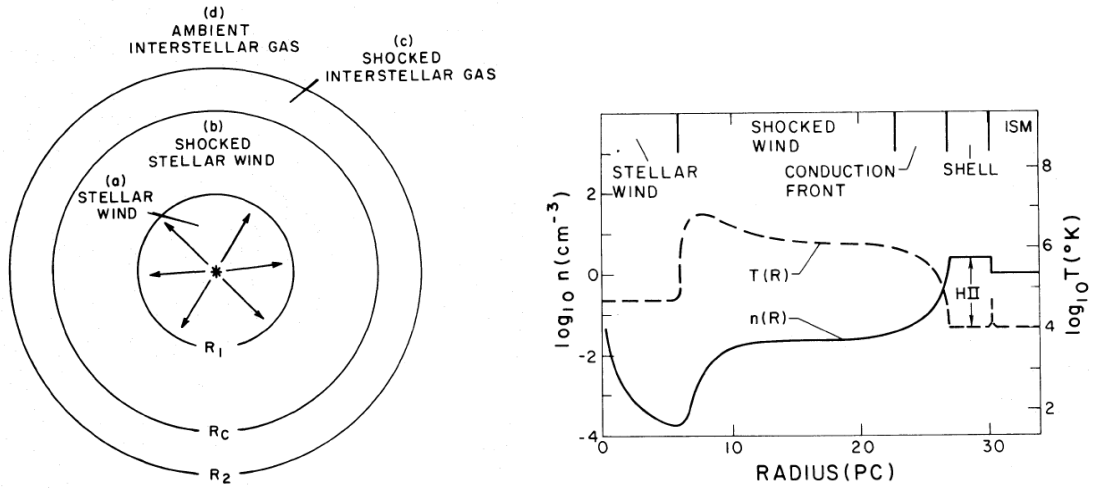

Figure 3.4: (a) Sketch illustrating the geometry of a bubble, blown by a massive stellar wind into the surrounding ISM. (b) Density- and temperature profiles of the bubble blown by an O7-type central star after 1 Myr (Figures taken from Weaver et al. 1977). See text for further details.

of time and can be estimated as:

$$R_{\rm ext} = (13\ {\rm pc}) t_{\rm Myr}^{3/5} \left(\frac{L_{\rm wind}}{3\times10^{36}{\rm erg/s}}\right)^{1/5} \left(\frac{n}{10^2{\rm cm}^{-3}}\right)^{-1/5} . \tag{3.6}$$

The mean distance between two stars in an OB association is with

$$R_\star = (6\ {\rm pc}) \left(\frac{R_{\rm OB}}{35\ {\rm pc}}\right) \left(\frac{N_{\rm OB}}{100}\right)^{-1/3} \tag{3.7}$$

much smaller compared to the radius of the shocked stellar gas (Parizot et al. 2004). Hence, single stellar bubbles merge and form a collective stellar bubble, the superbubble, within the first 1 Myr after their formation. This means that the superbubble blown by the winds of multiple massive stars in a stellar cluster can be seen as a scaled-up version of a interstellar wind bubble blown by a single star.

3.2.2 Characteristics of a superbubble

Collective stellar winds

Weaver et al. (1977) have shown that the temperature- and density profiles in an interstellar bubble follow a radial dependence as shown in Fig. 3.4(b). The innermost region is described by a gas of constant temperature T, with a density n that drops $\propto r^{-2}$, as resulting from the continuity equation. The stellar wind encounters a shock at a radius $R(t)$ with a density and temperature discontinuity. The shocked-wind region is characterised by a very high temperature ($T \gtrsim 10^6$ K) and a low density. Adjacent to this region and separated by a thermal conduction region, where energy is transported away from

the inner shock region to region (b), is the thin shell of shocked stellar gas with higher density and lower temperature compared to region (b). Mac Low & McCray (1988) as well as Parizot et al. (2004) extended the model used by Weaver et al. (1977) (steady, radially symmetric wind blowing into the constant-density ISM) to estimate the temperature, density and pressure inside a superbubble[5]. As a result, Parizot et al. (2004) find that the free wind termination radius $R_{\rm term}$ is for stars with $M > 35\ M_\odot$ smaller than $R_\star$, and therefore, stellar winds of massive stars directly interact with each other forming growing plasma waves and subsequently strong turbulence as well as MHD turbulence. Moreover, Dwarkadas (2008) has shown by means of two-dimensional hydrodynamic simulations that up to 20% of the wind kinetic energy can be transferred into this turbulences and non-radial motions, when massive stars enter the WR phase. At these turbulent structures, turbulent particle acceleration can occur via the Fermi II process (Fermi 1949).

Supernovae inside superbubbles

The evolution of a SNR expanding into a superbubble is described by the same physical laws as of an isolated SNR. However, given the lower density inside a superbubble compared to the ISM, the superbubble SNR shell will enter the Sedov phase at later times, given the $t \propto n^{-1/3}$ dependence of the transition time. The SNR will also expand in a medium with higher sound speed due to the higher temperature (in a plasma, $c_s \propto T^{1/2}$) (e.g. Parizot et al. 2004; Tang & Wang 2005)).

Two important results can be derived from this scaling: *(1)* The SNR shell inside a superbubble becomes subsonic before entering the radiative phase, and *(2)* The forward shock of a SN exploding in the superbubble will never reach the outer superbubble shell and will transfer energy into heat and sonic waves (Parizot et al. 2004). In other words, the SN explosion energy is not radiated away, but stays as internal energy in the superbubble. And in particular, due to the turbulent, non-uniform structure of the superbubble interior, energy stored in the expanding SNR shell will be transformed into additional turbulence and MHD waves.

3.2.3 Particle acceleration and γ-ray production inside a superbubble

Compared to the situation in isolated SNRs, the DSA process inside a superbubble is presumably modified due to the following characteristics: *(1)* Since the SNR free-expansion phase is longer, also the acceleration time is longer and hence, the maximum reachable particle energy could be higher. *(2)* Due to already existing turbulences and higher magnetic fields in the superbubble interior, the injection mechanism of particles is presumably more efficient (Parizot et al. 2004). Furthermore, low-energy (up to TeV energies) particles within the superbubble may experience multiple shock acceleration processes, in case their diffusion timescale is smaller than the time between two subsequent SN explosions. On the other hand, Dorfi & Völk (1996) studied the particle acceleration in SNRs in elliptical galaxies which also evolve in a low-density, high-temperature medium and found that DSA models alone (without taking into account turbulence and MHD effects) predict

[5] They ignore external magnetic fields, inhomogeneous environments, clumping, density gradients, etc. in their simulations.

that only a very low fraction of kinetic energy is transferred into the acceleration of CRs. This can be understood since in such an environment the sound speed is higher and the maximum reachable Mach number is lower compared to shocks evolving in higher-density, lower-temperature media. When considering turbulent particle acceleration in the superbubble environment, a peak in the acceleration efficiency is predicted a few 10^5 yrs after the first turbulence from the colliding winds of massive stars has formed (Bykov 2001). The produced high-energy particles can either interact with dense surrounding shells of pushed-away material or with the wind interaction regions, which in this scenario act as target material and at the same time as acceleration region. γ rays can be produced in these interactions via π^0 decay or by non-thermal Bremsstrahlung. Recent investigations based on Monte Carlo simulations, which take into account diffusive- and turbulent particle acceleration as well as particle escape (Ferrand & Marcowith 2010), indicate that accelerated proton spectra can have a complex structure. In their model, the spectra strongly depend on the history of a given superbubble, e.g. the time since the last SN explosion. However, spectra as resulting from these simulations in general show a hard spectral index at low energies, a spectral break and steeper spectra at high energies. This is a consequence of the interplay between (re-) acceleration and escape of particles. The transition depends on bubble parameters like the magnetic field, acceleration region size, density and external turbulence scale. Given all these results, VHE γ-ray spectra possibly measured from these regions would resemble spectral features like e.g. the spectral break. Chapter 5 in this work is dedicated to the analysis of the young massive stellar cluster Westerlund 1 and its surroundings and possibly associated superbubble in VHE γ rays.

3.3 VHE γ-ray emission from Starburst galaxies

Contrary to the situation in the Milky Way where star formation predominantly occurs in the spiral arms, SB galaxies are characterised by a high supernova explosion rate in the central region of the galaxy, the so-called *Starburst region*. It is widely believed that this SB activity is caused by the process of a merger- or a close fly-by of galaxies, where the gas dynamics is distorted, leading to the formation of regions of very high gas density and subsequent star formation and/or Galactic bar instabilities like e.g. in the SB galaxy NGC 253. In this section, the two main constituents important for particle acceleration, namely the SB region and the Galactic wind, are introduced, after which the CR acceleration, the energy-loss processes and the predicted γ-ray emission is discussed in more detail. Since the archetypal SB galaxy on the southern hemisphere NGC 253 is partially subject of this work, all quantities given in the following were derived using measurements of NGC 253. A detailed discussion on NGC 253 is given in Chapter 6.

3.3.1 Characteristic regions

NGC 253's SB region has a cylindrical shape with $\sim$ 150 pc radius and $\sim$ 60 pc height, following Weaver et al. (2002), and is driven by a SN rate much enhanced compared to the SN rate in our own Galaxy. In a simplified picture, particle acceleration in the spiral arms of the SB galaxy can be neglected, and only acceleration of CRs originating from SN explosions in the central nucleus is considered. The knowledge of the SN rate ν_{SN}

Figure 3.5: Colour-coded image of the central region of the SB galaxy M 82. Blue, green and red filters illustrate optical emission as measured with the Hubble Space Telescope, pink colours denote HI emission as measured with the ground-based WIYN Telescope. The Galactic wind streaming out perpendicular to the Galactic disc can be seen. (Image courtesy: Mark Westmoquette, University College London; Jay Gallagher, UW-Madison; Linda Smith, University College London; WIYN/NSF; NASA/ESA).

in the SB region is of crucial importance when calculating non-thermal processes in this environment. The large population of massive stars in the central SB region implies very large photon fields and hence a very high luminosity in far infrared (FIR) wavelengths. Van Buren & Greenhouse (1994) found a proportionality between FIR luminosity and ν_{SN} and used this to estimate a $\nu_{SN} \approx 0.08$ yr^{-1} for NGC 253. The SN rate found in the small SB volume has to be compared to the SN rate in the whole Milky Way which is of the same order of magnitude. Combined with the estimate that 70% of the total supernova activity has its origin in the SB nucleus (Melo et al. 2002), the total star formation rate (SFR) in the SB nucleus alone amounts to 5 $M_{\odot}$ yr^{-1}. The fast frequency of subsequent SN explosions heat the surrounding material and accelerate CRs. Together, they drive a Galactic wind on kiloparsec-scale.

Analogous to superbubbles, in SB nuclei stellar winds of massive stars and SN activity thermalizes and pushes away the surrounding material. Due to the larger scales in SB galaxies, this collective effect manifests itself in a kiloparsec-scale Galactic wind[6] which pours out of the Galactic disc. Thereby, mass, heat and heavier elements are effectively transported out of the SB galaxy into the low-density inter-galactic medium (IGM). A colour-coded image of the central region of the SB galaxy M 82, the nearest northern-hemisphere SB galaxy, as measured with the Hubble Space Telescope and its Galactic wind as resolved by observations conducted with the WIYN Telescope is shown in Fig. 3.5.

[6] Which has to be compared to the typical scales of superbubbles of $\mathcal{O}(100)$ pc

3.3.2 Cosmic-ray acceleration in SB galaxies

As mentioned above, there are two main mechanisms, which effectively accelerate CRs to very high energies in SB galaxies: *(1)* Acceleration of particles in individual SNR shells and *(2)* DSA at the termination shock, which is believed to be formed at the boundary between the Galactic wind and the cold, low-density IGM[7].

Under the assumption that a single SN explosion transfers a fraction ϵ_{CR} of its initial explosion energy E_{SNR} into the acceleration of CRs, the energy input in CRs in the SB nucleus E_{CR} can be estimated from the supernova rate ν_{SN} as:

$$F_{CR} = \nu_{SN} \cdot \epsilon_{CR} \cdot E_{SNR} \ . \tag{3.8}$$

Assuming the standard conversion efficiency of $\epsilon_{CR} = 0.1$, an initial explosion energy of 10^{51} erg and the measured supernova rate for NGC 253 of $\nu_{SN} \approx 0.08$ yr^{-1}, the luminosity in hadronic CRs is $F_{CR} \approx 2.56 \times 10^{42}$ erg s^{-1}.

CRs accelerated in the SNR shock waves might reach maximum energies of 10^{15} eV and are then carried by the Galactic wind to its termination shock. Here, they get re-accelerated to energies of up to $\approx 3 \times 10^{20}$ eV, as suggested by simulations performed by Anchordoqui et al. (1999). For simplicity, and since this work only concerns CR energies up to the knee, the Galactic wind acceleration is not taken into account in the following considerations.

3.3.3 Cosmic-ray energy-loss processes in SB galaxies

The population of CRs accelerated in SNRs predominantly loses energy via convection, due to escape of particles from the Galactic wind and due to diffusion of particles. The timescale of the former mechanism is given by the ratio of Galactic wind scale height h_{GW} and velocity v_{GW}. For NGC 253, these values are estimated as 60 pc and 900 km s^{-1}, respectively (see Weaver et al. 2002; Zirakashvili & Völk 2006). This leads to a convection timescale of

$$\tau_{\rm conv} = h_{GW}/v_{GW} \approx 6.5 \times 10^4 \text{ yrs} \ . \tag{3.9}$$

Following Aharonian et al. (2005c), the timescale for diffusive losses is given by

$$\tau_{\rm diff} = h_{GW}^2/\kappa = 1.4 \times 10^5 \left(\frac{E}{1 \text{ TeV}} \right)^{-1.1} \text{ yrs} \ , \tag{3.10}$$

where κ is the diffusion coefficient. For a 1 TeV proton, the effective loss time $\tau_{\rm loss}$ as resulting from convection and diffusion is then estimated to be

$$\tau_{\rm loss} = \frac{1}{1/\tau_{\rm conv} + 1/\tau_{\rm diff}} \approx 4.4 \times 10^4 \text{ yrs} \ . \tag{3.11}$$

This number has to be compared to the timescale as resulting from the *pp* interaction cross section, which can be approximated to (see also Eq. 3.5)

$$\tau_{pp} \approx 5.3 \times 10^7 \ \left(\frac{n_{\rm H}}{\rm cm^{-3}} \right)^{-1} \text{ yrs} \ . \tag{3.12}$$

[7] Additionally, as described in the previous section, also turbulent particle acceleration can occur in such an environment. For simplicity, a possible contribution is neglected in the following.

Obviously, this timescale strongly depends on the ambient medium density $n_{\rm H}$. With an assumed proton density in the SB region of NGC 253 of 580 cm^{-3} (Engelbracht et al. 1998), $\tau_{pp} \approx 9.1 \times 10^4$ yrs is of the same order of magnitude as the energy-loss time for convection and diffusion. In the *calorimetric* limit, energy loss due to diffusion and convection is neglected and it is assumed that all the proton energy is lost in inelastic proton-proton interactions. By adopting the calorimetric limit for NGC 253, the γ-ray emissivity F_γ can be easily calculated from the CR energy input F_{CR}. It has to be noted that NGC 253 is not a fully calorimetric system.

3.3.4 γ-ray emission as resulting from nucleonic interactions

In this section the calorimetric γ-ray emissivity of NGC 253 will be computed. Given the CR energy input in the form of SNe of F_{CR} as calculated from Eq. 3.8, and a energy conversion into π^0 production and subsequent decay into γ rays, the measurable F_γ on Earth can be calculated as:

$$F_\gamma = \frac{1}{3} \cdot \frac{1}{4\pi D^2} \cdot F_{CR} \approx 8.2 \times 10^{-11} \text{ TeV cm}^{-2} \text{ s}^{-1} \ , \tag{3.13}$$

considering a distance of 2.6 Mpc to NGC 253 (Engelbracht et al. 1998). Neglecting diffusion and convection and under the assumption of a proton distribution which follows a power law in energy with index $\Gamma = 2.0$, the integral flux above 1 TeV can be calculated as:

$$F_\gamma(> 1 \text{ TeV}) \approx 2.3 \times 10^{-12} \text{ cm}^{-2} \text{ s}^{-1} \ . \tag{3.14}$$

Aharonian et al. (2005c) modelled the expected VHE γ-ray emission considering convection (but neglecting diffusion) and estimated the γ-ray flux from NGC 253 to $F_\gamma(> 1 \text{ TeV}) \approx 9.8 \times 10^{-13}$ cm^{-2} s^{-1}. Domingo-Santamaría & Torres (2005) have performed a full modelling, taking into account all energy-loss processes by CRs and obtained integral fluxes of $F_\gamma(> 1 \text{ TeV}) \approx 2.0 \times 10^{-13}$ cm^{-2} s^{-1}, which is an order of magnitude lower compared to the calorimetric limit. Fig. 3.6(a) and 3.6(b) show the results of the Domingo-Santamaría & Torres (2005) model. Also Rephaeli et al. (2010) recently performed a detailed modelling, taking into account convective and diffusive losses. The estimated fluxes are compared to the measurement performed with H.E.S.S. and the spectral results as obtained with the ζ analysis, which are presented in Chapter 6.

As outlined in this Chapter, VHE γ-ray emission is presumably expected from star forming environments since these are able to serve as particle acceleration sites and provide at the same time target material and/or radiation fields for the production of HE and VHE γ rays. In the following chapters, data from VHE γ-ray observations performed with H.E.S.S. of the CWB binary η Carinae, the young massive stellar cluster Westerlund 1 and the SB galaxy NGC 253 are analysed with the BDT method. Spectral and morphological results are presented and used to draw conclusions on the origin of the potential VHE γ-ray emission from these objects.

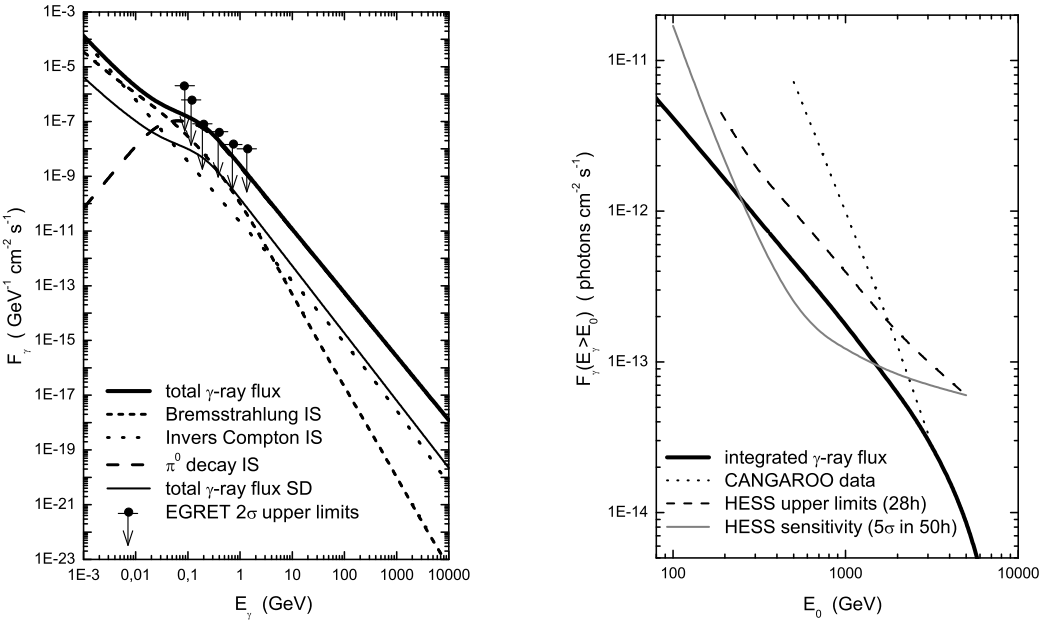

(a) (b)

Figure 3.6: Results of the simulated model as obtained by Domingo-Santamaría & Torres (2005). (a) Predicted differential γ-ray flux split by different contributions and between disc (SD) and SB nucleus (IS). Also indicated is the 2σ upper limit (UL) as obtained by EGRET. (b) Integral γ-ray flux in the region between 100 GeV and 10 TeV. Also shown are the CANGAROO results as well as the H.E.S.S. UL and the H.E.S.S. sensitivity (Figures taken from Domingo-Santamaría & Torres (2005)).

4 VHE γ-ray observations of η Carinae and the Carina region

4.1 The Carina region and the CWB η Carinae

The Carina Nebula is one of the largest and most active HII regions in our Galaxy and is a place of ongoing star formation. It is located in the constellation Carina, at a distance of ∼2.3 kpc harbouring eight massive stellar clusters with more than 64 O-type stars (Feinstein 1995; Smith 2006). A Hubble Space Telescope image of the Carina nebula showing the most prominent regions is displayed in Fig. 4.1. Based on the most evolved stars inside and the size of the nebula, its age is estimated to 3 Myrs. Diffuse X-ray emission was reported by Hamaguchi et al. (2007) based on observations from Suzaku, XMM-Newton and Chandra. The authors concluded that apart from two thermal, lower-temperature components originating from diffuse plasma, the 5 keV component is most likely generated by one or multiple SNRs. The Carina nebula also harbours four WR stars as well as the extreme-type luminous blue variable (LBV) η Carinae.

η Carinae is one of the most peculiar objects in our Galaxy. In the 1840's and 1890's a giant outburst (also known as the great eruption) and a smaller outburst produced the Homunculus- and Little Homunculus nebula (Ishibashi et al. 2003, see e.g.). η Carinae and the Homunculus nebula in optical and X-ray wavelengths is depicted in Fig. 4.2. The material expelled from the central star in the great eruption adds up to a mass of $\sim 12\ M_\odot$ which moves outwards at an average speed of ~ 650 km s^{-1} implying a kinetic energy of the giant outburst of roughly $(4-10)\times 10^{49}$ erg (Smith et al. 2003). Interestingly, Smith (2008) found material which is moving ahead of the expanding Homunculus nebula at speeds of $3500-6000$ km s^{-1}. The existence of this material basically doubles the estimate of the kinetic energy of the giant outburst and can be interpreted as a low-energy SNR shell (Smith 2008) with a fast blast wave moving into the ISM with velocities comparable to e.g. SN 1006 (Vink 2005).

For a long time it was believed that the central object, η Carinae, is a hypergiant LBV star, though recent observations (Hillier et al. 2001; Pittard & Corcoran 2002) suggest a binary system composed of a massive WR star ($M \geq 90 M_\odot$) and an O- or B-type star with a mass of $M \leq 30 M_\odot$. The optical (Damineli 1996; Damineli et al. 2000) and IR (Whitelock et al. 1994, 2004) light curves infer a long period of ∼2023 days (5.54 years) with a long time in a "high spectroscopic state" characterised by an emission line spectrum and a short time (typically a few months) in a "low spectroscopic state" – also called "spectroscopic events"[1]. An analysis of the X-ray light curves point to an highly eccentric orbit of $e \sim 0.9$ (Corcoran et al. 2001; Falceta-Gonçalves et al. 2005). In contrast to the WR star, which has a very high mass loss rate of $\dot{M}_1 \approx 2.5\times 10^{-4}\ M_\odot$ yr^{-1} and a

[1] This low spectroscopic state is believed to be caused by the collapse of the colliding wind region.

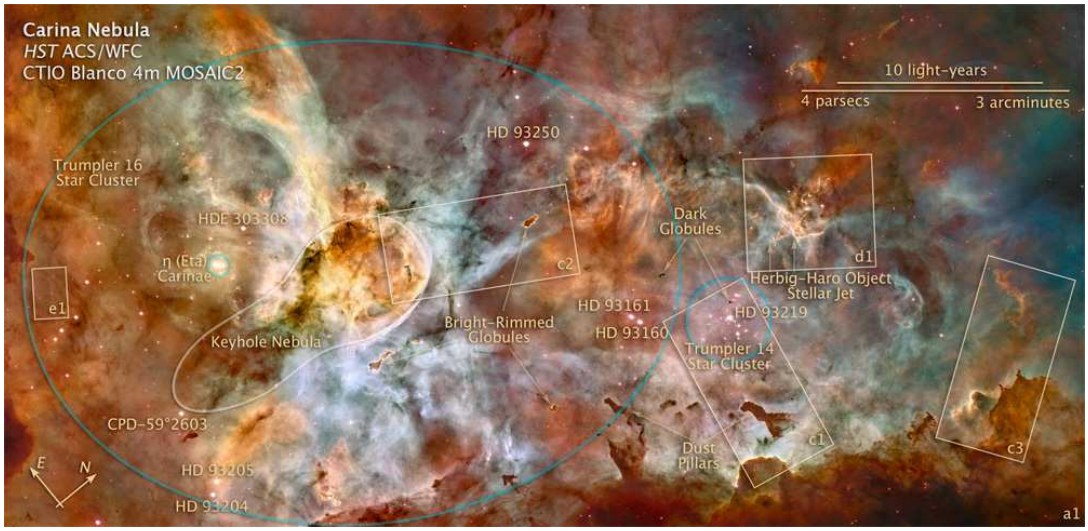

Figure 4.1: Optical image of the Carina nebula as seen by Hubble. The image also depicts prominent regions such as the stellar clusters Trumpler 14 and Trumpler 16, Herbig-Haro objects as well as two of the most massive stars known in the Milky Way: η Carinae and HD 93250. Credit: NASA/ESA.

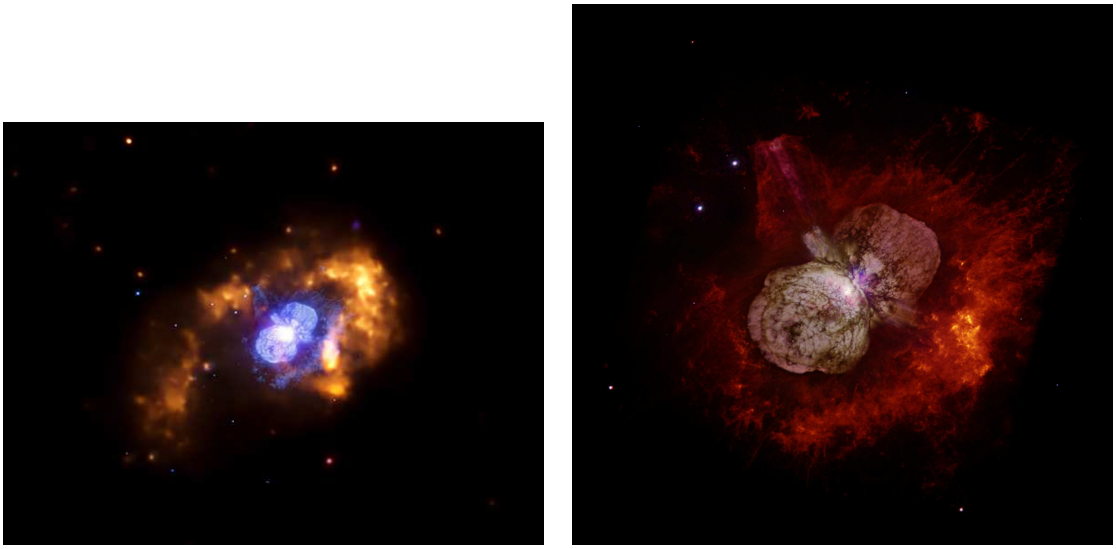

(a) (b)

Figure 4.2: (a) Composite Chandra/HST image. X-ray emission as measured with the Chandra satellite from η Carinae is shown as yellow ($0.5-1.2$ keV) and white ($1.2-11$ keV). The yellowish ring is interpreted as material blown away from the star in an eruption ~ 1000 yrs ago (Credit: NASA/CXC/GSFC/M.Corcoran et al). Blue depicts the emission as seen by Hubble. (b) Zoom into the central region of image (a); Optical emission as detected by the Hubble Space Telescope. The Homunculus nebula is clearly visible as double-lobe-like structure (Credit: NASA/ESA/STScI).

terminal wind velocity of $v_1 \approx (500-700)$ km s^{-1}, the companion star has a thin fast wind ($\dot{M}_2 \approx 1.0 \times 10^{-5}\ M_\odot$ yr^{-1} and $v_2 \approx 3000$ km s^{-1}) (Hillier et al. 2001; Pittard & Corcoran

2002). The total kinetic energy in stellar winds is of the order of a few 10^{37} ergs s^{-1} for the WR and the OB star together. When the supersonic expanding winds collide, they form a wind-wind interaction zone at the stagnation point with a reverse and forward shock where a few 10% of this kinetic energy could be transferred into the acceleration of particles to non-thermal energies (see also Section 3.1). With an acceleration efficiency of $\mathcal{O}(10\%)$ a yield of $10^{35} - 10^{36}$ ergs s^{-1} is in principle possible. This would translate into an energy flux of $\approx 10^{-6} - 10^{-7}$ ergs cm^{-2} s^{-1}

The existence of non-thermal particles in this CWB was first reported by the INTEGRAL collaboration. They obtain a luminosity of 7×10^{33} ergs s^{-1} in the hard X-ray band (22–100 keV)[2], representing only 0.1% of the total kinetic energy available in the wind-wind collision (Leyder et al. 2008). Just recently the AGILE collaboration reported on the detection of a variable source, 1AGL J1043–5936, coincident with the position of η Carinae (Tavani et al. 2009b) which is also seen (but as steady source) by the LAT instrument onboard the Fermi satellite (Abdo et al. 2009b, 2010). Section 4.3 will discuss the HE emission along with the VHE γ-ray results presented in the next section in more detail.

H.E.S.S.'s detection of HESS J1023–575 (Aharonian et al. 2007a) and the extended emission from the vicinity of Westerlund 1 (see Chapter 5 and Ohm et al. 2009a) seem to indicate that VHE γ-ray emission is linked to massive stars in our Galaxy and motivates an investigation of η Carinae and the Carina region as a whole as possible VHE γ-ray sources. Furthermore, acceleration of particles to very high energies in binary systems like LS 5039 (Aharonian et al. 2006f), PSR B1259–63 (Aharonian et al. 2005a) and presumably in HESS J0632+057 (Aharonian et al. 2007c; Skilton et al. 2009) was established by H.E.S.S. in previous detections and give a further motivation. However, the detection of a CWB in VHE γ rays is still pending.

4.2 VHE γ-ray data and data analysis

The Carina region and its surroundings were observed with the full four-telescope H.E.S.S. array for a total of 22 hours in 2004, 2006 and 2009. Data taken under unstable weather conditions or with malfunctioning hardware has been excluded in the standard data quality selection procedure (see Section 1.3.2). After standard data quality selection and dead time correction, the total live time amounts to 9 hours. Observations have been carried out at moderate zenith angles of 36° to 54°, with a mean value of 42°. The average pointing offset from η Carinae is 1.0°. The available data has been analysed with the ζ_{std} cuts to obtain energy spectra and light curves and with the ζ_{weak} cuts for the production of sky images. Thereby, a good γ/hadron separation as well as a low energy threshold of 0.52 TeV is achieved. Table 4.1 summarises the properties of the different data sets used in the analysis as well as the signal and background statistics.

Fig. 4.3(a) shows an image of the acceptance corrected VHE γ-ray counts per arcmin^2 of the $2° \times 2°$ f.o.v. centred on the optical position of η Carinae. The map has been smoothed with a Gaussian kernel of $3.4'$ width to reduce the effect of statistical fluctuations. Although

[2] Averaged over orbital periods $0.16 - 0.19$, $0.35 - 0.37$ and $0.99 - 1.01$, with a non-detection within 100ks at the RXTE minimum at periastron.

Data set	Period	θ^2 $^\circ$	live time hrs	N_{On}	$\alpha \cdot N_{Off}$	Excess	Significance σ
1	Mar 04	0.0125	1.4	59	54	5	0.6
2	May 06	0.0125	2.6	40	47	-7	-1.0
3	Feb 09	0.0125	0.9	12	11	1	0.1
all	Mar 04 – Feb 09	0.01	9.0	84	74	10	1.1
all	Mar 04 – Feb 09	0.16	9.0	1494	1274	220	5.9

Table 4.1: Properties of the data sets used for spectral analysis (1,2,3) consisting of only four-telescope data and the whole data set (all), also including three-telescope data. Number of γ-ray-like and background events as well as significance and γ-ray excess. ζ_{std} cuts were applied in the case of the split data sets together with the *Reflected* background method and ζ_{weak} cuts for the total data set and the *Template* background method (Rowell 2003).

no significant γ-ray emission at the position of η Carinae is detected, a small VHE γ-ray excess of extended nature seems to be apparent in the f.o.v.. This is also suggested by the one-dimensional distribution of VHE γ-ray excess events as a function of squared angular distance from η Carinae, which is shown in Fig. 4.3(b). Within an a priori chosen radius of 0.4°[3] around the η Carinae position, a total of 220 excess events at a significance level of 5.9σ are found, supporting the idea of an extended VHE γ-ray emission in this region. One of the main goals of the 35 hours of H.E.S.S. observations which are planned for 2010 on this target is to confirm this VHE γ-ray signal.

4.3 HE and VHE γ-ray results in context

At lower energies, the Fermi LAT detected a point-like steady HE γ-ray emitter within the first three months of operation (Abdo et al. 2009b) coincident with the η Carinae position. The one-year data confirmed the existence of this source, and reduced the positional error down to 1.8 arcmin (95%), which is consistent with the position of η Carinae. The Fermi source, 1FGL J1045.2–5942 showed no indication of variability[4], even though variability from a CWB could be expected. The spectrum of 1FGL J1045.2–5942 can not be described by a pure power law and shows significant curvature[5]. Fig. 4.4(a) shows the flux of the Fermi source in five energy bands together with the 2σ upper limit (UL) of 7×10^{-13} ph cm^{-2} s^{-1} on the flux above 0.52 TeV as derived from the H.E.S.S. measurement using all four-telescope data and an integration radius of 0.11°. Extrapolating the power-law fit results as given in the Fermi 1-year catalogue (Abdo et al. 2010) to the VHE domain would imply an integral flux $F_\gamma(> 0.52 \text{ TeV}) \simeq 2 \times 10^{-11}$ ph cm^{-2} s^{-1}, an order of magnitude above the H.E.S.S. UL which is shown in Fig. 4.4. The spectral curvature found by

[3] This radius was chosen a priori to match the integration radius typically used in the GPS analysis for the search of very extended sources.

[4] The variability index 12.9 has to be compared to the reference value of 23.21, which indicates a 1% probability of being a steady source.

[5] The curvature index 26.3 has to be compared to the reference value of 11.34, which indicates a 1% probability that the power-law spectrum is a good fit to the data.

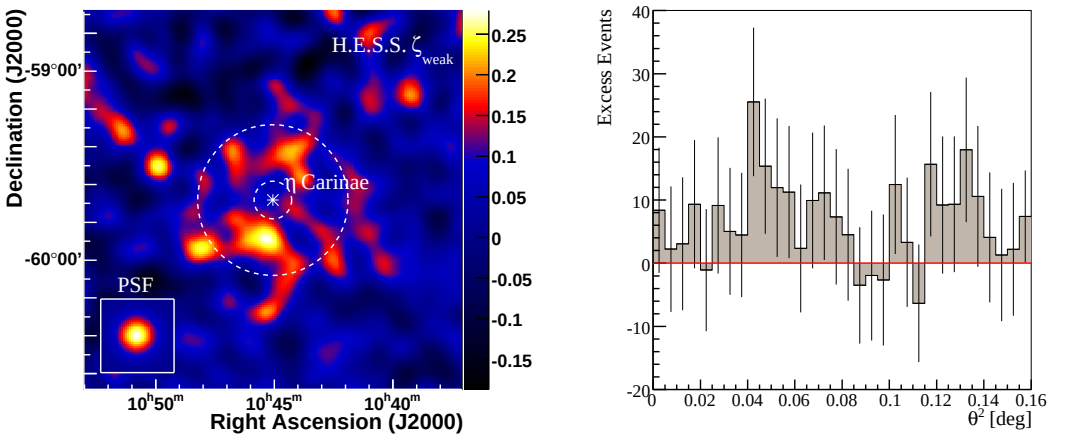

(a) (b)

Figure 4.3: (a) Acceptance corrected H.E.S.S. map in units of VHE γ-ray events per arcmin^2 of the region $2^\circ \times 2^\circ$ around η Carinae. The image was smoothed with a Gaussian kernel of $3.4'$ width to reduce the effect of statistical fluctuations. Circles denote the integration radii which were used to extract the statistics as given in Table 4.1. The inlay in the lower left corner represents the size of a point-like source as it would have been seen by H.E.S.S. for this analysis (b) θ^2 distribution of VHE γ-ray excess events relative to the η Carinae position.

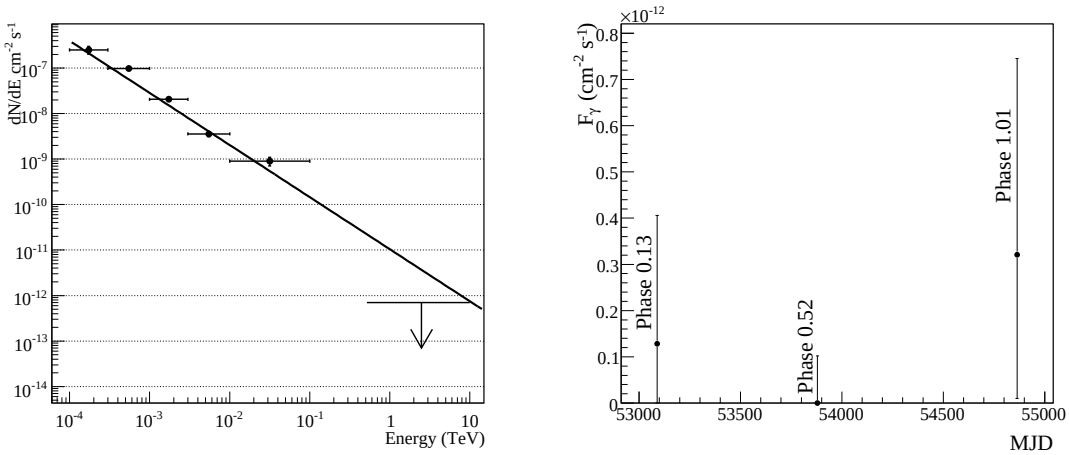

(a) (b)

Figure 4.4: (a) Spectral energy distribution of the Fermi source 1FGL J1045.2–5942 along with the H.E.S.S. 2σ upper limit on the γ-ray flux above an energy of 0.52 TeV. (b) Monthly light curve of VHE γ-ray emission from η Carinae between 1 and 10 TeV. 2σ statistical errors are indicated.

Fermi together with the H.E.S.S. UL demonstrates that deeper observations in the VHE regime can help to further investigate the spectral curvature, the implied energetics and the highest particle energies reached in this source.

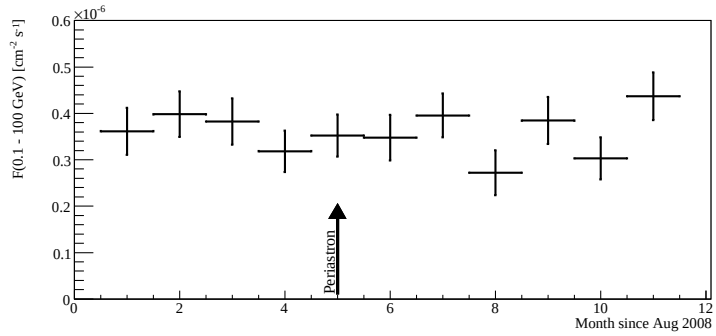

(a)

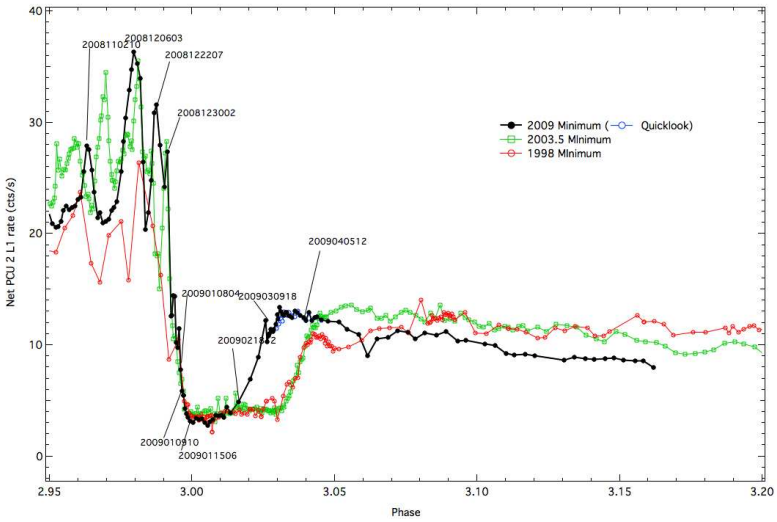

(b)

Figure 4.5: (a) Monthly light curve of 1FGL J1045.2–5942 for events with energies $(0.1 \leq E \leq 100)$ GeV as provided by the Fermi 1-year catalogue (Abdo et al. 2010). (b) RXTE light curve of η Carinae over a 13-year period in the $2 - 10$ keV band (Figure taken from Corcoran 2010).

The AGILE collaboration reported on a 5 – 10 times higher flux in October 2008 (orbital phase: 0.95) compared to the average flux of this γ-ray source. However, a preliminary analysis of the Fermi data could not confirm this increased flux level (Takahashi et al. 2009). Especially the LAT weekly light curve for events with energies $E > 0.1$ GeV depicted in Fig. 4.5(a) shows no decline in flux during the periastron passage mid-January 2009. A large drop in flux during this time is suggested by the X-ray light curve as measured with RXTE (depicted in Fig. 4.5(b)). The light curve shows a factor of ~ 30 smaller flux in the $2 - 10$ keV band during periastron compared to the maximum flux level which is reached shortly before (Moffat & Corcoran 2009).

The H.E.S.S. observations basically covered a full orbital period of η Carinae and can therefore provide information on a possible variability on larger timescales. Fig. 4.4(b) shows the monthly light curve of the H.E.S.S. measurements between (1 – 10) TeV for three different orbital phases (0.13, 0.52, 1.01). Unfortunately, the orbital phase of the AGILE flare is not covered by H.E.S.S. observations. The H.E.S.S. data shows no significant flux

in the three months of observations within the 5 years of observations. Variability on shorter timescales or at lower flux levels is in principle possible.

4.4 Discussion and outlook

Although the amount of collected H.E.S.S. data in the Carina region is quite limited, interesting preliminary results and future prospects arise. The hint of extended VHE γ-ray emission from the vicinity of η Carinae seen in the H.E.S.S. data seems to indicate that particle acceleration to very high energies occurs in this prominent star forming region. A detailed spectral and morphological study of the data collected in the forthcoming H.E.S.S. observations will help to understand the origin of the VHE γ-ray emission and shed light on particle acceleration processes in this environment.

The detection of a strong point-like source coincident with the η Carinae position by Fermi and AGILE seems to suggest that acceleration of particles to non-thermal energies is occurring in a CWB system. The spectrum as measured with Fermi extents to ~ 100 GeV and shows significant curvature. If one extrapolates the highest energy Fermi flux points to the VHE regime and also considers the suggested spectral curvature, the H.E.S.S. flux UL is close to the expected value and the planned H.E.S.S. observations of the Carina region in 2010 either result in a detection of η Carinae in the VHE range and shed light on the maximum particle energies reachable in this source, or would imply a break or cut-off in the spectrum between the Fermi energy range and the energy range, covered by H.E.S.S..

If the emission seen by Fermi and AGILE indeed originates exclusively from the CWB, the detection of HE γ-ray emission during periastron passage is puzzling. Since it is believed that the spectroscopic events are caused by a collapse of the colliding wind region, no particle acceleration should occur during this low-state. Alternatively, one could think of the HE γ rays emitted either by a pulsar, a PWN or a background AGN. Since the spectrum of the source shows no cut-off at a few GeV, as typical for the large population of γ-ray pulsars seen by the LAT, and no periodicity in the HE γ-ray emission in a pulsar blind search has been found (Abdo et al. 2009a), an association with a γ-ray pulsar is unlikely. Moreover, the existence of a PWN is doubtful, given the point-like nature of the emission and the fact, that no such object was discovered in deep X-ray observations with the Chandra, XMM-Newton and Suzaku satellite. An extragalactic background object, such as an AGN, is a possible counterpart as well. However, just one extragalactic object[6], which is not associated to an AGN, lies within $1.8'$ of the η Carinae position and has no reported high flux state in any wavelength band reported in the literature.

If neither the CWB nor the other three source types are responsible for the observed HE γ rays – especially during periastron passage – an alternative model is required to explain the emission. In the following, such a model is developed and presented for the first time, namely, the acceleration of particles in the fast expanding blast wave of the 1843's giant outburst, which shows the behaviour of a very young, low-energy SNR shell.

Smith (2008) finds that the kinetic energy stored in the fast expanding material is $E_{\rm kin} \approx$

[6] This object is an unclassified X-ray source – EXMS B1043–593, found by EXOSAT (Reynolds et al. 1999).

7×10^{49} erg, roughly the same as stored in the whole Homunculus nebula. Since the blast wave mimics a SNR shell, the expected γ-ray luminosity is estimated following Aharonian (2004). A scaling parameter relation is used to determine the flux of γ rays, which is produced in *pp* interactions of an expanding SNR shell and the ambient medium. This is applied to the fast outflow ejected from η Carinae in 1843. For a standard power law with exponential cut-off in accelerated protons, the scaling parameter A is given as:

$$A = \left(\frac{W_{CR}}{10^{50}\ \mathrm{erg}}\right)\left(\frac{d}{1\ \mathrm{kpc}}\right)^{-2}\left(\frac{n}{1\ \mathrm{cm}^{-3}}\right)\ . \tag{4.1}$$

Assuming an average ambient density of 500 cm^{-3} (Smith 2008), a distance to η Carinae of 2.3 kpc and furthermore that 10% of the total kinetic energy E_{kin} is transferred into the acceleration of protons W_{CR}, the scaling factor is $A \approx 6.6$. This scaling parameter can then be used to derive the integral γ-ray flux above 300 MeV according to Aharonian (2004) as:

$$F_\gamma(\geq 300\ \mathrm{MeV}) \approx 3 \times 10^8 A\ \mathrm{cm}^{-2}\ \mathrm{s}^{-1} = 2 \times 10^{-7}\ \mathrm{cm}^{-2}\ \mathrm{s}^{-1}\ . \tag{4.2}$$

The average integral flux in HE γ rays as measured by Fermi is 1.2×10^{-7} cm^{-2} s^{-1} for energies (0.3 – 100) GeV. This means that from energetics considerations the estimated γ-ray luminosity is of the same order of magnitude as the measured γ-ray flux in the HE domain.

The maximum particle energy which can be attained in the DSA is according to Lagage & Cesarsky (1983):

$$E_{\mathrm{max}} \sim \left(\frac{46Z}{\kappa}\right)\left(\frac{v_{cl}}{100\ \mathrm{km\ s}^{-1}}\right)\left(\frac{B}{1\ \mu G}\right)\left(\frac{R}{1\ \mathrm{pc}}\right)\ \mathrm{GeV}\ , \tag{4.3}$$

where Z is the charge of the particle, κ the gyro-factor (~ 1), R the linear size of the acceleration region and B the magnetic field. The projected angular size of the acceleration region of $\approx 40 - 70''$ translates into a physical size of ≈ 0.5 pc (Seward et al. 2001). Assuming a magnetic field of 1 μG, the maximum energy of a proton or electron E_{max} is between $0.8 - 1.4$ TeV, depending on the blast wave speed of 3500 and 6000 km/s, respectively. These energies are consistent with the maximum γ-ray energies around $\approx$ 100 GeV found by Fermi.

One possibility to prove the existence of HE electrons would be the detection of synchrotron radiation in the fast expanding blast wave. A population of electrons which produce IC photons with peak energy E_γ emit synchrotron UV/X-rays in a magnetic field B with peak energy E_X (Aharonian 2004):

$$E_X \simeq 5 \cdot \left(\frac{E_\gamma}{1\ \mathrm{TeV}}\right)\left(\frac{B}{10\ \mu G}\right)\ \mathrm{keV}\ . \tag{4.4}$$

With a magnetic field of 1 μG, the peak of synchrotron emitting electrons responsible for the IC photons of 1 TeV is in the soft X-ray domain around 1 keV. The Chandra satellite detected soft X-ray emission from a ring-like structure surrounding η Carinae known as the *outer ejecta*. The measured X-ray spectrum is of thermal nature with a characteristic plasma temperature of $\sim 0.6 - 0.8$ keV (Weis et al. 2004). That implies that shock waves

have already heated up the outer ejecta to keV temperatures. However, it is presumably hard to identify a non-thermal synchrotron component in the thermal X-ray spectrum.

Another possibility to prove the existence of HE electrons is to perform high resolution radio observations. Resolving a possible shell-like structure coincident with the blast wave or detecting a non-thermal radio spectrum in these observations would further support the proposed scenario.

If the developed model proves to be real, this will be a perfect opportunity to study 'real-time' CR acceleration and propagation in one of the best studied astrophysical environments. Furthermore, η Carinae is located in the solar neighbourhood a factor 20 closer to Earth compared to the prominent SN in the Large Magellanic Cloud SN 1987A which has an age of 23 years. Also the recently found youngest Galactic supernova remnant SN G1.9+0.3 (Reynolds et al. 2008), located near the Galactic Centre with an age of ~ 100 years is a factor 3.5 further away. η Carinae would also be a new source type in the MeV – GeV (and presumably TeV) domain, a young, low-energy SNR shell originating from an LBV outburst.

5 VHE γ rays from the vicinity of the young massive stellar cluster Westerlund 1

5.1 The young massive stellar cluster Westerlund 1

The compact young open stellar cluster Westerlund 1 (Wd 1) is the most massive stellar cluster known in our Galaxy with a mass likely in excess of 10^5 $M_\odot$ (Clark et al. 2005). Presumably, Wd 1 is more massive than any other young stellar cluster in the Local Group. With such a high mass it is associated to the class of Starburst clusters (also referred to as super star clusters), which are usually found in the central regions of SB galaxies and are characterised by large electron densities ($10^3 - 10^6$ cm^{-3}) and high global pressures ($P/k_B > 10^7 - 10^{10}$ K cm^{-3}) (Johnson 2004). Wd 1 is located at a distance of $(4-5)$ kpc at the outer edge of the Galactic bar (Brandner et al. 2005; Crowther et al. 2006; Kothes & Dougherty 2007). It has an estimated age of 5×10^6 yrs and a total stellar luminosity which is reaching $L_* \approx 10^7$ $L_\odot$ (Crowther et al. 2006). With a core size of $25''$ (Clark et al. 2005; Muno et al. 2006a) Wd 1 is a very compact cluster harbouring a large population of stars in advanced stages of stellar evolution like super- and hyper-giants as well as one LBV star (Westerlund 1987; Clark & Negueruela 2002, 2004; Clark et al. 2005; Negueruela & Clark 2005). It is currently the record holder in terms of its rich population of stars in the WR phase. Until now 24 WR stars are known of which at least 70 % are bound in binary systems (Crowther et al. 2006). The kinetic energy stored in the fast ($v \approx 10^3$ km s^{-1}) and dense ($\dot{M} \approx 1.0 \times 10^{-5} M_\odot$ yr^{-1}) winds of the WR stars in Westerlund 1 amounts to $L_{\rm W} \approx 10^{39}$ ergs s^{-1}. Also several SN explosions are expected to have occurred in Wd 1. Extrapolating the initial mass function (IMF) for stars $M > 30$ $M_\odot$, Muno et al. (2006b) conclude that $80-150$ stars with initial masses $M > 50$ $M_\odot$ must have undergone SN explosions. Assuming a kinetic energy release of 10^{51} ergs per SN, an additional contribution of $(2-5) \times 10^{39}$ ergs s^{-1} is in principle available in this system for particle acceleration (Muno et al. 2006b). The fact that so far no SNR shells have been detected at radio or X-ray wavelengths can be understood in the framework of the expansion of SNRs in a hot medium with a high pressure where radiative cooling is negligible (see e.g. Section 3.2). A $4' \times 4'$ sky region, centred on Wd 1, in optical wavelengths is depicted in Fig. 5.1(a).

Using X-ray observations with the Chandra satellite, Muno et al. (2006a) found a Magnetar candidate ($P = 10.6$ s) whose progenitor star is associated to Wd 1 and was as massive as 40 $M_\odot$. A sophisticated analysis of the Chandra data also revealed extended, arc-minute-scale, non-thermal X-ray emission (Muno et al. 2006b). This kind of emission is seen just for a couple of young stellar associations in our Galaxy like e.g. RCW 38 (Wolk et al. 2002) and possibly the Arches cluster (Law & Yusef-Zadeh 2004) as well as in the Large Magellanic Cloud (LMC) in 30 Dor C (Bamba et al. 2004) and DEM L192 (Cooper et al. 2004). The extended, non-thermal X-ray emission along with the numerous point-

(a) (b)

Figure 5.1: (a) Optical image of the $4' \times 4'$ f.o.v. of the stellar cluster Westerlund 1 (Image taken from Brandner et al. (2008)). (b) Westerlund 1 as seen by Chandra in X-ray wavelengths ($5' \times 4.5'$). Apart from numerous point-like sources, a diffuse non-thermal X-ray component is apparent (Credit: NASA/CXC/UCLA/M.Muno et al.).

like sources as detected by Chandra are shown in Fig. 5.1(b). The total X-ray luminosity observed in and around Wd 1 amounts to $L_X = 3 \times 10^{34}$ ergs s^{-1}, which represents just a fraction of 10^{-5} of the total mechanical energy in this system (Muno et al. 2006b). The same authors discuss various possibilities to explain the missing energy in this powerful system, among dissipation at other wavelengths and beyond the Chandra f.o.v., also CR acceleration has been suggested as possible channel to account for parts of the missing energy.

In this chapter, observational data taken with H.E.S.S. are presented and analysed (Section 5.2). Since the detected VHE γ-ray emission from the vicinity of Wd 1 is of very extended nature, in-depth systematic tests have been performed and are discussed in Section 5.3. Morphological and spectral studies are presented in Section 5.4 and 5.5, respectively. An extensive search for astronomical objects potentially associated to the VHE γ-ray emission is presented in Section 5.6 and possible acceleration and emission scenarios, including particle acceleration in Wd 1 are discussed in Section 5.7.

5.2 VHE γ-ray data and data analysis

5.2.1 Data set

The region around Wd 1 was observed during the GPS in 2004 and 2007 (Aharonian et al. 2006e). Additionally, pointed observations at low zenith angles have been performed from May to August 2008 to establish the hint of extended VHE γ-ray emission seen in

the survey data. Data taken under unstable weather conditions or with malfunctioning hardware has been excluded in the standard data quality selection procedure (Aharonian et al. 2006a). Also pointed observations on Wd 1 at very large zenith angles of $> 55°$ have not been considered to preclude potential systematic effects in the description of the camera acceptance at such low altitudes with an extended source like HESS J1646.8–455. After standard data quality selection and dead time correction, the total live time amounts to 33.8 hours. Observations have been carried out at zenith angles of 21° to 45°, with a mean value of 26°. The average pointing offset from the Westerlund 1 position is 1.1°.

5.2.2 Analysis technique

The data set presented in the following has been processed using the H.E.S.S. Standard Analysis for shower reconstruction (Aharonian et al. 2006a) and the BDT method for γ/hadron separation (see Chapter 2 and Ohm et al. 2009b). For two-dimensional sky image generation and morphology studies, the *Template* background model has been applied (Rowell 2003; Berge et al. 2007). The *Template* background method estimates the CR background in parameter space rather than in angular space. For this analysis, the BDT output parameter has been used to define signal and background regions for the *Template* background model. Since the system acceptance drops off radially with the distance to the telescope pointing position and since it is different for γ-ray and CR-like events, a correction has to be applied to α. All morphological results have been checked for consistency with the *Ring* background method and are discussed in detail in Section 5.3.

5.2.3 Analysis results

Fig. 5.2 shows an image of the acceptance corrected VHE γ-ray counts per arcmin^2 of the $3° \times 3°$ f.o.v. centred on the best fit position of the γ-ray excess. The map has been smoothed with a Gaussian kernel of $7.6'$ width to reduce the effect of statistical fluctuations and to make significant morphological features apparent. Significance contours at the $5-8\sigma$ level are overlaid after integrating events within a radius of 0.22° at each trial source position. This integration radius was matched to the RMS of the Gaussian and resembles significant features in the sky image[1]. Apparently, the VHE γ-ray emission is of extended and complex nature. In order to get an estimate of the centre of gravity of the emission, a two-dimensional Gaussian convolved with the H.E.S.S. PSF was fitted to the raw excess count map. The resulting best fit position is $16^{\mathrm{h}}46^{\mathrm{m}}50.40^{\mathrm{s}} \pm 30^{\mathrm{s}}$, $-45°49'12.0'' \pm 6'$, J2000 coordinates. Beyond the two-dimensional Gaussian fit, different hypotheses like a homogeneously emitting sphere and a thick shell have been tested and found to give consistent positions.

Based on the radial profile shown in Fig. 5.3[2], the 95% containment radius of the VHE γ-ray emission relative to the best fit position was determined to 1.1°. This radius has been used to produce the azimuthal profile shown in Fig. 5.9 and to extract the energy spectrum. Within the integration region of 1.1° a total of 2797 ± 134 γ-ray excess events

[1] This radius was chosen a priori to match the integration radius typically used in the GPS analysis for the search of slightly extended sources.

[2] The γ-ray emission from HESS J1640–465 has been excluded for radii $1.0° \leq r \leq 1.4°$.

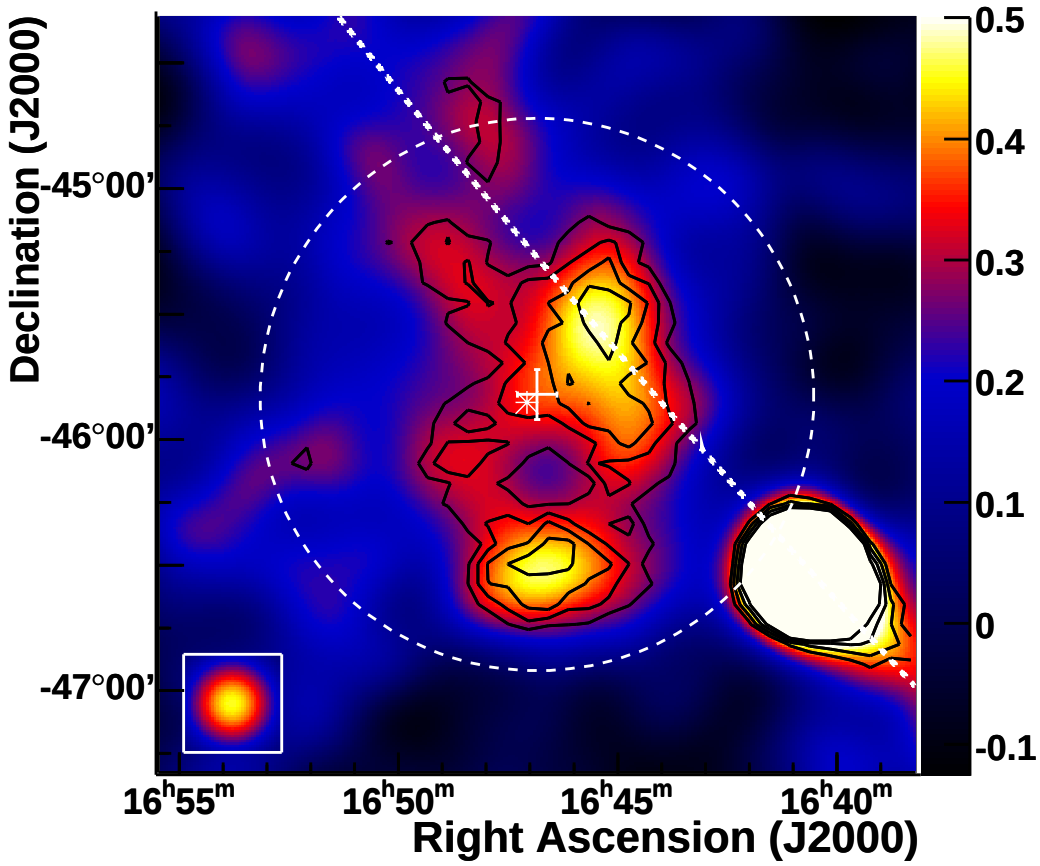

Figure 5.2: Acceptance corrected H.E.S.S. map in units of VHE γ-ray events per arcmin^2 of the region around Westerlund 1. The image was smoothed with a Gaussian kernel of 7.6′ width, significance contours of $5-8\sigma$ are overlaid in black. The white star marks the position of Westerlund 1 and the white cross the 68% error on the best fit position to the VHE γ-ray emission. The inlay represents the size of a point-like source as it would have been seen by H.E.S.S. for this analysis. The dotted white circle denotes the size of the region used for spectral reconstruction. The bright region in the lower right corner is the source HESS J1640–465 detected, during the Galactic plane scan (Aharonian et al. 2006e).

at a significance level of 22.1σ are found. To further illustrate how the γ-ray excess is distributed over the f.o.v., Fig. 5.4 depicts the statistics of γ-ray excess events along with the corresponding statistical errors for large bins of 0.3° width. The impression of distinct emission regions which are separated from each other is not very conclusive from Fig. 5.4 and is going to be quantitatively investigated in Section 5.4.

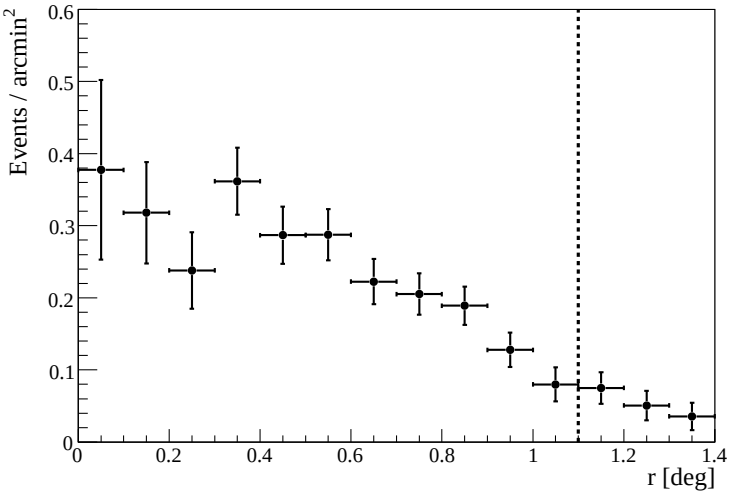

Figure 5.3: H.E.S.S. radial profile relative to the best fit position of the VHE γ-ray emission. The dotted vertical line denotes the region used to extract the spectrum shown in Fig. 5.12. Note that the region covering the bright source HESS J1640–465 has been excluded for the radial profile.

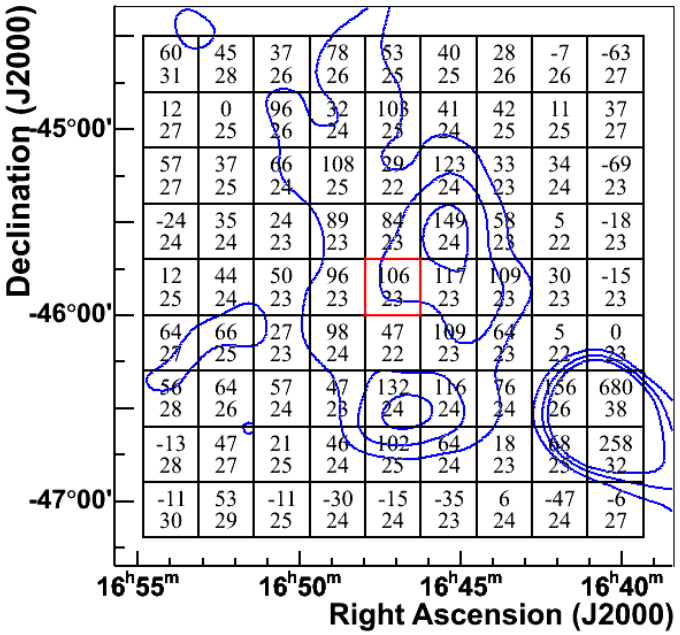

Figure 5.4: Uncorrelated VHE γ-ray excess map in bins of 0.3° width. The upper number in each bin is the excess coming from the quadratic region, the lower number is the corresponding statistical error in this bin. Blue contours correspond to a smoothed VHE γ-ray excess of 0.25, 0.35 and 0.45 events per arcmin^2. The red bin is centred on the position of Wd 1.

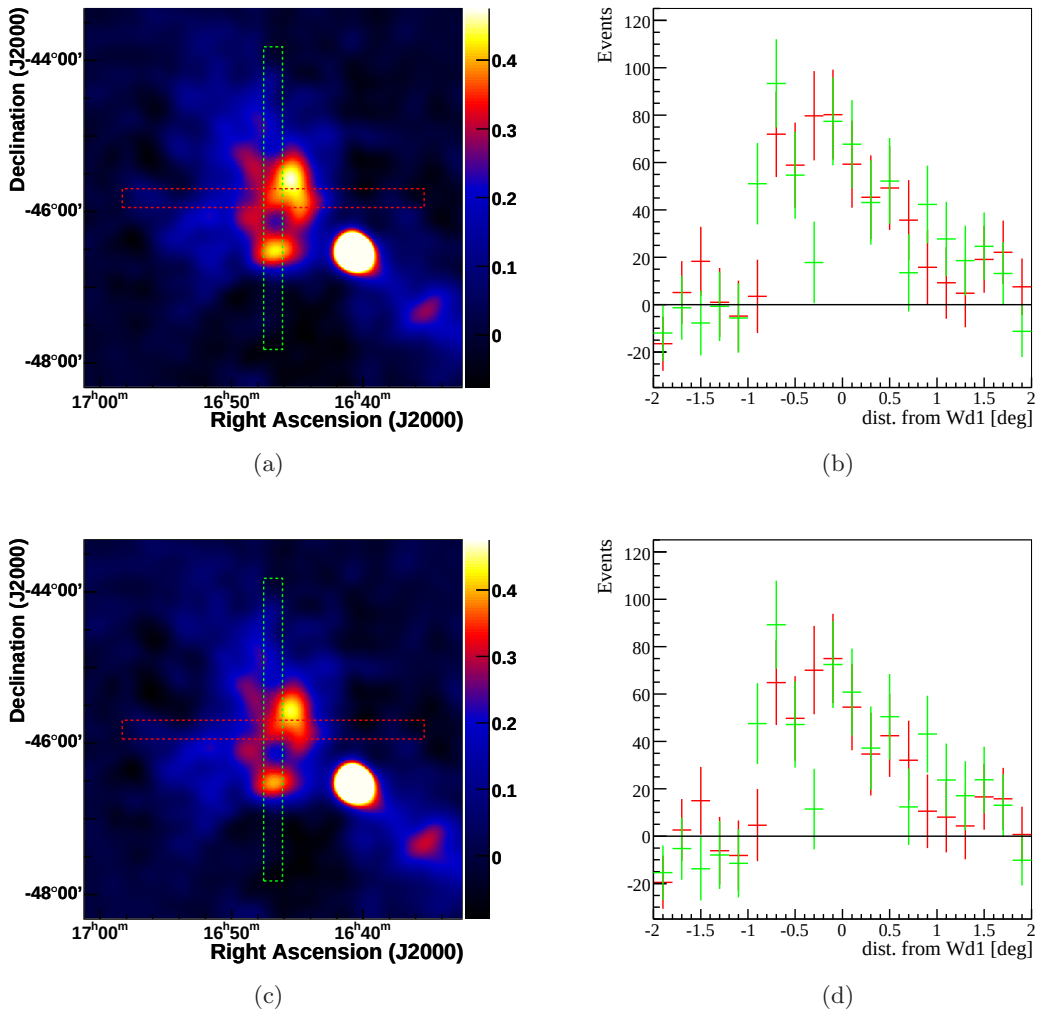

Figure 5.5: (a,c) H.E.S.S. sky image as shown in Fig. 5.2 but for a larger f.o.v. of $5^\circ \times 5^\circ$ as obtained with the *Template* background method (a) and with the *Ring* background model (c). Red and green boxes denote the regions used to extract the one-dimensional slices shown in (b) and (d). (b,d) One-dimensional slices of the uncorrelated excess map for the *Template* (b) and *Ring* (d). Red depicts the slice along RA, starting at larger values, green the slice along Dec, starting at smaller values.

5.3 Systematic tests

This section will focus on an investigation of the influence of potential systematic problems in the background estimation on the measured VHE γ-ray excess and can be skipped if it is not of particular interest for the reader.

The tests concern the morphology as well as the absolute level of the γ-ray emission. For this purpose, results as obtained with the *Template* background method have been checked for consistency with the *Ring* background model (see Section 2.4.1 for a description of the

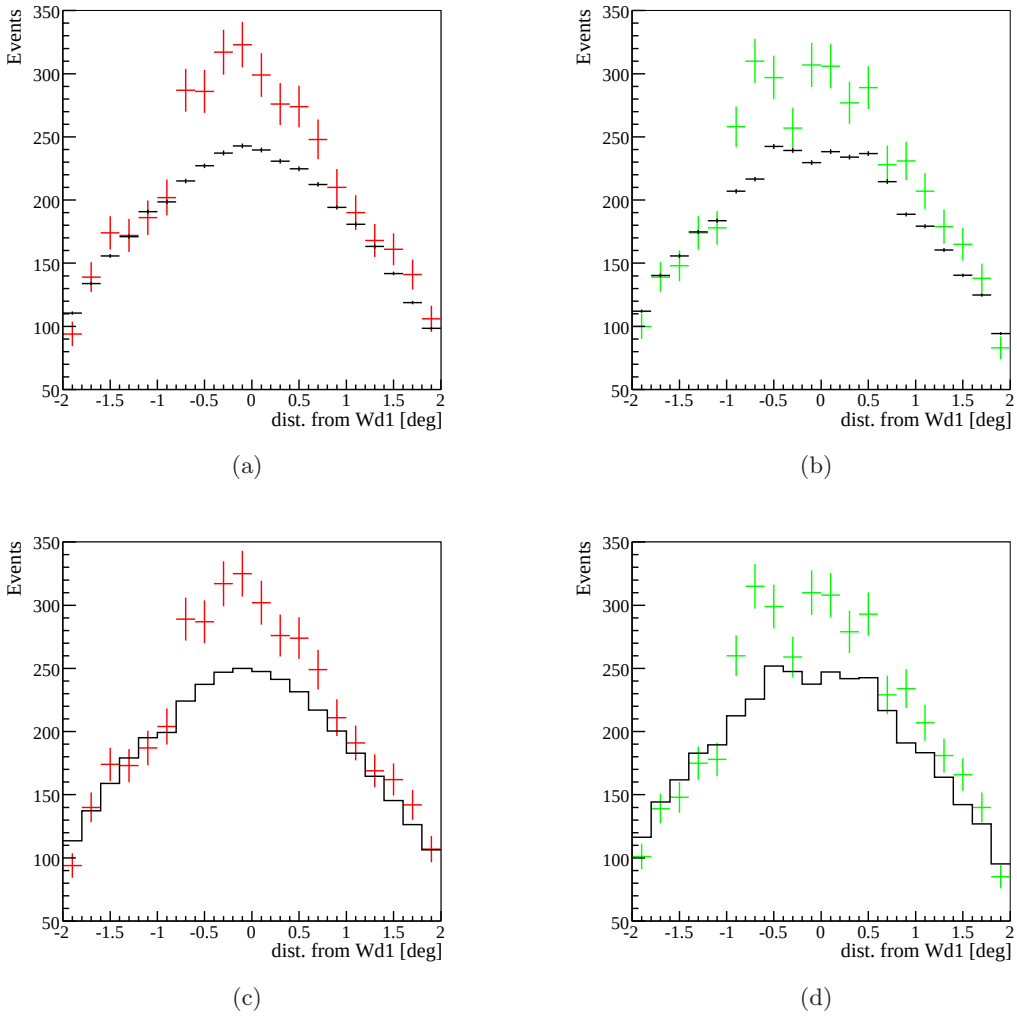

Figure 5.6: Slices along RA (a,c) and Dec (b,d) for the regions depicted in Fig. 5.5 for the *Template* (a,b) and *Ring* (c,d) background method. Signal distributions are shown in red/green, the α-scaled background distribution in black.

method). First of all, one-dimensional excess distributions in slices along RA and Dec of 4° length and 0.25° width, centred on the best fit position of the uncorrelated excess map have been produced. Fig. 5.5(a) illustrates the two regions and Fig. 5.5(b) shows the one dimensional distribution of excess events along RA and Dec for the *Template* model. Both distributions drop off to 0 excess outside the emission region as one would expect for a correct background estimation. In Fig. 5.5(c) and 5.5(d) the corresponding sky image and one-dimensional distributions are shown as obtained with the *Ring* background method. Although, some discrepancy in the absolute level of emission is apparent, the overall morphology agrees rather good between both background estimation methods.

This is further supported by the one-dimensional slices of signal and background maps shown in Fig. 5.6. The one-dimensional slices of the uncorrelated signal map and the α-scaled background map along RA and Dec are depicted in Fig. 5.6(a) and 5.6(b) for the

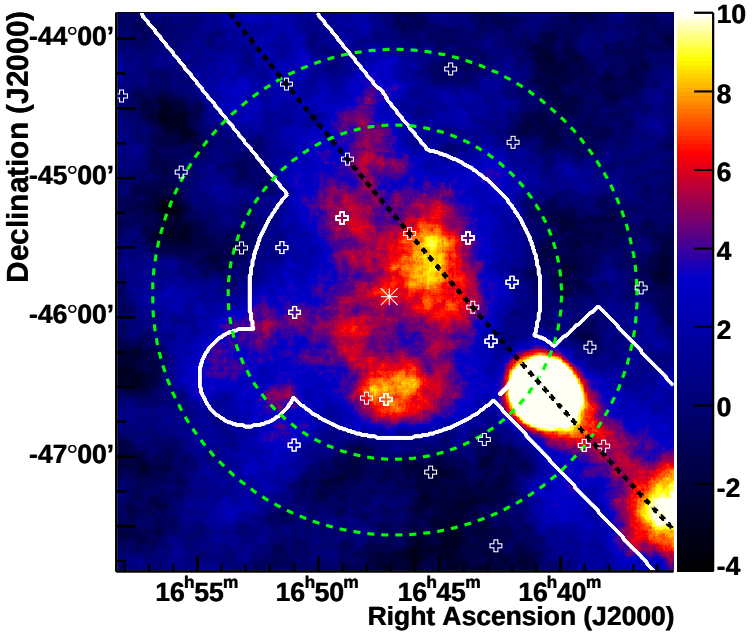

Figure 5.7: Significance map as obtained with the *Ring* background method. White crosses denote the different observation positions, the white star the Westerlund 1 position and the green circle the region used to extract the statistics given in Table 5.1. The white lines mark regions which have a significant γ-ray signal and are hence not used in the background estimation.

Template model, respectively. Fig. 5.6(c) and 5.6(d) show the same distributions for the *Ring* background method. Note that the normalisation of the signal and background map in both background estimation methods is calculated from the number of events in the f.o.v., excluding potential γ-ray source regions. So, by definition, signal and background events should follow the same distribution outside the signal region. The RA signal slices are compatible with the background slice outside the assumed signal region at distances $|\text{dist.}| \gtrsim 1.1°$ for both methods. However, there seems to be a γ-ray excess in the Dec slices apparent, which extents up to 1.5° away from the Westerlund 1 position. A diffuse VHE γ-ray component was also visible in the radial profile shown in Fig. 5.3. A potential effect of this diffuse emission on the background estimation is investigated in more detail in the following.

Fig. 5.7 depicts the significance map as obtained with the *Ring* background model. Also shown are the different observation positions, which to a large extent lie in regions with a significant γ-ray signal. Indicated in green is the ring, used to extract the γ-ray statistics as given in Table 5.1. The difference seen in absolute level of γ-ray emission which is suggestive from Fig 5.5(b) is also seen in the statistics. The difference between Ring and Template results is $\approx 20\%$ and could be caused by a potential γ-ray contamination in the ring which is used to estimate the background for the *Ring* model. Diffuse γ-ray emission which is not excluded in the analysis would affect the significance distribution in the sky image. If all γ-ray sources are excluded and the background estimation works as expected,

Region	On	Off	α	Excess	Significance σ	Rate Excess / αOff
Template	17597	995760	0.015	2797 ± 134	22.1	0.189 ± 0.010
Ring	17682	11259	1.36	2316 ± 197	11.7	0.151 ± 0.013
Reflected	2043	1862	0.96	258 ± 61	4.2	0.145 ± 0.034

Table 5.1: Statistics for the entire source region as obtained with different background estimation methods. Note that for the *Reflected* background and *On-Off* method the live time is just 4.5 and 20.5 hours, respectively.

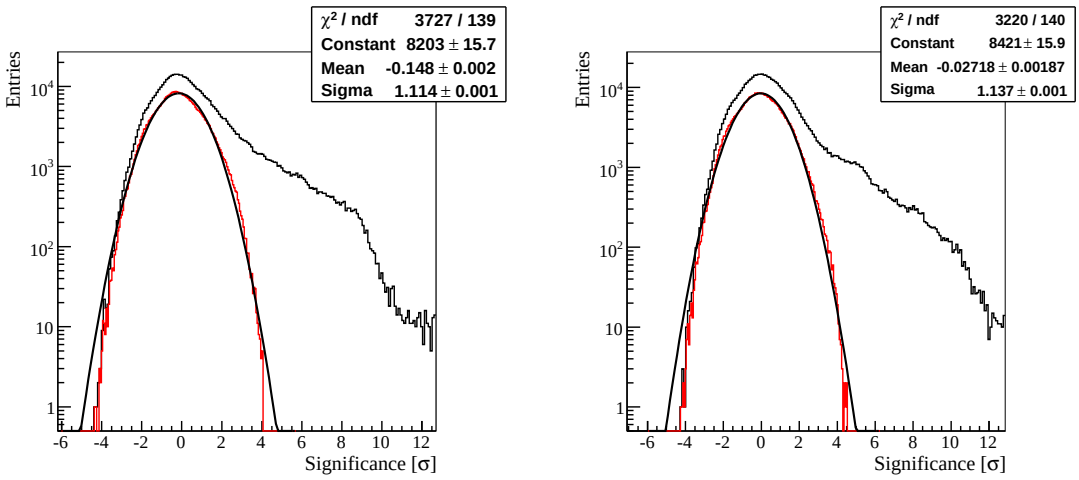

(a) (b)

Figure 5.8: Significance distributions of the Wd 1 f.o.v. for the *Template* (a) and *Ring* background method (b). The black curve depicts the distribution, including signal regions, the red curve was produced, excluding potential signal regions as indicated in Fig 5.7.

the distributions should be centred at 0 with a width of 1. Fig. 5.8(a) and 5.8(b) depict the significance distributions over the f.o.v. for the *Template* and *Ring* background model. Also shown are the distributions without taking into account the signal regions as indicated in Fig. 5.7. For both methods, the width of the 'excluded significance' distribution is with 1.11 slightly larger than 1. Hence, this could be indicative for a potential diffuse γ-ray component in this region of the sky, which has not been excluded in the analysis[3]. On the other hand, since both, *Ring* as well as *Template* background method, rely on a model of the acceptance curve, a systematic difference between assumed model and true model could also cause the observed effect. As noted by Berge et al. (2007), such a difference could introduce additional systematic effects for the *Template* model, since for this method two different system acceptance curves are used in the background estimation.

However, as shown at the beginning of this section, *Template* and *Ring* method reveal the same morphological features and agree on the overall shape of the γ-ray emission. So, the

[3] Note that this would also affect the background estimation for the *Reflected* model since background control regions are chosen from the same f.o.v..

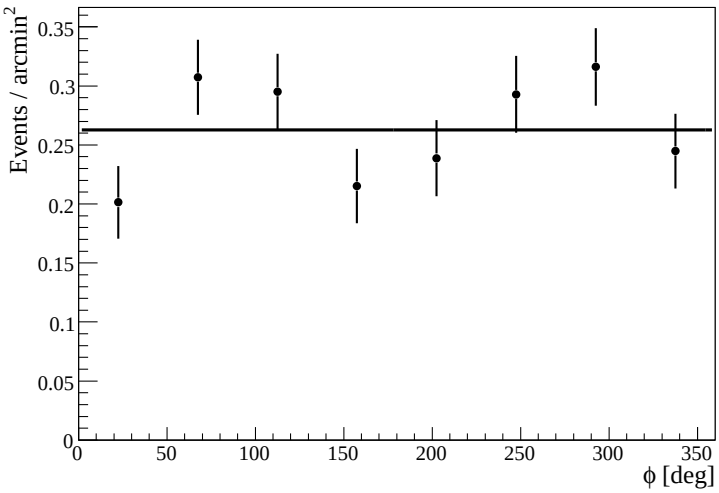

Figure 5.9: H.E.S.S. azimuthal profile integrated over the 1.1° integration region relative to the best fit position. 0° denotes north and 90° east in this representation. The fit of a constant which is shown as black solid line yields a mean value of 0.26 ± 0.01 events/arcmin^2 and has a χ^2/ndf of 15.2/7 (3.5% probability). The fit of a constant to the azimuthal profile as obtained with the *Ring* method reveals a mean value of 0.24 ± 0.01.

morphological studies performed with the *Template* method and presented in the following are qualitatively not affected by the difference in absolute γ-ray emission as discussed in this section.

5.4 Morphological analysis

As a first attempt to quantify the complicated morphological structure suggestive from the sky image shown in Fig. 5.2, the number of VHE γ-ray excess events together with their associated statistical errors in coarse quadratic bins of 0.3° width is shown in Fig. 5.4. Apparently, on the basis of the available statistics it is hard to draw a strong conclusion on the possibility of multiple emission regions within the Wd 1 f.o.v.. The sky image also suggests a lack of γ-ray emission east to Wd 1. However, the azimuthal profile in Fig. 5.9 does not confirm this impression, given the quality of a fit of a constant of $\chi^2/\text{ndf} = 15.2/7$ with a probability of 3.5%[4].

To further investigate the multi-source hypothesis, two emission regions A and B (shown in Fig. 5.10, left) have been determined. The radii of 0.35° and 0.25° of region A and B, respectively, have been chosen such that all of the emission from these regions was encompassed. A one-dimensional slice in the uncorrelated excess image along the major axis between the two regions has been produced. Even if the fit of two separate sources with Gaussian shape results in a good χ^2 of 3.7 for 4 degrees of freedom, the emission across the slice in the region of interest (indicated by the dotted lines in Fig. 5.10, top-right) is

[4] An azimuthal profile shifted by half a bin width results in a $\chi^2/\text{ndf} = 20/7$ with a probability of 0.6%.

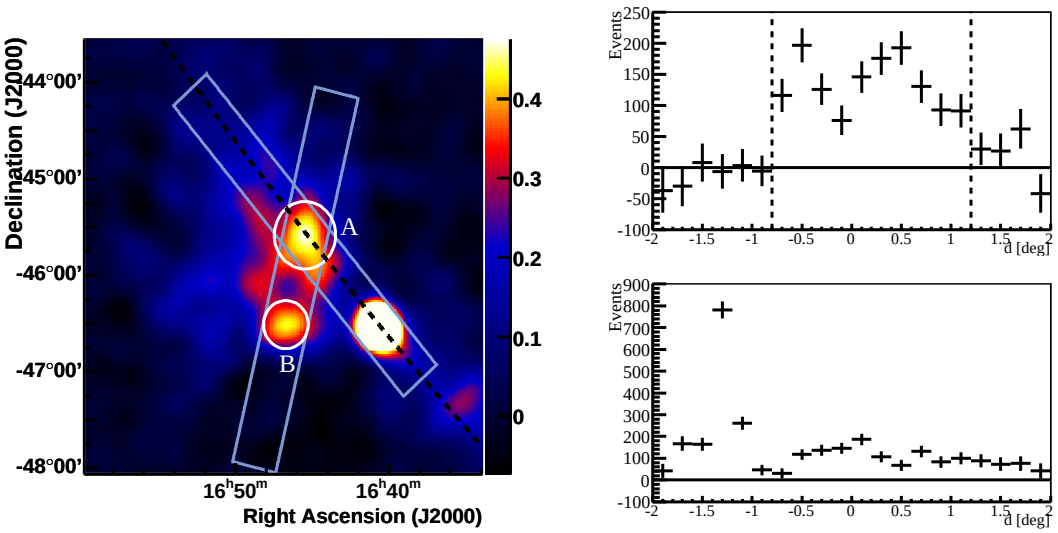

Figure 5.10: (Left:) Smoothed excess map of the $4.5° \times 4.5°$ f.o.v. around Wd 1. Overlaid are blue-grey boxes which depict regions which were used to extract the one-dimensional slices shown on the right side. (Right:) One-dimensional excess distribution along the region A and B (top), starting at negative Declinations and along the Galactic plane (bottom), starting in the HESS J1640–465 direction.

Region	RA °	Dec °	θ °	Excess events	Significance σ
Full – *Template*	251.71	-45.82	1.1	2797 ± 134	18.5
Full – *Ring*	251.71	-45.82	1.1	2316 ± 197	11.5
A – *Template*	251.37	-45.59	0.35	474 ± 49	10.5
B – *Template*	251.68	-46.51	0.25	252 ± 34	8.0

Table 5.2: Statistics for region A and B (shown in Figure 5.10), compared with the statistics from the entire source region as obtained with different background estimation methods.

never more than two standard deviations away from a constant value. Figure 5.10, left also suggests a contribution of diffuse VHE γ-ray emission along the Galactic plane, which extents $1 - 2°$ from region A north-eastwards. This impression is supported by the one-dimensional slice shown in Fig. 5.10, bottom-right, where the significance of the emission in all bins with $0.5° \leq d \leq 1.8°$ is between $2 - 4\sigma$. This diffuse emission could be due to unresolved VHE γ-ray sources and/or a Galactic diffuse emission component, caused by the interaction of GCRs with molecular material located along the Galactic plane. The statistics of region A and B compared to the entire source region are given in Table 5.2.

Even though the studies presented before showed no clear evidence for a multi-source morphology and do not support a separation into multiple VHE γ-ray sources, spectral variations across the whole emission region could indicate different physical acceleration processes from multiple sources and/or transport as well as energy-loss processes in a single source. In that case, an energy-dependent morphology would be apparent. To test this

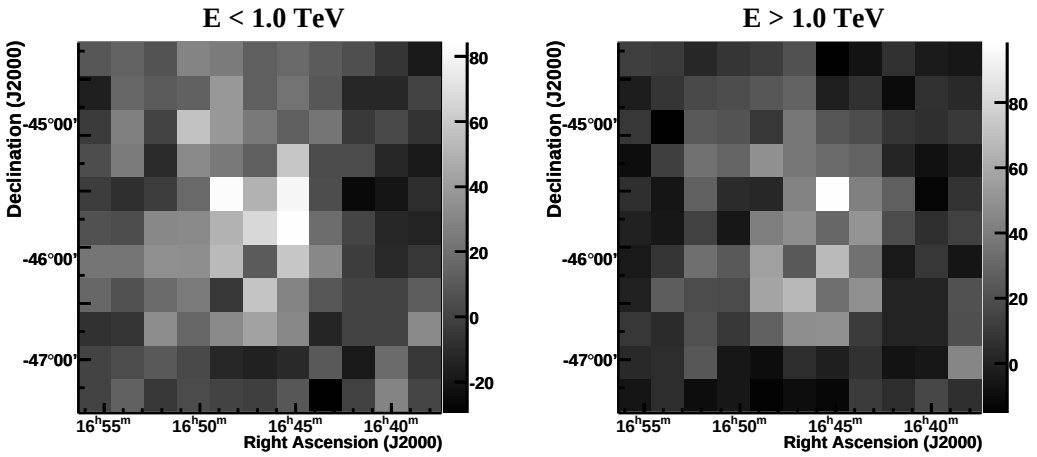

Figure 5.11: Uncorrelated VHE γ-ray excess map in bins of 0.3° width for events with reconstructed energies $E < 1.0$ TeV (left) and $E > 1.0$ TeV (right). A statistical test reveals a χ^2 of 95.4 for 76 degrees of freedom with a probability of 6.5% that both excess maps follow the same underlying distribution.

hypothesis, the complete data set has been divided into a low-energy band, just containing events with energies $E < 1.0$ TeV and a high-energy band, just containing events with energies $E > 1.0$ TeV. The unsmoothed excess maps in coarse bins of 0.3° width for the two energy bands are shown in Fig. 5.11. A χ^2 can be calculated using the number of excess events in each bin:

$$\chi^2 = \sum_{i=1}^{i=k} \frac{(h_i - N \cdot l_i)^2}{\sigma_{h,i}^2 + N^2 \cdot \sigma_{l,i}^2} \ , \tag{5.1}$$

where k denotes the number of considered bins, h_i and l_i the excess in bin i, σ_i the corresponding errors and $N = N_h/N_l$ the normalisation between total number of excess events in the two maps. This statistical test reveals a χ^2 of 95.4 for 76 degrees of freedom. The probability that both excess maps follow the same underlying distribution is 6.5%. Also from this test, no source-wide energy-dependent morphology change seems to be apparent.

5.5 Spectral analysis

Given the extension of the source of >2° and the fact that observations have been carried out within regions of VHE γ-ray emission, the *On-Off* background estimation model has been used to extract spectral information. In this method, the CR background is subtracted from the *On-Region* using observations taken without any VHE γ-ray signal in the f.o.v.. To guarantee similar observation conditions between *On-* and *Off-data*, only *On-Off* pairs of observations are considered that were taken at similar zenith angles and within four months of each other, resulting in a total live time of 20 hours for the spectral analysis. The absolute normalisation α between *On-* and *Off-data* has been calculated using the live time of each observation. The spectrum obtained for this data set using the *On-Off* background estimation method is shown in Fig. 5.12. It is well described by a power law: $dN/dE =$

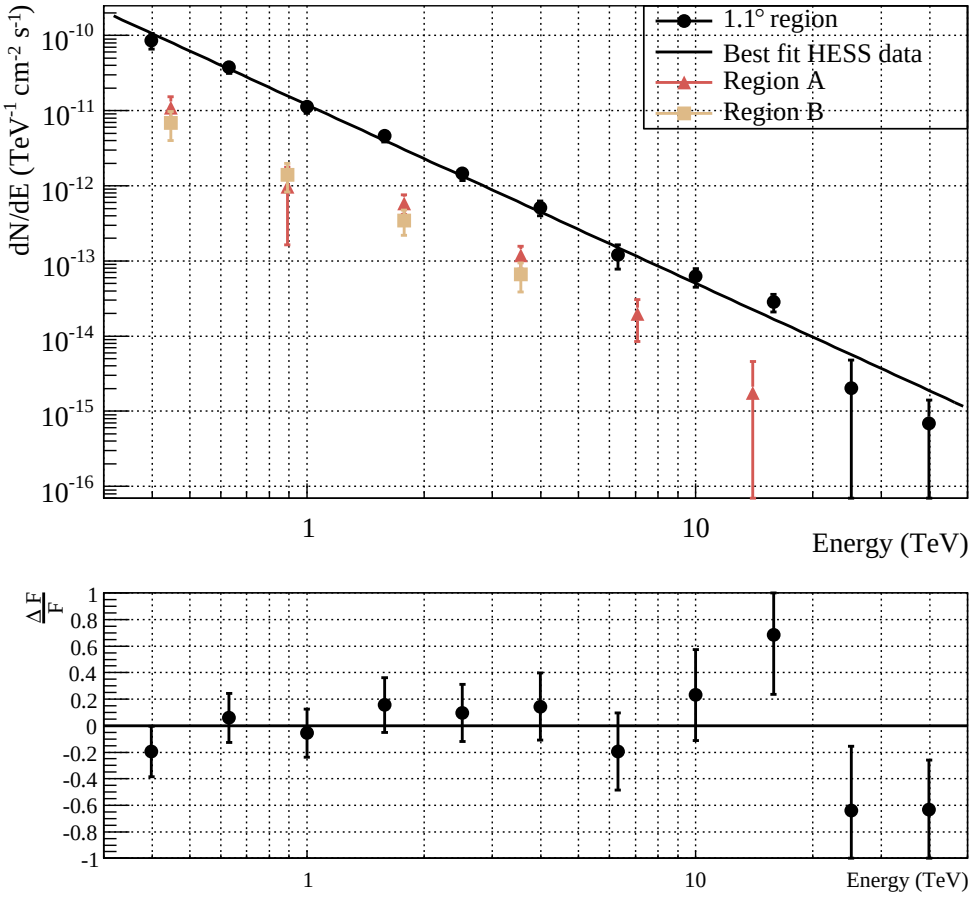

Figure 5.12: Differential energy spectrum of different regions of Wd 1. Shown is the spectrum of the whole 1.1° integration region as indicated in Fig. 5.2 as black filled circles. Spectra of region *A* and *B* are drawn as red filled triangles and brown filled squares, respectively.

$\Phi_0 \cdot (E/1\ \mathrm{TeV})^{-\Gamma}$ with photon index $\Gamma = 2.34 \pm 0.06_{\mathrm{stat}} \pm 0.2_{\mathrm{sys}}$ and differential flux normalisation $\mathrm{N_0} = (11.8 \pm 0.92_{\mathrm{stat}} \pm 1.2_{\mathrm{sys}}) \times 10^{-12}\,\mathrm{TeV^{-1}\,cm^{-2}\,s^{-1}}$. This translates into an integral flux between $(0.2-10)$ TeV of $F(0.2-10\,\mathrm{TeV}) = (7.64 \pm 0.74) \times 10^{-11}\,\mathrm{cm^{-2}\,s^{-1}}$.

Additionally, the differential energy spectrum for region *A* for an integration radius of 0.35° and of region *B* with an integration radius of 0.25° has been performed. The integrated flux between 0.2 TeV and 10 TeV as well as the photon indices obtained from a power-law fit are summarised in Table 5.3 and compared to the results for the spectral analysis of the whole 1.1° region. The differential energy spectra for these two regions are shown in Fig. 5.12 as well. Within statistical errors, no change in photon index between the three studied regions is apparent, further supporting that there is no evidence for multiple sources. In the following, astronomical objects which could be possibly associated to the observed extended VHE γ-ray emission are discussed in more detail.

Region	$F(0.2-10$ TeV) $\times 10^{-11}\,\mathrm{cm}^{-2}\,\mathrm{s}^{-1}$	% total	Γ
Full	7.64 ± 0.74	100	2.34 ± 0.06
A	1.44 ± 0.29	19 ± 4	2.32 ± 0.12
B	1.00 ± 0.24	13 ± 3	2.42 ± 0.20

Table 5.3: Integral fluxes of region A and B (shown in Fig. 5.10), compared to the integral flux from the entire source region. The photon index Γ is derived from a fit of a power-law to the spectrum for each region. Only statistical errors are shown.

5.6 Possible associations

Beside the stellar cluster Westerlund 1, which could act as a particle accelerator as discussed in Section 3.2, standard catalogues of objects which are thought to be potentially associated to VHE γ-ray sources have been searched for counterparts of the emission detected by H.E.S.S.. This search comprised SNRs (Green 2009), high spin-down-flux pulsars (Manchester et al. 2005) and objects detected by the Fermi LAT (Abdo et al. 2010). Additionally, X-ray sources from the ROSAT bright source catalogue (Voges et al. 1999), the XMM Slew survey catalogue (Saxton et al. 2008) and objects identified in hard X-rays by INTEGRAL (Bird et al. 2007) have been investigated as potential counterparts and are discussed individually. Fig. 5.13(a) and 5.13(b) show the Molonglo radio map at 843 MHz (Murphy et al. 2007) and the 1.4 GHz map of neutral hydrogen at a velocity of ~ -55 km/s as obtained from the Southern Galactic Plane Survey (SGPS) (McClure-Griffiths et al. 2005), respectively. Overlaid are all objects found in the mentioned catalogues.

5.6.1 ROSAT

GX340+0 was detected by INTEGRAL and also by ROSAT and XMM-Newton[5] (object A in Fig. 5.13(b)) and is a prominent LMXB which shows recurrent outbursts. Even though this object coincides with the peak of the observed VHE γ-ray emission seen at the Galactic plane, a spectral and temporal analysis has not revealed any significant flux variations during the H.E.S.S. observations. GX340+0 would appear as a point-like source in the H.E.S.S. data, whereas the VHE γ-ray emission is of extended nature.

The source 1RXS J164658.8–464308 (object B in Fig. 5.13(b)) is at the edge of the southern VHE γ-ray emission peak and has been identified in the ROSAT all-sky survey as a bright source. It has not been associated to a source class in any other wavelengths band yet. Since the nature of this X-ray source is unclear, multiwavelength observations could help to identify this object and its potential contribution to the observed VHE γ-ray emission.

[5] It was detected as 1RXS J164547.8–453642 and XMMSL1 J164548.2–453640, respectively

5.6.2 XMM-Newton

In 0.1° distance to the ROSAT object B a source has been detected by XMM-Newton during the Slew Survey (Saxton et al. 2008). XMMSL1 J164715.3–463659, referred to as object C in Fig. 5.13(b), has been found in an effective exposure of 2.4 seconds with an estimated energy flux in the hard band between $2 - 12$ keV of $(1.67 \pm 0.77) \times 10^{-11}$ erg cm^{-2} s^{-1}. The source seems to be extended for XMM-Newton with a size of $11.85 \pm 3.8''$[6]. Future Chandra observations could further resolve the spatial extent of the X-ray source and possibly connect the X-ray emission with the observed VHE γ-ray emission. If the X-ray emission is indeed extended or if an extended X-ray nebula is detected around a bright point-like source, an identification with a previously unknown PWN, is likely. This PWN could power the emission seen from region B.

5.6.3 Integral

All INTEGRAL sources in the f.o.v. are related to the class of X-ray binaries, which are comprised of a compact object, the accretor – a white dwarf, neutron star or stellar black hole – that accrets matter or stellar wind material from a binary companion star, the donor. In case the donor is a massive O,- B,- Be- or blue hypergiant star, the binary system belongs to the class of High-Mass X-ray binaries (HMXBs). In case the stellar component is a main sequence star or an evolved star, the binary system belongs to the class of Low-Mass X-ray binaries (LMXBs).

Three out of four INTEGRAL sources are spatially coincident with the extended VHE γ-ray emission seen in the Wd 1 vicinity. Of these three, two are associated to a special class of HMXBs, so-called Supergiant Fast X-ray transients, (SFXTs)[7]. SFXTs show short ($\mathcal{O}$(hrs)), strong ($\mathcal{O}(10^3 - 10^4)$ increase) hard X-ray outbursts. Spectral analyses on the two SFXTs coincident with the emission seen by H.E.S.S. showed no flux increase during any of the observations. Furthermore, the VHE γ-ray emission is of extended nature, whereas SFXTs would emit γ rays which appear point-like for H.E.S.S.. Therefore, an association with one of these objects is unlikely.

5.6.4 Fermi

The Fermi LAT collaboration recently published the 1-year catalogue of HE γ-ray sources, detected in a point-like source analysis, using data from 11 months of observation (Abdo et al. 2010). Of these, three are found to (partially) coincide with the VHE γ-ray emission and are in the following investigated as potential counterparts. They are all non-variable and have significant flux in the $10-100$ GeV band. That makes these HE γ-ray sources also potential VHE γ-ray sources. A spectral analysis of the H.E.S.S. data on the positions of the Fermi sources has been performed. Since the extension (95%) of 1FGL J1648.4–4609c is smaller than the H.E.S.S. PSF, a point-like nature of the emission with $\theta^2 = 0.0125$ was assumed. To account for the extended nature of 1FGL J1649.3–4501c and 1FGL J1651.5–

[6] The XMM PSF is given as 6.6″ for the conducted observation mode.

[7] IGR J16479–4514 and IGR J16465–4507 have been identified as such objects in X-ray- (Negueruela et al. 2006) and IR observations (Nespoli et al. 2008)

Region	θ (deg)	$F(0.2-10$ TeV) $\times 10^{-11}\,\mathrm{cm}^{-2}\,\mathrm{s}^{-1}$	% total	Γ
Full	1.10	7.64 ± 0.74	100	2.34 ± 0.06
1FGL J1648.4–4609c	0.11	0.14 ± 0.07	2 ± 1	2.39 ± 0.38
1FGL J1649.3–4501c	0.22	0.45 ± 0.27	6 ± 4	2.80 ± 0.46
1FGL J1651.5–4602c	0.22	0.42 ± 0.19	5 ± 2	2.41 ± 0.31

Table 5.4: Integral fluxes of possible Fermi counterparts (shown in Fig. 5.13(a)), compared with the integral flux from the entire source region. The photon index Γ is derived from a fit of a power-law to the spectrum for each region. Only statistical errors are shown.

4602c, which is larger than the H.E.S.S. PSF, a slightly extended emission ($\theta^2 = 0.05$) was assumed in the analysis. The extrapolated best power-law fits to the Fermi data together with the measured H.E.S.S. flux are shown in Fig. 5.14. Notably, all extrapolated Fermi spectral fits overpredict the measured H.E.S.S. flux. However, in the 1-year catalogue, all Fermi sources are marked as found in a region with a bright and/or possibly incorrectly modelled diffuse Galactic plane emission, why the spectral results in the high-energy regime have to be seen with some care. Whereas 1FGL J1648.4–4609c is spatially coincident with the pulsar PSR J1648–4611, the other two sources could not be associated to an object like e.g. a SNR or a pulsar. Table 5.4 summarises the spectral results from the analyses of the H.E.S.S. data on the three Fermi source positions. The sum of the integral flux of the three regions accounts for $13 \pm 5\%$ of the total observed emission in VHE γ rays.

5.7 Interpretation of the VHE γ-ray emission

In the following, two possible VHE γ-ray emission scenarios are investigated in more detail:

- ◇ A leptonic and hadronic scenario, where Westerlund 1 is responsible for the observed VHE γ-ray emission.
- ◇ A leptonic PWN scenario, where PSR J1648–4611 is responsible for the HE emission seen from 1FGL J1648.4–4609c and (parts of) the observed VHE γ-ray emission.

5.7.1 Particle acceleration in and around Westerlund 1

The theoretical considerations presented in Section 3.2 showed that particles in young massive stellar clusters can be accelerated either in the colliding winds of massive stars, or via diffusive or turbulent particle acceleration. Wd 1 harbours ≥ 24 WR stars, largely bound in binary systems, which could accelerate electrons to very high energies as shown in Section 3.1. In that case, the strong photon fields of the stellar cluster member stars would serve as target for the IC process. Given the core size of $25''$ of Wd 1, any VHE γ-ray emission produced via this mechanism would appear point-like for H.E.S.S.. However, at the position of the stellar cluster no significant point-like source on top of the extended

γ-ray excess is seen. Hence, a significant contribution from the collective effect of multiple CWBs to the observed VHE γ-ray emission is not likely.

The presented counterpart search suggests that none of the discussed objects can explain the overall VHE γ-ray emission and in particular the northern emission region coincident with the Galactic plane. In the following, a scenario where Westerlund 1 is the source of hadronic CRs which produce the observed VHE γ-ray emission in interactions with the ambient medium is presented and investigated in more detail.

Westerlund 1 – Energetics

Under the assumption that hadronic CRs produce the observed VHE γ-ray emission and follow a power-law distribution between 1 GeV and 1 PeV with same spectral index as found for the γ-ray data, the measured γ-ray luminosity in this energy band is:

$$L_\gamma = 1.0 \times 10^{36} \left(\frac{d_{Wd1}}{3.9 \text{ kpc}} \right)^2 \text{ erg s}^{-1} \, . \tag{5.2}$$

The energy in CRs is the product of the timescale typical for the *pp* interaction cross section τ_{pp} and the γ-ray luminosity L_γ, scaled by the conversion efficiency from CRs into VHE γ rays ϵ_{CR}:

$$E_{CR} = \frac{L_\gamma \cdot \tau_{pp}}{\epsilon_{CR}} \, . \tag{5.3}$$

τ_{pp} is given by Eq. 3.12 as:

$$\tau_{pp} \approx 1.7 \times 10^{15} \left(\frac{n_\text{H}}{\text{cm}^{-3}} \right)^{-1} \text{ s} \, . \tag{5.4}$$

Depending on the ambient medium density n_H, the assumed distance to Wd 1 d_{Wd1} and the conversion efficiency ϵ_{CR}, the total energy in CRs required to explain the observed VHE γ-ray emission is:

$$E_{CR} = 1.7 \times 10^{52} \left(\frac{\epsilon_{CR}}{0.1} \right)^{-1} \left(\frac{d_{Wd1}}{3.9 \text{ kpc}} \right)^2 \left(\frac{n_\text{H}}{\text{cm}^{-3}} \right)^{-1} \text{ erg} \, , \tag{5.5}$$

assuming a typical conversion efficiency from CRs to VHE γ rays of 10%. According to a *Starburst99* simulation[8] (Leitherer 2010) of Westerlund 1 assuming a mass of $10^5 M_\odot$, the total kinetic energy in stellar winds of massive stars and SNe after 5 Myrs is estimated to be $E_\text{kin} = 3.1 \times 10^{53}$ erg. If 5% of the available kinetic energy are transferred into the acceleration of CRs, this would be sufficient to generate the observed H.E.S.S. emission in *pp* interactions with an ambient medium of ISM density of 1 proton per cm^{-3}. In summary, the available kinetic energy in the system is fully sufficient to explain the measured VHE γ-ray emission.

[8] Starburst99 (Leitherer 2010) is a simulation that models the temporal stellar evolution of a cluster of stars for e.g. given mass, IMF, metallicity or wind models. Additional information about the simulation and all input parameters can be found in Appendix B.

Bubble	v km/s	d pc	age Myrs
B1	5	5	0.15
B2	≥ 5	10×18	< 0.6
B3	~ 3	50	$4.5 - 5.0$

Table 5.5: HI bubble parameters as derived by Kothes & Dougherty (2007). For all quantities, a distance to Wd 1 of 3.9 kpc was assumed. The age of the stellar wind bubbles B1 and B2 was estimated following Crowther et al. (2006) using the quantity $t_{\rm Myr} = 0.29 \cdot R_{\rm pc}/v_{\rm km/s}$. The expansion velocity of B3 was estimated using the same quantity, but assuming an age of $4.5 - 5.0$ Myrs.

Westerlund 1 – Neutral environment

The energy in CRs required to generate the VHE γ-ray emission linearly depends on the ambient medium density in the vicinity of Wd 1. Following Kothes & Dougherty (2007), more accurate estimates of the ambient medium density are derived and the morphology of the Westerlund 1 surroundings is discussed using neutral hydrogen (HI) data from the SGPS (McClure-Griffiths et al. 2005). By means of HI absorption features in the Westerlund 1 direction, Kothes & Dougherty (2007) derive a distance to Wd 1 of 3.9 ± 0.7 kpc. The authors investigated the neutral environment of Wd 1 at the corresponding proper motion of the surrounding gas at a velocity of -55 km/s on angular scales of $\sim 2^\circ$, similar to the extension of the γ-ray emission. As a result of their studies, they find three expanding bubbles of different size which they interpret as blown by stellar wind activity during different evolutionary stages of Wd 1. Fig. 5.15 shows the neutral hydrogen map on scales of $2.5^\circ \times 2.5^\circ$ at a velocity of -55 km/s. Overlaid are the three bubbles B1, B2 and B3 as ellipses of different colour and the H.E.S.S. excess contours. The bubble parameters as derived by Kothes & Dougherty (2007) are summarised in Table 5.5. The authors conclude that the smaller bubbles B1 and B2 could have been created by the stellar winds of cluster member stars after the last SN explosion, which occurred less than 0.6 Myr ago. The larger bubble B3 is interpreted as stellar wind bubble, created $4.5 - 5.0$ Myrs ago, during an early evolutionary stage of the member stars.

Apparently, the higher density regions at the edge of the HI bubble B3 seem to be correlated to the northern VHE γ-ray emission region. Also to the east, some overlap between VHE γ-ray emission and the HII region complex G340.2 − 0.2 is obvious. Kothes & Dougherty (2007) interpret the formation of this HII region as triggered by the stellar wind activity of Wd 1. Indeed, if Wd 1 is located at this distance, some correlation between VHE γ rays and this HII region is expected.

Interstellar material with temperatures of $80 - 100$ K usually implies a particle density of $20 - 50$ protons per cm^{-3} (Ferrière 2001). Such a high density would reduce the required amount of kinetic energy transferred into CRs in these regions by $\sim 1 - 2$ orders of magnitude. For bubbles B1 and B2 Kothes & Dougherty (2007) suggest that these are now filled with material expelled by massive stellar winds, after the last SN explosion, which swept away all material. They estimate a total mass in the two bubbles of ≈ 350 $M_\odot \pm 50\%$

what infers a density of:

$$\rho_{B1,B2} \approx 3.4 \cdot \left(\frac{M_{B1,B2}}{350\ M_{\odot}}\right)\left(\frac{R_{B2}}{10\ \mathrm{pc}}\right)^{-3}\ \rho_{\mathrm{ISM}}\ , \tag{5.6}$$

a factor 10 smaller compared to the HI shell created by bubble B3. In summary, the HI gas located in the direct vicinity of Wd 1 has a density of $\rho \sim 5 - 50$ cm^{-3} and can serve as a perfect target for accelerated hadrons and VHE γ-ray production in *pp* interactions.

As opposed to the three bubbles, located in the Wd 1 surroundings, the southern VHE γ-ray emission regions are either not covered by the SGPS or do not have a clear association to higher-density regions in HI at the Wd 1 distance. This could be indicative for an incorrect distance estimate to Wd 1 and hence a different structure of the gaseous environment, which would serve as target material for the CRs accelerated in Wd 1. On the other hand, a different origin of the γ-ray emission, e.g. in a PWN scenario for region *B* and/or for 1FGL J1648.4–4609c as presented in the next section is also plausible.

5.7.2 PSR J1648–4611/1FGL J1648.4–4609c

In a PWN, the VHE γ-ray radiation is believed to originate from electrons, accelerated to very high energies by the central pulsar, which up-scatter ambient photons via the IC process. Important for a possible association between a PWN and a VHE γ-ray source is the spin-down luminosity of the pulsar $\dot{E}$. $\dot{E}$ has to be high enough to explain the measured γ-ray flux on earth L_{γ}. The γ-ray luminosity at a distance D to the pulsar can be related to the current spin-down luminosity of the pulsar by a conversion efficiency $\epsilon_{\gamma} = (4\pi D^2 L_{\gamma})/\dot{E}$. In the case of PSR J1648–4611, the spin-down luminosity $\dot{E} = 2.1 \times 10^{35}$ ergs s^{-1}. From dispersion measurements, D is determined to 5.71 kpc (Taylor & Cordes 1993) and 4.96 kpc (Cordes et al. 2002), depending on the model of the free Galactic electron distribution. L_{γ} at distance D in the energy range $(0.5 - 10)$ TeV is then $(2.3 - 3.0) \times 10^{33}$ ergs s^{-1} using the spectral results as given in Table 5.4. With these measurements, the conversion efficiency from spin-down power into VHE γ-rays is $\epsilon_{\gamma} \approx 1.0 - 1.5\%$. The extrapolation of the H.E.S.S. spectrum to 1 GeV as suggested by the Fermi detection results in a rather large $\epsilon_{\gamma} \approx 15 - 25\%$. However, ϵ_{γ} can only be seen as an upper limit to the true conversion efficiency since only the current spin-down power of the pulsar is considered in the estimation. Electrons emitted at earlier times when the pulsars' $\dot{E}$ was larger could contribute to the observed HE/VHE γ-ray emission too. This is of particular importance for PSR J1648–4611, given its spin-down age of 1.1×10^5 yrs. Other VHE γ-ray sources which are firmly associated to PWN have conversion efficiencies of $\epsilon_{\gamma} \lesssim 10\%$ (Gallant 2007), compatible with the results found here. On the other hand, an ϵ_{γ} of $60 - 85\%$ would be required to explain the whole emission seen in VHE γ rays in the energy range $0.5 - 10.0$ TeV in a PWN scenario. Moreover, the size of the γ-ray emission of 2.0° translates into a physical size of $170 - 200$ pc at the estimated pulsar distances. This extension is much larger compared to the size of the e.g. Vela X PWN (Aharonian et al. 2006c) or HESS J1825–137 (Aharonian et al. 2006g) of $\mathcal{O}(10)$ pc. For such a large nebula, an energy-dependent morphology as found for HESS J1825–137 could be expected and indicate energy-dependent cooling times of the parent electron population. As shown in Section 5.4 and 5.5 neither a significant change in morphology of the VHE γ-ray emission nor a significant change of spectral index across the source was found in

the analysis of the H.E.S.S. data. The large ϵ_γ and the non-detection of energy-dependent morphology makes an association of the whole VHE γ-ray emission and the possible PWN of PSR J1648–4611 unlikely. However, the source found by Fermi is spatially coincident with PSR J1648–4611 and could explain some of the observed H.E.S.S. emission in a PWN scenario. Just recently, Luna et al. (2010) reported on a cavity which is surrounded by a fragmented molecular shell (found in archival CO data), which is located in the Norma near arm at a systemic velocity of -90 km/s. They interpret the VHE γ-ray emission as originating from the inner wall of the expanding shell of the stellar remnant PSR J1648–4611 with the molecular material. The authors conclude that Wd 1 cannot be responsible for the H.E.S.S. emission. However, the age of the cavity derived by the authors of $\sim 10^6$ years does not match the spin-down age of PSR J1648–4611 of 1.1×10^5 years. Moreover, the kinetic energy in CRs, required to explain the γ-ray emission as given in Eq. 5.5 is an order of magnitude larger compared to the energy available in the proposed stellar explosion.

5.8 Nature of emission

The theoretical considerations made in Section 3.2 imply that CRs can be accelerated in stellar clusters via DSA in strong shocks of SNR shells or via turbulent particle acceleration on plasma waves and MHD turbulences. So far, no SNR shell or strong supersonic shocks as expected for the Weaver et al. (1977) model could be detected in any wavelength band in the vicinity of Wd 1. However, the detection of a Magnetar in Wd 1 implies that $80 - 150$ massive stars must have undergone SN explosions in the history of Wd 1 (Muno et al. 2006b), providing a vast amount of kinetic energy. If just a minor fraction of $0.1 - 1.5\%$ of this energy is channelled into CRs via turbulent particle acceleration, this could easily explain (parts of) the overall VHE γ-ray emission morphology as produced in *pp* interactions and subsequent π^0 decay in the surrounding HI gas. The emission seen from region B, however, can presumably not be explained in this picture. A possible identification of XMMSL1 J164715.3–463659 as a PWN in future Chandra observations could help to disentangle the emission seen by H.E.S.S. in the VHE regime. Also a partial contribution from PSR J1648–4611/1FGL J1648.4–4609c in a PWN scenario is possible.

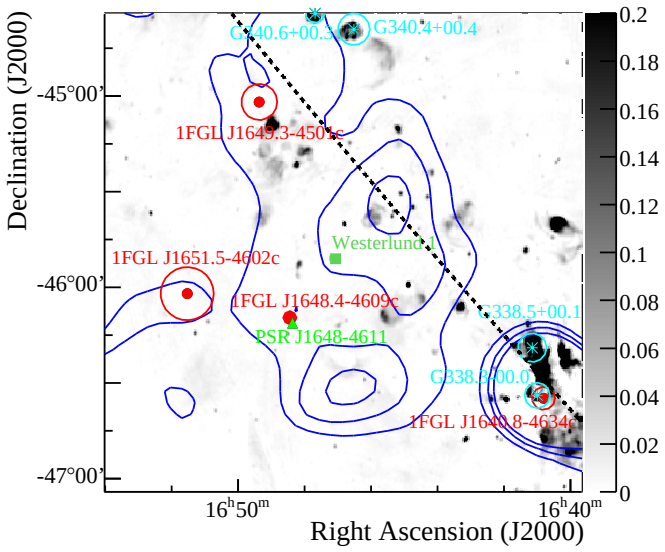

(a)

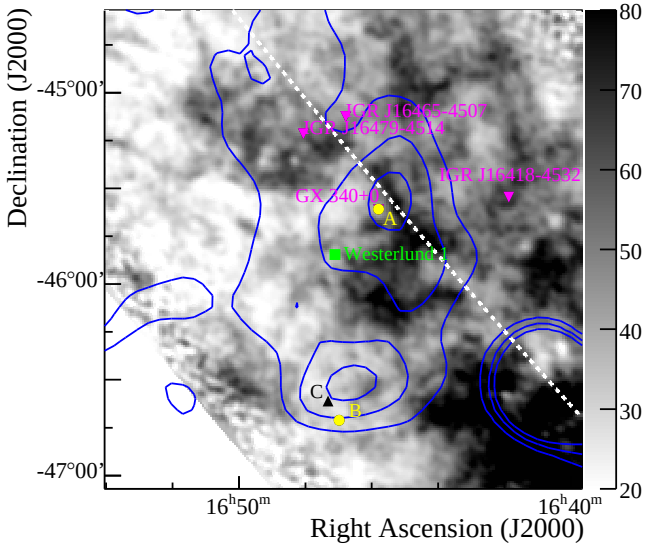

(b)

Figure 5.13: (a) H.E.S.S. smoothed VHE γ-ray excess contours in blue (0.25, 0.35, 0.45 events per arcmin^2) overlaid on the Molonglo 843 MHz map (Murphy et al. 2007) (grey scale, in Jy). Overlaid are SNRs (Green 2009) as cyan circles, pulsars with a spin-down flux on earth, $\dot{E}/\mathrm{d}^2$, greater than 5×10^{33} ergs s^{-1} kpc^{-2} (Manchester et al. 2005) as green upright triangles and HE γ-ray sources listed in the Fermi 1-year catalogue (Abdo et al. 2010) as red circles. (b) HI channel map at 1.4 GHz (McClure-Griffiths et al. 2005) (grey scale, in K) at a velocity of ~ -55 km/s. INTEGRAL sources (Bird et al. 2007) are overlaid as pink downright triangles and yellow circles represent the ROSAT sources 1RXS J164547.8–453642 (A) and 1RXS J164658.8–464308 (B). The XMM-Newton Slew Survey source XMMSL1 J164715.3–463659 (Saxton et al. 2008) is denoted as object C as black upright triangle. The INTEGRAL sources GX340+0 and IGR J16418–4532 were also detected in the XMM-Newton Slew Survey.

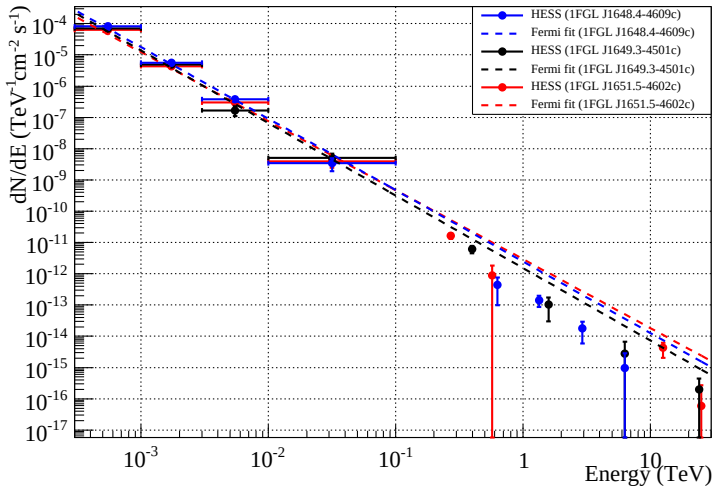

Figure 5.14: H.E.S.S. spectra as resulting from source analyses on the positions of the Fermi sources 1FGL J1648.4–4609c (blue filled circles), 1FGL J1649.3–4501c (black filled circles) and 1FGL J1651.5–4602c (red filled circles). The extrapolated best power-law fits of the Fermi data are depicted as lines in corresponding colours. Fermi spectral points are shown in corresponding colours.

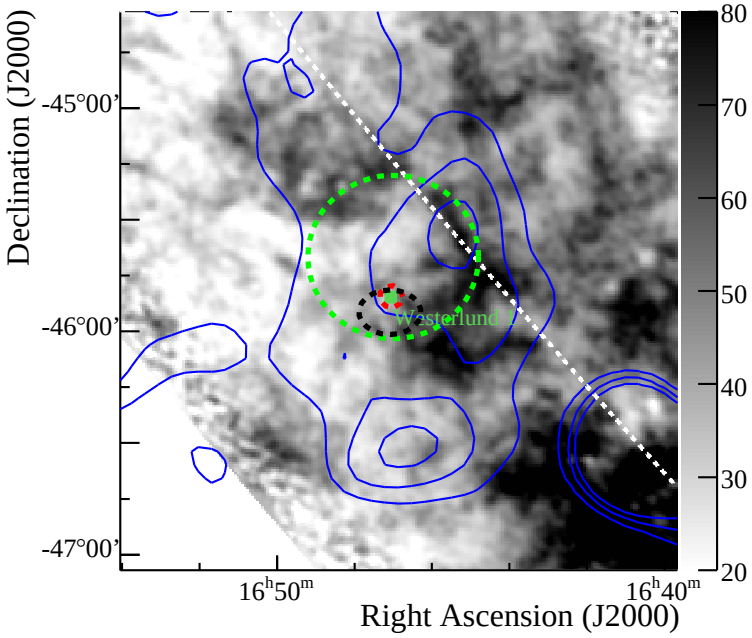

Figure 5.15: $2.5° \times 2.5°$ f.o.v. of the HI channel map at -55 km/s as shown in Fig. 5.13(b). Overlaid are smoothed H.E.S.S. excess contours. The red dashed circle depicts the HI bubble B1, the black dashed ellipse the bubble B2 and the green dashed circle bubble B3 as discovered by Kothes & Dougherty (2007).

6 VHE γ-ray observations of NGC 253 with H.E.S.S.

Starburst galaxies are characterised by a high supernova rate in the central region of the galaxy – the SB nucleus. As discussed in Section 3.3, this high SN rate – and hence high CR density – in combination with the large amount of gaseous material in the SB nucleus leads to a VHE γ-ray flux predicted to be detectable by IACTs. NGC 253 on the southern hemisphere and its twin, M 82, on the northern hemisphere are the closest objects and archetypal for the class of SB galaxies. This chapter will focus on VHE γ-ray observations of NGC 253. After an introduction of the characteristics of this object in Section 6.1, Section 6.2 presents the data collected in long-time observations of NGC 253 and the analysis of this data using the advanced analysis technique presented in Chapter 2. Finally, in Section 6.4 the detection of VHE γ-ray emission from NGC 253, the first external spiral galaxy seen in VHE γ rays, is discussed in the context CR properties, energy-loss and transport processes.

6.1 The SB galaxy NGC 253

NGC 253, located in the Sculptor Group of galaxies, is the closest object in the southern hemisphere which belongs to the class of SB galaxies. The distance to NGC 253 is measured to $(2.6 - 3.9)$ Mpc using different distance estimation techniques. Davidge et al. (1991) e.g. utilised AGB stars, whereas Karachentsev et al. (2003) used the tip of the red giant branch and Rekola et al. (2005) Planetary nebulae to derive the distance. The reference distance used in this work is 2.6 Mpc (Davidge et al. 1991) since this value is used in most of the quoted works. However, it has to be noted that this estimate is afflicted with a considerable error.

Compared to the Milky Way, NGC 253 exhibits an increased star formation rate and hence a high SN rate ν_{SN} in the SB nucleus. Since SNe are believed to be the major source of Galactic CRs, the CR density in the SB region of NGC 253 is expected to be high. The SN rate can be determined using IR observations, since the FIR luminosity can be assumed to be directly proportional to ν_{SN}. Van Buren & Greenhouse (1994) found a relation which connects the FIR luminosity L_{FIR} with ν_{SN}:

$$\nu_{SN} \approx 2 \times 10^{-12}\ L_{FIR,\odot}\ \mathrm{yr}^{-1}\ . \tag{6.1}$$

Van Buren & Greenhouse (1994) derived a SN rate of $\nu_{SN} \approx 0.08\ \mathrm{yr}^{-1}$.

The SB activity in the Galactic nucleus of NGC 253 induces a Galactic wind (McCarthy et al. 1987; Zirakashvili & Völk 2006), which basically transports hot gas from the SB nucleus into the IGM. As shown in Section 3.3, the scale height and velocity of the Galactic

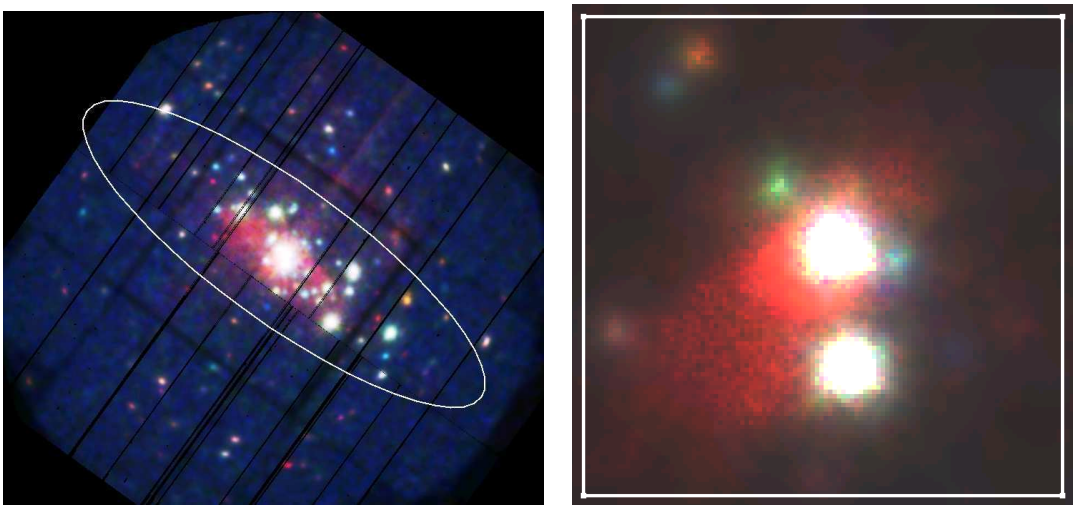

(a) (b)

Figure 6.1: NGC 253 as seen in X-rays by the XMM-Newton satellite. (a) The $30' \times 30'$ region around the optical centre of the galaxy (colour code: $0.3-2.0$ keV in red, $2.0-4.0$ keV in green and $4.0-10.0$ keV in blue). The white contour depicts a constant magnitude brightness of 25 per arcsec^2. (b) Zoom into the central $2' \times 2'$ region of NGC 253 of image (a). The extended red structure is the Galactic wind, reported by Pietsch et al. (2001) (Figures taken from Barnard et al. 2008).

wind determines convective and diffusive losses. Zirakashvili & Völk (2006) estimated the Galactic wind speed to 900^{+1100}_{-400} km s^{-1} following an analytical model which they applied to radio data (Mohan et al. 2005). At the boundary between the Galactic wind and the IGM a strong termination shock forms, which is believed to re-accelerate CRs via DSA to energies of up to $\approx 3 \times 10^{20}$ eV (Anchordoqui et al. 1999).

Some of the properties reviewed before are relevant for estimating the γ-ray luminosity of the CR population in NGC 253. Whereas the distance to the object quantitatively determines the expected γ-ray flux on Earth, the SN rate is directly related to the CR content. The high matter density in the SB region, on the other hand, determines the conversion efficiency of CRs into the production of γ rays via hadronic interactions. The Galactic wind properties, however, affect the energy loss of the CR population via convection and diffusion as shown in Section 3.3.

NGC 253 was observed in the VHE regime by HEGRA, CANGAROO and H.E.S.S.. The HEGRA collaboration derived a 99% UL from 32.5 hours of observations above an energy threshold of 5.2 TeV of $F_\gamma(> 5.2 \text{ TeV}) < 1.3 \times 10^{-13}$ cm^{-2} s^{-1} (Goetting 2005). CANGAROO II claimed the detection of VHE γ-ray emission from NGC 253 (Itoh et al. 2002) and a spectrum with integral flux of $F_\gamma(> 0.44 \text{ TeV}) = 1.4 \times 10^{-11}$ cm^{-2} s^{-1} and spectral index $\Gamma = 3.85$ in a later publication (Itoh et al. 2003). These results could not be confirmed in observations performed in 2003 by the more sensitive H.E.S.S. instrument (Aharonian et al. 2005c). Aharonian et al. (2005c) derived an 99% UL of $F_\gamma(> 0.3 \text{ TeV}) < 1.9 \times 10^{-12}$ cm^{-2} s^{-1} assuming an spectral index as found by Itoh

et al. (2003)[1]. A larger data set of 37 hours live time was analysed with the H.E.S.S. Standard Analysis and resulted in an 99.9% UL above the analysis threshold of 0.44 TeV of $F_\gamma(> 0.44 \text{ TeV}) < 6.3 \times 10^{-13}$ cm^{-2} s^{-1}, assuming a spectral index of $\Gamma = 2.1$ (Nedbal 2008). The 3σ hint of a signal seen in the analysis of the same data set with the BDT method triggered further observations of NGC 253 with H.E.S.S. in 2008 and 2009. The ζ analysis results of the much larger data set are discussed in the following.

6.2 VHE γ-ray data and data analysis

NGC 253 was observed with the full four-telescope H.E.S.S. array in 2005 and from $2007 - 2009$ for a total of 241 hours. Data taken under unstable weather conditions or with malfunctioning hardware has been excluded in the standard data quality selection procedure (see Section 1.3.2). After standard data quality selection and deadtime correction, the total live time amounts to 156 hours of 2,- 3,- and 4-telescope observations. For spectral reconstruction, only 4-telescope data has been considered, resulting in a lower live time of 146 hours. Observations have been carried out at zenith angles of 1° to 42°, with a small mean value of 12°. The average pointing offset from NGC 253 is 0.5°. All results presented in the following were obtained with the advanced γ/hadron separation technique introduced in Chapter 2. The analysis of a reduced data set of 119 hours live time with the BDT method (Ohm et al. 2009b) and the Model++ method (de Naurois & Rolland 2009) led to the detection of NGC 253 in VHE γ rays and a publication in Science (Acero et al. 2009). ζ_{std} cuts have been used for the generation of spectra and sky images. Spectral results have been extracted using the *Reflected* background model, whereas the *Ring* background model has been utilised to generate sky images. The analysis threshold is 245 GeV. Since the expected VHE γ-ray signal from NGC 253 is very weak, ζ_{weak} cuts, which are optimised for a 0.5% Crab source and an spectral index of $\Gamma = 2.6$, have been applied to cross-check the ζ_{std} results.

Fig. 6.2 shows an image of the acceptance corrected VHE γ-ray counts per arcmin^2 of the $2° \times 2°$ f.o.v. centred on the optical position of NGC 253. The map has been smoothed with a Gaussian kernel of $3.9'$ width to reduce the effect of statistical fluctuations. A total of 348 ± 66 excess events at a significance level of 5.5σ are found at the nominal position of NGC 253. The overall statistics of ζ_{std} and ζ_{weak} cuts can be found in Table 6.1. Also shown are the results as obtained with the H.E.S.S. Standard Analysis, demonstrating the improved γ/hadron separation potential of the BDT method compared to the Standard Analysis, which made the detection of NGC 253 in VHE γ rays possible. The best fit position of the source is $00^\text{h}47^\text{m}36.12^\text{s} \pm 3.1^\text{s}$, $-25°17'20.0'' \pm 0.9'$, J2000 coordinates, well compatible within 1σ with the optical centre of NGC 253 at $00^\text{h}47^\text{m}33.1^\text{s}$, $-25°17'18''$, J2000 coordinates.

The angular distribution of excess events relative to the NGC 253 position as shown in Fig. 6.3 is consistent with a point-like nature of the emission. This implies a source extension at a 1σ confidence level of $< 5'$. Furthermore, the γ-ray signal is stable over the four years of observations as indicated by the yearly light curve depicted in Fig. 6.4. The signal is stable and the fit of a constant to the emission reveals a mean of 1.81 ± 0.45

[1] Itoh et al. (2007), withdrew their results found earlier and derived an UL of 5.8% Crab above an energy of $E > 0.58$ TeV.

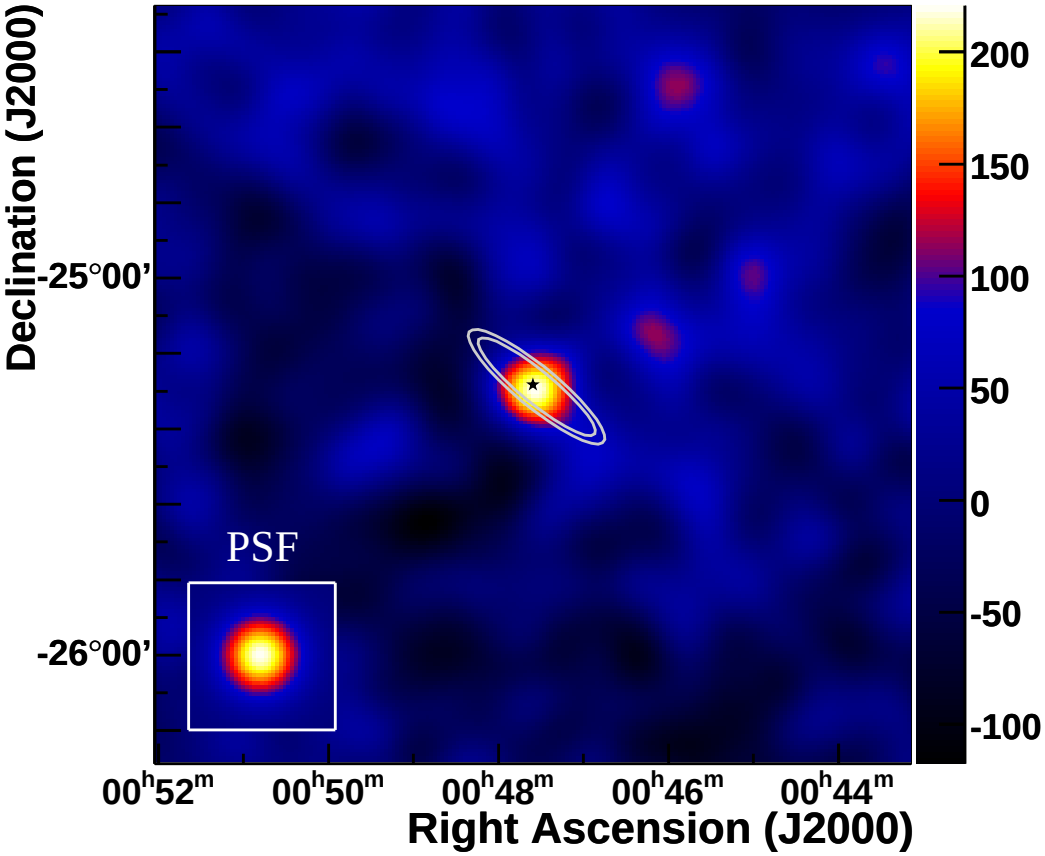

Figure 6.2: H.E.S.S. map in units of VHE γ-ray events per arcmin^2 of the $2^\circ \times 2^\circ$ f.o.v. of NGC 253. The image was smoothed with a Gaussian kernel of $3.9'$ width. The black star marks the position of the optical centre of NGC 253. The inlay represents the size of a point-like source as it would have been seen by H.E.S.S. for this analysis. White contours depict the optical emission from the whole galaxy with contour levels of constant surface brightness of 25 mag arcsec^2 and 23.94 mag arcsec^2 as used in Pence (1980).

Cuts	θ^2 $^\circ$	N_{On}	$\alpha \cdot N_{Off}$	Excess	Significance σ
std	0.0125	7258	7073	185 ± 89	2.1
ζ_{std}	0.0125	4043	3695	348 ± 66	5.5
ζ_{weak}	0.01	2424	2124	300 ± 51	6.1

Table 6.1: Number of γ-ray-like and background events as well as significance and γ-ray excess for std-cuts, compared to ζ_{std} and ζ_{weak} cuts. The *Reflected* background method has been applied to estimate the background in the signal region.

excess events per hour of live time. The quality of the fit has a χ^2 of 3.34 for 3 degrees of

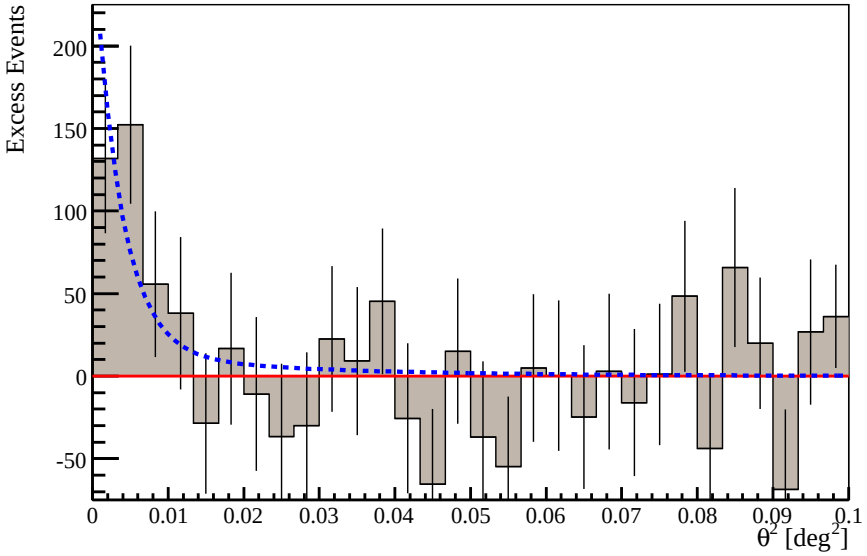

Figure 6.3: Distribution of reconstructed event directions around NGC 253. The squared angular distribution has been produced using the *Ring* background model. Also shown is the point spread function of the instrument for this analysis, assuming the γ-ray emission originates from the optical centre of NGC 253. Model and γ-ray excess are normalised in the range $0^{\circ^2} - 0.0125^{\circ^2}$.

freedom with a probability of 34%.

The differential energy spectrum as shown in Fig. 6.5 is well described by a power-law: $dN/dE = \Phi_0 \cdot (E/1\ \mathrm{TeV})^{-\Gamma}$ with photon index $\Gamma = 2.24 \pm 0.14_{\mathrm{stat}} \pm 0.2_{\mathrm{sys}}$ and differential flux normalisation $\mathrm{N_0} = (1.12 \pm 0.19_{\mathrm{stat}} \pm 0.12_{\mathrm{sys}}) \times 10^{-13}\,\mathrm{TeV}^{-1}\,\mathrm{cm}^{-2}\,\mathrm{s}^{-1}$. This translates into an integral flux above the energy threshold of 245 GeV of $F(> 245\,\mathrm{GeV}) = (5.16 \pm 0.97) \times 10^{-13}\,\mathrm{cm}^{-2}\,\mathrm{s}^{-1}$. The spectral results obtained with the ζ_{std} cuts are compatible with the spectrum as reconstructed with the ζ_{weak} cuts above the corresponding threshold energy of 295 GeV. With a flux of $(0.22 \pm 0.04)\%$ of the Crab nebula flux above 245 GeV NGC 253 is the weakest VHE γ-ray source detected so far by any IACT system. Also shown in Fig. 6.5 is the extrapolated best fit and 1σ error band of the Fermi measurement of NGC 253 in the MeV−GeV band. Within the 1σ statistical errors, the H.E.S.S. measurement and the Fermi results are compatible, in spectral index as well as extrapolated flux level. Note that NGC 253 is significantly detected by Fermi just in the energy range between $0.3 - 3.0$ GeV. Only 2σ ULs are given in the 1-year catalogue for energies below 0.3 GeV and for energies of $(3.0 - 100.0)$ GeV (Abdo et al. 2010). The spectral results from H.E.S.S. and Fermi are summarised in Table 6.2.

Fig. 6.6 compares the best fit to the H.E.S.S. spectrum as obtained with the ζ_{weak} cuts to the model predictions of Paglione et al. (1996), Domingo-Santamaría & Torres (2005) and Rephaeli et al. (2010). Within errors as stated in the previous section, the H.E.S.S. measurement is consistent with the models of Domingo-Santamaría & Torres (2005) and Rephaeli et al. (2010), which take into account convective and diffusive losses.

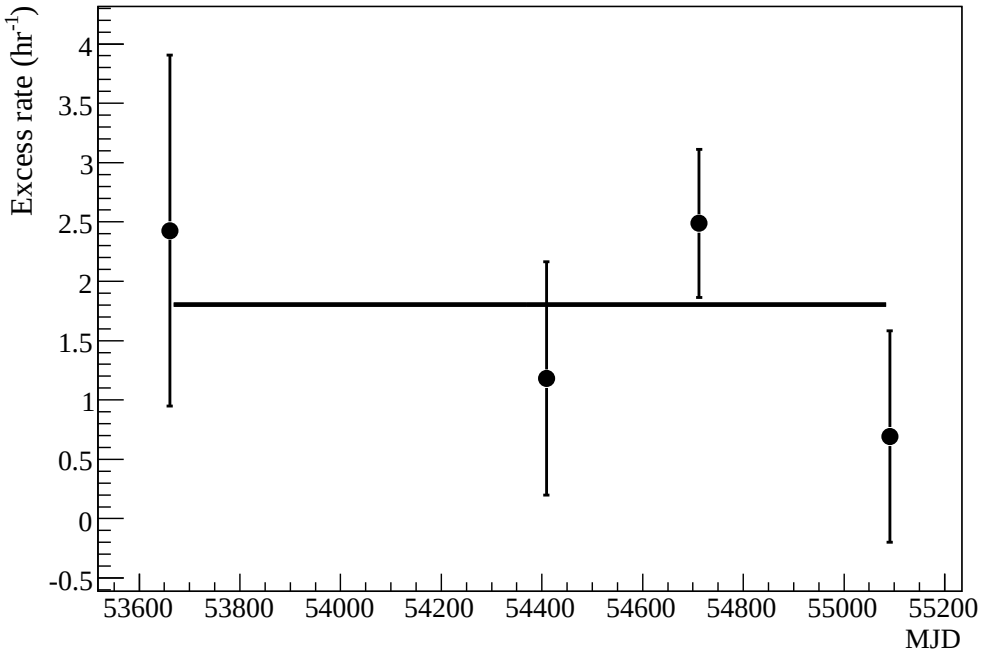

Figure 6.4: Rate of VHE γ-ray excess events for observations in 2005, 2007, 2008 and 2009. The signal is steady and stable, the fit of a constant reveals a mean of 1.81 ± 0.45 excess events per hour of live time. The fit has a probability of 34%.

Data	E	$F(E)$ $\mathrm{cm}^{-2}\,\mathrm{s}^{-1}$	Γ
Fermi	$(0.30 - 3.0)$ GeV	$(3.4 \pm 0.9) \times 10^{-9}$	2.15 ± 0.17
H.E.S.S. ζ_{std}	$(0.25 - 10.0)$ TeV	$(5.2 \pm 1.0) \times 10^{-13}$	2.24 ± 0.13
H.E.S.S. ζ_{weak}	$(0.25 - 10.0)$ TeV	$(5.1 \pm 0.9) \times 10^{-13}$	2.22 ± 0.12

Table 6.2: Integral fluxes of Fermi and H.E.S.S. data as shown in Fig. 6.5 The photon index Γ is derived from a fit of a power-law to the spectrum for each data set. Only statistical errors are given.

6.3 Background systematics of the NGC 253 data set

The following section deals with potential systematic effects in the background estimation and can be skipped if it is not of particular interest for the reader.

The measured very low γ-ray flux and an excess rate of just two VHE γ rays per hour of observation implies that just 1 out of 10^5 events from the direction of NGC 253 is a VHE γ ray. Therefore, the background reduction needs to be well understood in order to confirm the realness of the signal. In the following, systematic tests regarding the γ/hadron separation and potential background systematics are presented.

Any background systematics would result in artefacts in the sky image. If the background

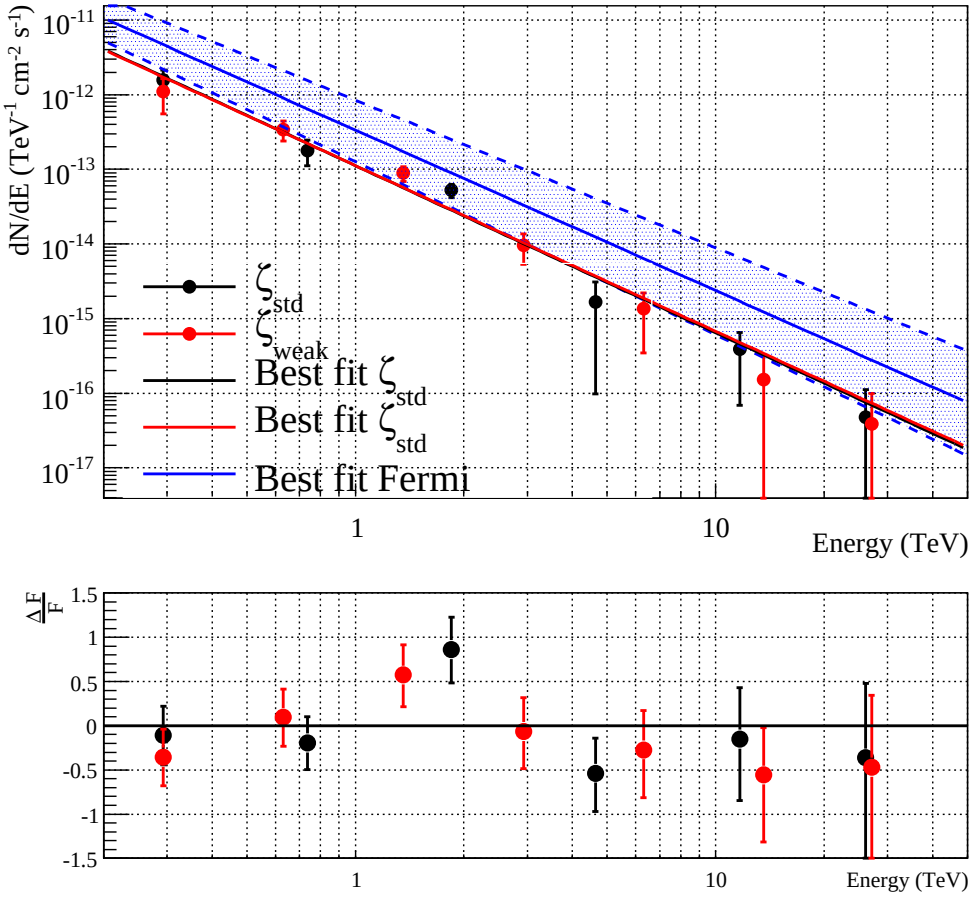

Figure 6.5: Differential energy spectrum of NGC 253 as obtained with ζ_{std} and ζ_{weak} cuts. Also shown is the extrapolated best fit of a power-law to the Fermi data between $0.3 - 3.0$ GeV. The 1σ error to the best fit parameters is indicate as blue band.

estimation works as expected, the significance distribution over the whole f.o.v. has a mean value of 0 and a width of 1. The sky image in Fig. 6.7(a) shows the large $6° \times 6°$ f.o.v. around NGC 253. Apparently, in general higher significance values at larger declinations and lower significance values at smaller declinations are obtained in the analysis. This impression is supported by the one-dimensional significance distribution shown in Fig. 6.7(b) which has an RMS value of 1.22. The effect is also apparent when using a different background estimation method such as e.g. the Template background model. Systematic tests have shown that this gradient is neither a selection effect as resulting from the γ/hadron separation nor caused by a problem in the reconstruction or data analysis chain. This points to the fact that the gradient visible in the sky image is caused by a difference of the total number of events in certain regions of the sky. There are two possibilities, how a varying trigger rate over the covered f.o.v. of the camera can be generated. First of all, a varying zenith angle over the f.o.v. of the camera results in a trigger threshold which slightly varies across the camera. Hence, the number of events, projected onto the sky also depends on the reconstructed position of the event. This zenith-angle-dependent gradient

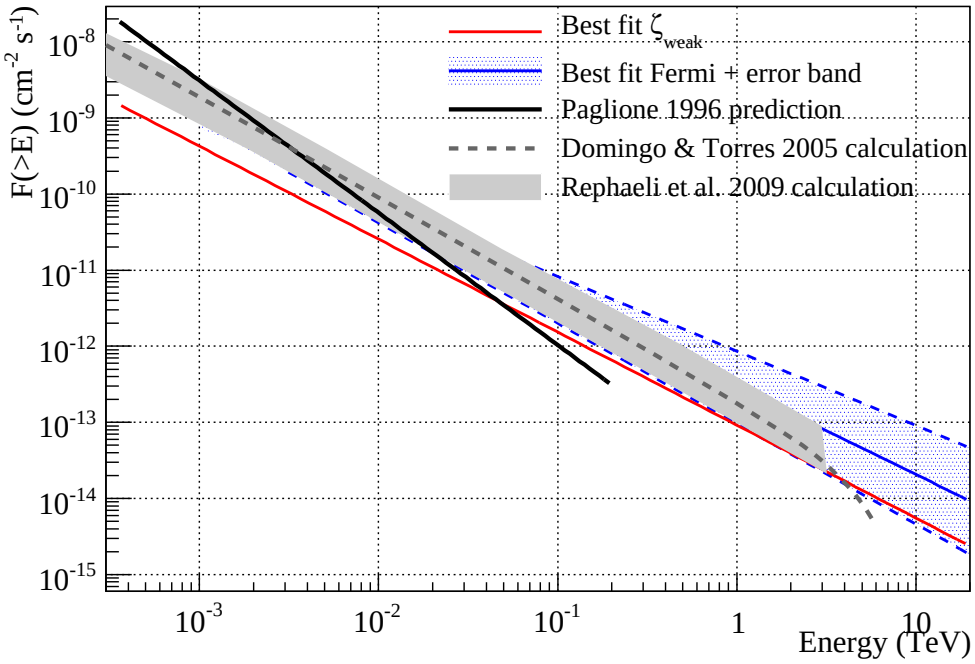

Figure 6.6: Integral flux of NGC 253 as obtained with ζ_{weak} cuts in comparison with model predictions by Paglione et al. (1996), Domingo-Santamaría & Torres (2005) and Rephaeli et al. (2010). Also shown is the best fit to the Fermi spectrum along with 1σ error band.

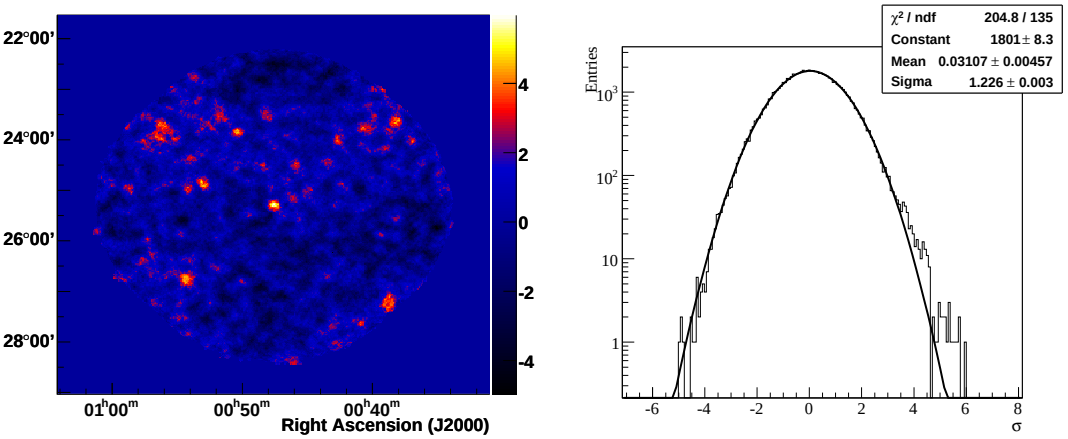

(a) (b)

Figure 6.7: (a) Significance map of the 6°×6° f.o.v. around NGC 253. (b) One-dimensional distribution of significance over the NGC 253 f.o.v.. Note that excluding the source region from the distribution does not significantly change the mean or width of the distribution.

is corrected in the Standard Analysis chain and is not the reason for the gradient visible in

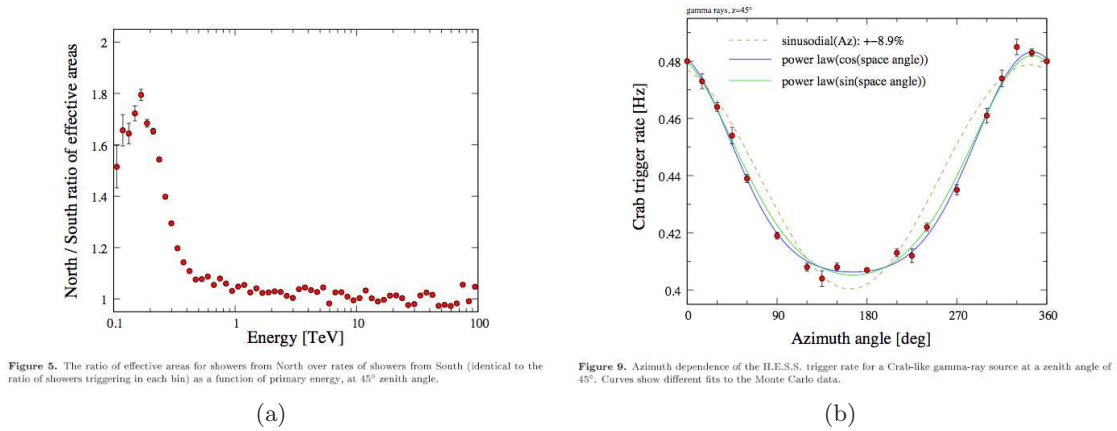

Figure 5. The ratio of effective areas for showers from North over rates of showers from South (identical to the ratio of showers triggering in each bin) as a function of primary energy, at 45° zenith angle.

Figure 9. Azimuth dependence of the H.E.S.S. trigger rate for a Crab-like gamma-ray source at a zenith angle of 45°. Curves show different fits to the Monte Carlo data.

(a) (b)

Figure 6.8: (a) Ratio of effective areas of Monte Carlo γ-ray events originating from northern and southern direction at 45° zenith angle as a function of reconstructed shower energy. (b) Azimuth dependence of trigger rate for Monte Carlo γ-ray showers at 45° zenith angle Figures taken from Bernlöhr (2005).

the NGC 253 f.o.v.. In further tests also potential hardware problems e.g. of the cameras as well as bright stars in the NGC 253 f.o.v. could be excluded as responsible for the gradient. The corresponding significance distributions showed no indication for any change in mean or width when excluding bright stars in the f.o.v. or excluding observations, where cameras were affected by e.g. missing drawers. Bernlöhr (2005) investigated, how the geomagnetic field of the Earth affects the shower development and the trigger rate as a function of the pointing direction of the telescopes. In the following, it will be shown that the Earths geomagnetic field could indeed affect the background subtraction in the NGC 253 data.

If the major axis of a shower is e.g. perpendicular to B_{earth}, $e^+ - e^-$ pairs are bent to opposite sites. The Čerenkov light of this shower is spread over a slightly larger area on ground and hence such kind of events have slightly larger energy thresholds. Fig. 6.8(a) shows the ratio of trigger rate between northwards oriented and southwards oriented Monte Carlo γ-ray showers at 45° zenith angle over reconstructed energy. Especially at low energies – up to 0.6 TeV – the difference is considerably large. In order to test the geomagnetic field hypothesis, the NGC 253 data has been split into sub sets of events with reconstructed energies below and above 0.6 TeV. Indeed, the resulting sky images have significance distributions which have a width of 1.22 and 1.02 for the low- and high-energy band, respectively.

To further investigate a possible Earth magnetic field effect, the whole NGC 253 data set has been split by the different pointing positions and analysed separately. The resulting signal and background statistics are compared in Table 6.3. Whereas the RA wobbles in positive and negative direction yield a similar number of excess events, the different Dec wobbles clearly show a difference in total number of excess events. The Altitude distribution of event directions, depicted in Fig. 6.9, shows that events predominantly arrived from Western direction between $90° - 130°$ and from Eastern direction between $230° - 280°$. Fig. 6.8(b) exemplarily depicts the trigger rate as a function of azimuth angle for Monte Carlo γ-ray events at 45° zenith angle. The absolute difference in trigger rate

Pointing	N_{On}	$\alpha \cdot N_{Off}$	Excess	Significance
			σ	
RA +	982	909	73 ± 33	2.3
RA -	891	825	62 ± 31	2.0
Dec +	926	925	1 ± 32	0.0
Dec -	1124	986	138 ± 35	4.1

Table 6.3: Number of γ-ray-like and background events as well as significance and γ-ray excess for ζ_{std} split by pointing position. The *Reflected* background method has been applied to estimate the background in the signal region.

is around $(1.5 - 2)\%$ for Western events and $\sim 3\%$ for Eastern events in the mentioned azimuth ranges. For comparison, Fig. 6.10 shows the mean azimuth angle of γ-ray like events as a function of sky position as obtained in the NGC 253 observations. Clearly, events with smaller azimuth angles have in general a larger declination. That implies that on average more events will trigger at larger declinations. The situation for Eastern events is different (Fig. 6.11). Here, events with larger azimuth angles have on average a larger declination – again, events preferably trigger at larger declinations. So, the difference in trigger rate as suggested by the simulations would not cancel out between Eastern and Western observations but would be amplified to $(4.5 - 5)\%$. Hence, for observations performed at positive declinations, the background at the NGC 253 position is presumably overestimated since Off-regions with higher rates are used for background estimation. On the other hand, observations performed at negative declinations would result in an underestimated background at the NGC 253 position due to background subtraction from Off-regions with lower rates. As one would expect, observations at positive and negative RA are not affected since the geomagnetic field effect would cancel out.

Indeed, changing the background level by 5% in the positive and negative declination pointings would result in a corrected excess which would match the excess as obtained from the RA pointings. These investigations show that the geomagnetic field could indeed affect the background estimation for different observation positions at the NGC 253 position. Moreover, as shown before, for energies above 0.6 TeV the observed gradient in the f.o.v. is no longer apparent, as also suggested by the studies done by Bernlöhr (2005). A power-law fit to the spectrum above an energy of 0.6 TeV results in an index of $\Gamma = 2.34 \pm 0.2$ and a normalisation at 1 TeV of $N_0 = (1.27 \pm 0.29_{\mathrm{stat}}) \times 10^{-13}\,\mathrm{TeV}^{-1}\,\mathrm{cm}^{-2}\,\mathrm{s}^{-1}$. These fit results are within 1σ compatible with the results found in Section 6.2 and suggest that the reconstruction of the NGC 253 spectrum is not significantly affected by the geomagnetic field.

6.4 Interpretation

In several aspects, the detection of HE/VHE γ-ray emission from a SB galaxy such as NGC 253 is interesting. So far, only AGN – which are driven by a supermassive black hole in the centre of their host galaxy – have been detected in VHE γ rays. NGC 253 is the

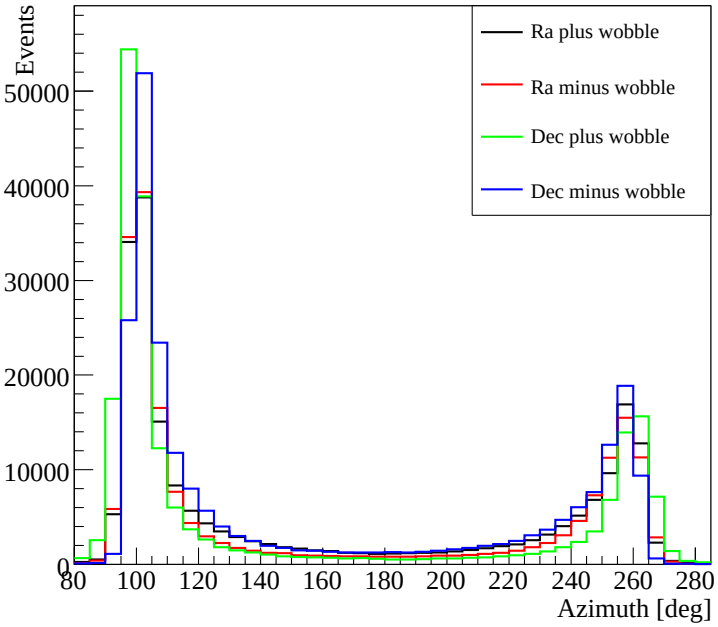

Figure 6.9: Azimuth distribution of events, 90° denotes west, 270° east.

first external galaxy seen in VHE γ rays[2], which produces its own population of CRs in Starburst activity. The H.E.S.S. measurements for the first time allow to derive properties of the CR population such as the particle- and energy density as well as CR transport in such an environment and to relate these to the CR properties measured in the solar system and other places in our own Galaxy.

First of all, the detection of VHE γ-ray emission from the SB nucleus implies a very high density of CRs in this region. A comparison of the γ-ray flux from the central region of the Milky Way and of NGC 253 allows to quantitatively estimate the CR density in the SB region. The CR density in the SB nucleus can be estimated using the VHE γ-ray flux measured from NGC 253 and the Galactic Centre ridge, the corresponding target material densities and their distances as:

$$E_{CR,253} = \left(\frac{F_{\gamma,253}}{F_{\gamma,GC}}\right)\left(\frac{d_{253}}{d_{GC}}\right)^2\left(\frac{\rho_{253}}{\rho_{GC}}\right)^{-1} E_{CR,GC} \tag{6.2}$$

Assuming a cylinder of 100 pc radius and 60 pc height and a mass of $1.7 \times 10^7\ M_\odot$ as used in Aharonian et al. (2006d), the density inside the central region of the Milky Way is $\rho_{GC} \approx 700\ \mathrm{cm}^{-3}$. The integral flux of the diffuse emission above an energy of 245 GeV is then $2.4 \times 10^{-11}\ \mathrm{cm}^{-2}\ \mathrm{s}^{-1}$ (Aharonian et al. 2006d). Using a distance to the GC of 8.5 kpc and the measured integral flux of NGC 253, the density of CRs with energy

[2] However, HE γ-ray emission has been detected from the Milky Way satellite galaxy, the LMC, by EGRET (Sreekumar et al. 1992) and later by Fermi (Knödlseder 2009). At the same time of the H.E.S.S. publication, also the VERITAS collaboration reported on the detection of VHE γ-ray emission from a SB galaxy, namely M 82, the northern twin of NGC 253 (VERITAS Collaboration et al. 2009).

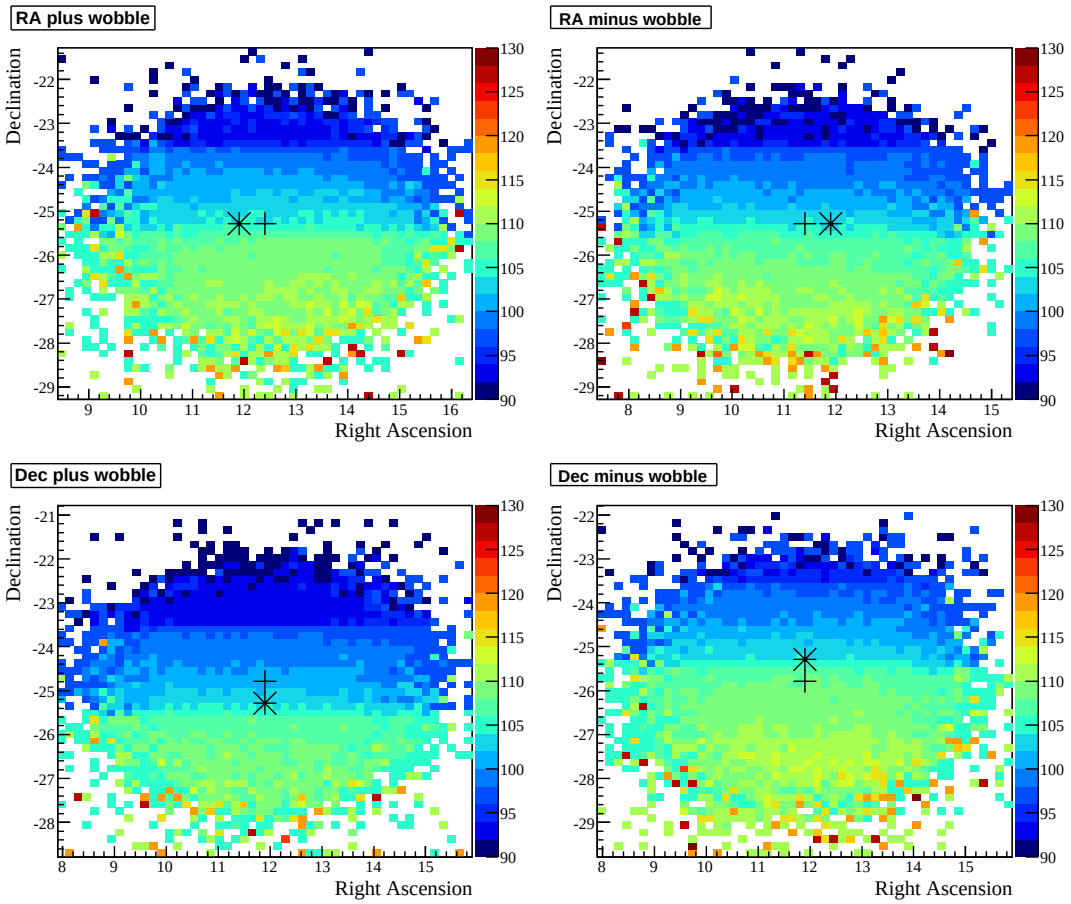

Figure 6.10: Mean azimuth angle of events coming from the Western direction, projected on RA-Dec coordinates. Events with smaller azimuth angles predominantly originate from larger declinations. The black cross denotes the pointing position relative to the NGC 253 position (black star). According to the *Reflected* background model, the background is subtracted from circular regions at same distances between telescope pointing position and NGC 253 position.

$E > 245/0.17 = 1440$ GeV in the central region of NGC 253 amounts to:

$$E_{CR,253}(> 1.44 \text{ TeV}) \approx 4.9 \times 10^{-12} \text{ cm}^{-3} \approx 1400 \; E_{CR,GC} \; . \tag{6.3}$$

This density is a factor of 2000 larger compared to the local CR density above the same energy and a factor of 1400 larger compared to the CR density in the central region of our Galaxy. Multiplying the CR density with the CR energy of 1.44 TeV results in a rough estimate of the energy density in CRs of 7.1 eV cm^{-3}, a value larger than the energy density in CRs in the solar neighbourhood. Notably, the solar system energy density is dominated by GeV particles, whereas the derived estimate is for protons with energies $E > 1.44$ TeV.

As shown in Section 3.3, the population of CRs apparent in the SB nucleus in NGC 253 not only encounters energy loss due to hadronic interactions with the ambient medium, but also due to convection and diffusion of particles. Extrapolating the estimated γ-ray flux in the calorimetric limit as calculated in Eq. 3.14 down to 245 GeV results in an

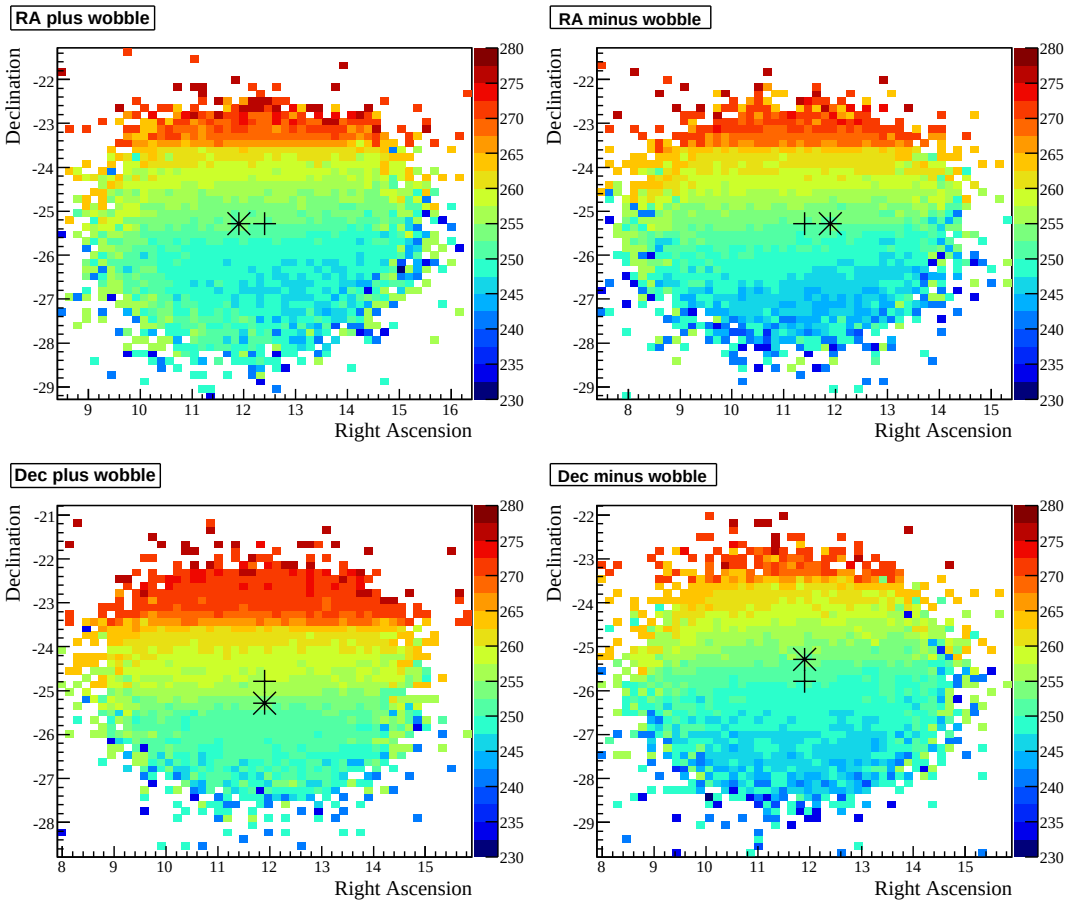

Figure 6.11: Mean azimuth angle of events coming from the Eastern direction, projected on RA-Dec coordinates. Events with larger azimuth angles predominantly originate from larger declinations. The black cross denotes the pointing position relative to the NGC 253 position (black star). The background is estimated using the *Reflected* background method.

$F_\gamma \approx 10^{-11}$ cm^{-2} s^{-1}, a factor of ≈ 20 higher as expected in a fully calorimetric system. Hence, the SB region is just to 5% calorimetric. Whereas convection does not change the index of the parent CR population, diffusion does change the spectral index. With the knowledge of the spectral index of the injected particles, the magnitude of diffusive losses could be read off in the difference to the measured VHE γ-ray spectral index. Assuming an injection spectrum of CRs which falls off as $dN_{CR}/dE \propto E^{-2.1}$, the difference in spectral index between measured γ-ray index and injection spectrum can be attributed to energy-dependent diffusion. The uncertainty of 0.13 on the measured index of 2.24 does not allow to disentangle the contribution of energy loss due to convection and diffusion. However, it is clear, that a major fraction of the CR energy is dissipated in convection and diffusion. Therefore, SB galaxies are believed to populate the IGM with CRs.

7 Summary and Conclusions

In this work, an advanced γ/hadron separation technique – the BDT method – was introduced and applied to H.E.S.S. data obtained in observations of regions of massive star formation. From small to large scales, the analyses comprise the prominent colliding wind binary system η Carinae, the most massive stellar cluster in the Milky Way, Westerlund 1 and the Starburst galaxy NGC 253. An upper limit on the γ-ray flux from η Carinae was derived. Furthermore, extended VHE γ-ray emission from the vicinity of Westerlund 1 has been reported. Finally, NGC 253 as representative for Starburst galaxies, was established as a new VHE γ-ray source (class).

Ground-based IACTs achieve a five order of magnitude increased detection area compared to satellite-based instruments at the expense of a huge hadronic background component. The capability to separate these CRs from VHE γ rays directly determines the sensitivity of IACT systems like H.E.S.S.. In this work, the multivariate BDT method has been trained, tested and evaluated with Monte Carlo γ-ray simulations and real background data by means of parameters which describe the shape of the initiated EAS. The BDT approach leads to a significantly increased separation power compared to the H.E.S.S. Standard Analysis. Especially in the case of weak, steep-spectrum sources, the ζ_{std} cuts have proven to achieve a 20% gain in sensitivity (or 45% in observation time). The zenith- and energy-dependent γ/hadron separation has proven to give a stable performance improvement for a wide range of observational conditions. Moreover, the inclusion of additional parameters with separation potential, as e.g. obtained in the Model3D or Model++ analysis, in the training process can further improve the BDT performance. Systematic studies demonstrated that an MVA approach such as the BDT is well suited for the analysis of γ-ray data. Future projects like H.E.S.S. II, MAGIC II, CTA and AGIS will extent the accessible energy range of IACTs as the reachable sensitivity increases. Multivariate methods will most likely play a major role for the analysis and particularly for the γ/hadron separation, since the majority of the events will be recorded below 100 GeV, where γ/hadron separation gets increasingly difficult. Parameters such as X_{max} demonstrated the ability to improve the performance of IACTs, especially for the separation at low energies.

In the second part of this work the developed BDT method was utilised in the analysis of γ-ray data. Colliding wind binary systems such as η Carinae are predicted to emit γ rays at a level detectable with the Fermi satellite and up to energies which are right at the edge of the energy threshold of IACTs such as H.E.S.S.. The data analysis of observations with 9 hours of live time in the η Carinae region resulted in a 2σ flux UL of 7×10^{-13} ph cm^{-2} s^{-1} above an energy of 0.52 TeV at the position of η Carinae and a hint of extended VHE γ-ray emission in a circular region of 0.4° radius. Future H.E.S.S. observations will help to shed light on the nature of the point-like unidentified Fermi source coincident with η Carinae and prove whether or not particle acceleration to TeV energies is occurring in this system. The planned observations could also confirm the extended

emission seen from the surrounding Carina nebula, one of the most massive star formation regions in the Milky Way. Additionally, an alternative HE/VHE γ-ray emission scenario for the presence of HE γ-ray emission during periastron passage of η Carinae (where no signal is expected due to a collapse of the CWR) has been presented for the first time. Namely, particle acceleration in the fast expanding blast wave of the historical 1843's outburst, which mimics a low-energy SNR shell. This model could be tested by means of high-resolution radio observations and prove whether or not, a population of high-energy electrons is apparent in the outer ejecta.

Young massive stellar clusters are believed to significantly contribute to the acceleration of GCRs via diffusive and turbulent shock acceleration. The analysis of data with 34 hours of live time of the most massive stellar cluster in the Milky Way, Westerlund 1, revealed $2^\circ-$scale VHE γ-ray emission from the vicinity of the cluster. Spectral and morphological analyses showed no indication for multiple sources as responsible for the emission. Moreover, no change in spectral index across the whole emission was found, which would be indicative for energy-dependent particle transport and/or energy loss processes in a single source. Point-like VHE γ-ray emission is expected if the numerous CWB systems in Wd 1 effectively accelerate particles in their colliding winds. However, a large part of the detected emission is of diffuse nature and just a minor fraction may be associated to emission originating from the cluster itself. The stellar wind and SN activity of Wd 1 presumably led to the formation of a superbubble which is now merging with the surrounding interstellar medium. Some correlation between high-density regions in HI at the estimated cluster distance and VHE γ-ray emission is apparent. This correlation is suggestive for a hadronic scenario, where protons could be accelerated in and around Wd 1 and interact with the ambient medium producing π^0s and subsequently VHE γ rays. However, parts of the observed emission are not correlated with regions of high gas density. The search for astronomical objects which are believed to accelerate particles to very high energies such as e.g. SNRs or PWNe revealed a bright and extended X-ray source, identified in the XMM-Newton Slew Survey. Future X-ray observations could confirm a possible PWN and help to disentangle a potential contribution to the overall VHE γ-ray emission.

The central region of Starburst galaxies can be seen as Galactic scale twins or scaled-up version of superbubbles blown by a stellar cluster. SB galaxies undergo an evolutionary phase of enhanced star formation and are characterised by an highly increased supernova rate in a very localised region compared to galaxies such as the Milky Way. Starburst regions are promising sites for particle acceleration and provide at the same time a high density of target material for *pp* interaction and the production of π^0-decay γ rays. The archetypal SB galaxy NGC 253 has been observed with H.E.S.S. for a very long exposure time of 241 hours. A total of ~ 150 hours of observations passed standard quality criteria and were analysed with the BDT method. The analysis presented in this work resulted in the detection of a significant γ-ray excess from the central region of NGC 253. The signal is stable over a four year time period, of point-like nature and has an integral flux of $\sim 0.2\%$ of the Crab nebula flux above the threshold energy of 245 GeV. This is the by far weakest VHE γ-ray signal ever detected by any IACT. The differential energy spectrum is well described by a power law with spectral index $\Gamma = 2.24 \pm 0.14$ and norm $N_0 = 1.12 \pm 0.19$ – compatible within 1σ with the extrapolated Fermi flux. The flux level as measured by H.E.S.S. is a factor of 20 lower as expected in the calorimetric limit, where energy loss due to CR escape in the Galactic wind and diffusion of particles can be neglected.

Therefore, NGC 253 in particular and SB galaxies in general are expected to populate the inter-galactic medium with CRs.

In summary, even though the detection of a CWB in VHE γ rays is still pending, analysis results presented in this work strongly hint to particle acceleration in a massive stellar cluster and hadronic interactions in its vicinity. Most importantly, application of the advanced γ/hadron separation method led to the discovery of the first SB galaxy in VHE γ-ray astronomy and demonstrated the potential of elaborated γ/hadron discrimination methods for current systems like H.E.S.S. as well as for mid- and long-term future projects such as CTA.

A Comparison between simulations and data, HESS J1745–290 – Dark Matter data set

In the following, the comparison between the data set comprised of a sub set of the data used in Aharonian et al. (2006b) with a total live time of 11.4 hours (as used in Ohm et al. 2009b) and Monte Carlo γ-ray simulations is shown. Events with zenith angles of $15^\circ \leq \theta \leq 25^\circ$, reconstructed energies of $(0.2 - 10.0)$ TeV and a mean offset of 1° are compared to Monte Carlo γ-ray simulations at a fixed zenith- and offset angle of 20° and 1°, respectively. Only events in the same energy regime which follow the same spectral energy distribution as measured in Aharonian et al. (2006b) ($\Gamma = 2.21$) have been considered.

Figure A.1 illustrates the ζ distribution of events originating from the assumed source region and from seven circular background control regions following the Reflected background model. The VHE γ-ray excess is calculated as $N_\gamma = N_{On} - \alpha \cdot N_{Off}$.

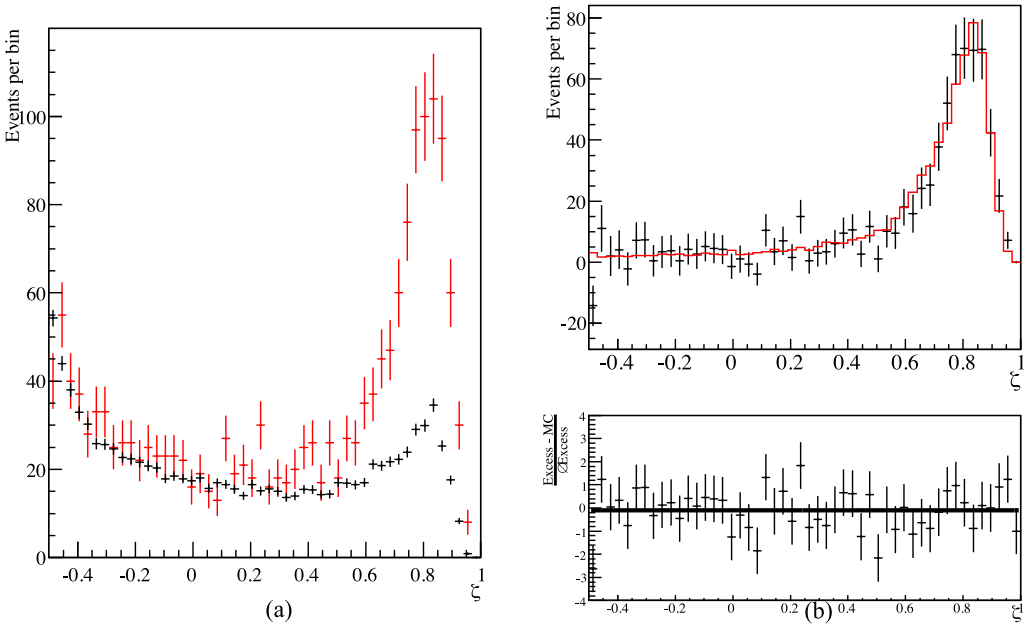

Figure A.1: (a) ζ distribution for events from the On-Region (red) and events from the Off-Regions (black), weighted by α, from HESS J1745–290 observations. (b) Comparison between Monte Carlo γ-ray simulations (red curve) and VHE γ-ray excess, normalised to the number of events in the range ($0 \leq \zeta \leq 1$). Also shown are the residua between the two distributions and the result of a fit of a constant, which is compatible with 0 residuum within the statistical errors and has a χ^2/ndf of 40/49 (Figure taken from Ohm et al. 2009b).

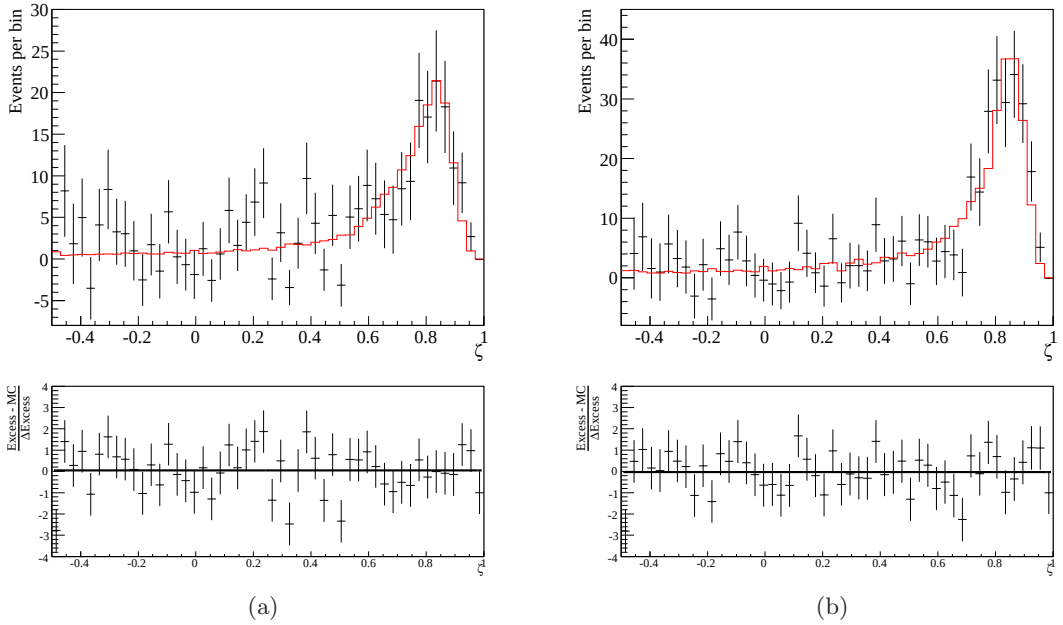

Figure A.2: Comparison of ζ distributions for Monte Carlo γ-ray simulations and VHE γ-ray excess (a) for events with a multiplicity of 2 and (b) for events with reconstructed energies 0.2 TeV $\leq$ E $\leq$ 0.4 TeV. The lower panel again shows their residua and the result of a fit of a constant. Both fits are compatible with 0 residuum within the statistical errors and have a χ^2/ndf of 57/49 and 43/49, respectively (Figure taken from Ohm et al. 2009b).

B Starburst99 simulation of Westerlund 1

The following options can be specified as input parameters for the Starburst99 simulations, available at:

`http://www.stsci.edu/science/starburst99/`

MODEL DESIGNATION: [NAME]
Westerlund1

CONTINUOUS STAR FORMATION (> 0) OR FIXED MASS (≤ 0): [ISF]
-1

TOTAL STELLAR MASS [10e6 SOLAR MASSES] IF 'FIXED MASS' IS CHOSEN: [TOMA]
0.1

SFR [SOLAR MASSES PER YEAR] IF 'CONT. SF' IS CHOSEN: [SFR]
1.000

NUMBER OF INTERVALS FOR THE IMF (KROUPA=2): [NINTERV]
2

IMF EXPONENTS (KROUPA=1.3,2.3): [XPONENT]
1.300,2.300

MASS BOUNDARIES FOR IMF (KROUPA=0.1,0.5,100) [SOLAR MASSES]: [XMASLIM]
0.100,0.500,100.000

SUPERNOVA CUT-OFF MASS [SOLAR MASSES]: [SNCUT]
8.000

BLACK HOLE CUT-OFF MASS [SOLAR MASSES]: [BHCUT]
120.000

METALLICITY + TRACKS: [IZ]
GENEVA STD: 11=0.001; 12=0.004; 13=0.008; 14=0.020; 15=0.040
GENEVA HIGH:21=0.001; 22=0.004; 23=0.008; 24=0.020; 25=0.040
PADOVA STD: 31=0.0004; 32=0.004; 33=0.008; 34=0.020; 35=0.050
PADOVA AGB: 41=0.0004; 42=0.004; 43=0.008; 44=0.020; 45=0.050
44

WIND MODEL (0: MAEDER; 1: EMP.; 2: THEOR.; 3: ELSON): [IWIND]
0

INITIAL TIME [1.E6 YEARS]: [TIME1]
0.010

TIME SCALE: LINEAR (=0) OR LOGARITHMIC (=1) [JTIME]
0

TIME STEP [1.e6 YEARS] (ONLY USED IF JTIME=0): [TBIV]
0.100

NUMBER OF STEPS (ONLY USED IF JTIME=1): [ITBIV]
1000

LAST GRID POINT [1.e6 YEARS]: [TMAX]
100.000

SMALL (=0) OR LARGE (=1) MASS GRID;
ISOCHRONE ON LARGE GRID (=2) OR FULL ISOCHRONE (=3): [JMG]
3

LMIN, LMAX (ALL=0): [LMIN,LMAX]
0

TIME STEP FOR PRINTING OUT THE SYNTHETIC SPECTRA [1.e6YR]: [TDEL]
2.000

ATMOSPHERE: 1=PLA, 2=LEJ, 3=LEJ+SCH, 4=LEJ+SMI, 5=PAU+SMI: [IATMOS]
5

METALLICITY OF THE HIGH RESOLUTION MODELS [ILIB]
(1=0.001, 2= 0.008, 3=0.020, 4=0.040):
3

METALLICITY OF THE UV LINE SPECTRUM: (1=SOLAR, 2=LMC/SMC) [ILINE]
1

RSG FEATURE: MICROTURB. VEL (1-6), SOL/NON-SOL ABUND (0,1) [IVT,IRSG]
3,0

OUTPUT FILES (NO<0, YES≥ 0) [IO1,...]
1,1,1,1,1,1,1,1,1,1,1,1,1,1,-1

Bibliography

Abazov, V. M., Abbott, B., Abolins, M., et al. 2008, Phys. Rev. D, 78, 012005

Abdo, A. A., Ackermann, M., Ajello, M., et al. 2009a, Science, 325, 840

Abdo, A. A., Ackermann, M., Ajello, M., et al. 2010, Fermi/Large Area Telescope 1 year catalog, http:http://fermi.gsfc.nasa.gov/ssc/data/access/lat/1yr_catalog/1FGL_catalog_v2.pdf

Abdo, A. A., Ackermann, M., Ajello, M., et al. 2009b, ApJS, 183, 46

Acciari, V. A., Aliu, E., Arlen, T., et al. 2009, ApJ, 698, L133

Acero, F., Aharonian, F., Akhperjanian, A. G., et al. 2009, Science, 326, 1080

Aharonian, F., Akhperjanian, A., Barrio, J., et al. 2001, A&A, 370, 112

Aharonian, F., Akhperjanian, A., Beilicke, M., et al. 2004a, ApJ, 614, 897

Aharonian, F., Akhperjanian, A. G., Anton, G., et al. 2009a, A&A, 503, 817

Aharonian, F., Akhperjanian, A. G., Aye, K., et al. 2005a, A&A, 442, 1

Aharonian, F., Akhperjanian, A. G., Aye, K., et al. 2005b, A&A, 430, 865

Aharonian, F., Akhperjanian, A. G., Aye, K., et al. 2004b, Astroparticle Physics, 22, 109

Aharonian, F., Akhperjanian, A. G., Barres de Almeida, U., et al. 2008a, Physical Review Letters, 101, 261104

Aharonian, F., Akhperjanian, A. G., Bazer-Bachi, A. R., et al. 2008b, A&A, 481, 401

Aharonian, F., Akhperjanian, A. G., Bazer-Bachi, A. R., et al. 2006b, Physical Review Letters, 97, 221102

Aharonian, F., Akhperjanian, A. G., Bazer-Bachi, A. R., et al. 2006c, A&A, 448, L43

Aharonian, F., Akhperjanian, A. G., Bazer-Bachi, A. R., et al. 2006a, A&A, 457, 899

Aharonian, F., Akhperjanian, A. G., Bazer-Bachi, A. R., et al. 2005c, A&A, 442, 177

Aharonian, F., Akhperjanian, A. G., Bazer-Bachi, A. R., et al. 2006d, Nature, 439, 695

Aharonian, F., Akhperjanian, A. G., Bazer-Bachi, A. R., et al. 2006e, ApJ, 636, 777

Aharonian, F., Akhperjanian, A. G., Bazer-Bachi, A. R., et al. 2007a, A&A, 467, 1075

Aharonian, F., Akhperjanian, A. G., Bazer-Bachi, A. R., et al. 2007b, ApJ, 661, 236

Aharonian, F., Akhperjanian, A. G., Bazer-Bachi, A. R., et al. 2006f, A&A, 460, 743

Aharonian, F., Akhperjanian, A. G., Bazer-Bachi, A. R., et al. 2006g, A&A, 460, 365

Aharonian, F., Akhperjanian, A. G., de Almeida, U. B., et al. 2009b, ApJ, 692, 1500

Aharonian, F. A. 2004, Very high energy cosmic gamma radiation : a crucial window on the extreme Universe (World Scientific Publishing Company; 1st edition (April 30, 2003))

Aharonian, F. A., Akhperjanian, A. G., Aye, K., et al. 2004c, Nature, 432, 75

Aharonian, F. A., Akhperjanian, A. G., Bazer-Bachi, A. R., et al. 2007c, A&A, 469, L1

Albert, J., Aliu, E., Anderhub, H., et al. 2008, Nuclear Instruments and Methods in Physics Research A, 588, 424

Albert, J., Aliu, E., Anderhub, H., et al. 2007a, A&A, 474, 937

Albert, J., Aliu, E., Anderhub, H., et al. 2007b, ApJ, 664, L87

Aliu, E., Anderhub, H., Antonelli, L. A., et al. 2008, ApJ, 685, L71

Anchordoqui, L. A., Romero, G. E., & Combi, J. A. 1999, Phys. Rev. D, 60, 103001

Axford, W. I., Leer, E., & Skadron, G. 1977, in International Cosmic Ray Conference, Vol. 11, International Cosmic Ray Conference, 132–+

Bailey, S., Aragon, C., Romano, R., et al. 2007, ApJ, 665, 1246

Bamba, A., Ueno, M., Nakajima, H., & Koyama, K. 2004, ApJ, 602, 257

Barnard, R., Greening, L. S., & Kolb, U. 2008, MNRAS, 388, 849

Bednarek, W. 2005, MNRAS, 363, L46

Bell, A. R. 1978, MNRAS, 182, 443

Benaglia, P. & Romero, G. E. 2003, A&A, 399, 1121

Berge, D. 2006, PhD thesis, Ruperto-Carola University of Heidelberg

Berge, D., Funk, S., & Hinton, J. 2007, A&A, 466, 1219

Bernlöhr, K. 2000, Monte Carlo images of air showers, `http://www.mpi-hd.mpg.de/hfm/~bernlohr/HESS/`

Bernlöhr, K. 2005, Geomagnetic effects on showers relevant for the H.E.S.S. experiment, H.E.S.S. internal note

Bernlöhr, K. 2010, private communications

Bird, A. J., Malizia, A., Bazzano, A., et al. 2007, ApJS, 170, 175

Blandford, R. D. & Ostriker, J. P. 1978, ApJ, 221, L29

Bock, R. K., Chilingarian, A., Gaug, M., et al. 2004, Nuclear Instruments and Methods in Physics Research A, 516, 511

Bolz, O. 2004, PhD thesis, Ruperto-Carola University of Heidelberg

Brandner, W., Clark, J. S., Stolte, A., et al. 2008, A&A, 478, 137

Brandner, W., Clark, S., & Waters, R. 2005, in Protostars and Planets V, 8344–+

Breiman, L. 2001, Mach. Learn., 45, 5

Breiman, L., Friedman, J. H., Olshen, R. A., & Stone, C. J. 1984, Classification and Regression Trees (Chapman & Hall/CRC)

Bugayov, V. V., Plyasheshnikov, A. V., Vassiliev, V. V., & Weekes, T. C. 2002, Astroparticle Physics, 17, 41

Bykov, A. M. 2001, Space Science Reviews, 99, 317

Celik, O. 2008, in International Cosmic Ray Conference, Vol. 2, International Cosmic Ray Conference, 847–850

Chen, W. & White, R. L. 1991, ApJ, 381, L63

Clark, J. S. & Negueruela, I. 2002, A&A, 396, L25

Clark, J. S. & Negueruela, I. 2004, A&A, 413, L15

Clark, J. S., Negueruela, I., Crowther, P. A., & Goodwin, S. P. 2005, A&A, 434, 949

Cooper, R. L., Guerrero, M. A., Chu, Y., Chen, C., & Dunne, B. C. 2004, ApJ, 605, 751

Corcoran, M. F. 2010, `http://asd.gsfc.nasa.gov/Michael.Corcoran/eta_car/etacar_rxte_lightcurve/index.html`

Corcoran, M. F., Ishibashi, K., Swank, J. H., & Petre, R. 2001, ApJ, 547, 1034

Cordes, J., Lazio, T., Chatterjee, S., Arzoumanian, Z., & Chernoff, D. 2002, in COSPAR, Plenary Meeting, Vol. 34, 34th COSPAR Scientific Assembly

Crowther, P. A., Hadfield, L. J., Clark, J. S., Negueruela, I., & Vacca, W. D. 2006, MNRAS, 372, 1407

Damineli, A. 1996, ApJ, 460, L49+

Damineli, A., Kaufer, A., Wolf, B., et al. 2000, ApJ, 528, L101

Davidge, T. J., Le Fevre, O., & Clark, C. C. 1991, ApJ, 370, 559

Davies, J. & Cotton, E. 1957, Journal of Solar Energy Science and Engineering

De Becker, M. 2007, A&A Rev., 14, 171

de Naurois, M. & Rolland, L. 2009, Astroparticle Physics, 32, 231

Domingo-Santamaría, E. & Torres, D. F. 2005, A&A, 444, 403

Dorfi, E. A. & Völk, H. J. 1996, A&A, 307, 715

Dwarkadas, V. V. 2008, Physica Scripta Volume T, 132, 014024

Egberts, K. 2005, Das Spektrum der kosmischen Elektronen gemessen mit H.E.S.S., Diploma thesis

Egberts, K. 2009, PhD thesis, Ruperto-Carola University of Heidelberg

Eichler, D. & Usov, V. 1993, ApJ, 402, 271

Engelbracht, C. W., Rieke, M. J., Rieke, G. H., Kelly, D. M., & Achtermann, J. M. 1998, ApJ, 505, 639

Ergin, T. & VERITAS Collaboration. 2008, in AAS/High Energy Astrophysics Division, Vol. 10, AAS/High Energy Astrophysics Division, #31.08–+

Falceta-Gonçalves, D., Jatenco-Pereira, V., & Abraham, Z. 2005, MNRAS, 357, 895

Fegan, S., Buckley, J. H., Bugaev, S., et al. 2008, in AAS/High Energy Astrophysics Division, Vol. 10, AAS/High Energy Astrophysics Division, #28.06–+

Feinstein, A. 1995, in Revista Mexicana de Astronomia y Astrofisica, vol. 27, Vol. 2, Revista Mexicana de Astronomia y Astrofisica Conference Series, ed. V. Niemela, N. Morrell, & A. Feinstein, 57–+

Fermi, E. 1949, Physical Review, 75, 1169

Ferrand, G. & Marcowith, A. 2010, A&A, 510, A101+

Ferrière, K. M. 2001, Reviews of Modern Physics, 73, 1031

Fiasson, A., Dubois, F., Lamanna, G., Masbou, J., & Rosier-Lees, S. 2010, to be submitted to Astroparticle Physics

Fonseca, V. 1998, Ap&SS, 263, 377

Freund, Y. & Schapire, R. E. 1997, J. Comput. Syst. Sci., 55, 119

Gallant, Y. A. 2007, Ap&SS, 309, 197

Gies, D. R. 2008, in Astronomical Society of the Pacific Conference Series, Vol. 387, Massive Star Formation: Observations Confront Theory, ed. H. Beuther, H. Linz, & T. Henning, 93–+

Goetting, N. 2005, PhD thesis, Universität Hamburg

Green, D. A. 2009, Bulletin of the Astronomical Society of India, 37, 45

Hamaguchi, K., Petre, R., Matsumoto, H., et al. 2007, PASJ, 59, 151

Hartman, R. C., Bertsch, D. L., Bloom, S. D., et al. 1999, VizieR Online Data Catalog, 212, 30079

Heitler, W. 1954, Quantum theory of radiation (Dover Publications; 3 edition (April 1, 1984))

Hermann, G., Hofmann, W., Schweizer, T., & et al. 2008, in International Cosmic Ray Conference, Vol. 3, International Cosmic Ray Conference, 1313–1316

Higdon, J. C. & Lingenfelter, R. E. 2005, ApJ, 628, 738

Hillas, A. M. 1985, in International Cosmic Ray Conference, ed. F. C. Jones, Vol. 3, 445–448

Hillier, D. J., Davidson, K., Ishibashi, K., & Gull, T. 2001, ApJ, 553, 837

Hinton, J. A. 2004, New Astronomy Review, 48, 331

Hinton, J. A. & Hofmann, W. 2009, ARA&A, 47, 523

Hoecker, A., Speckmayer, P., Stelzer, J., et al. 2007, ArXiv Physics e-prints

Hofmann, W., Jung, I., Konopelko, A., et al. 1999, Astroparticle Physics, 12, 135

Hoppe, S. 2008, PhD thesis, Ruperto-Carola University of Heidelberg

Horan, D. & Weekes, T. C. 2004, New Astronomy Review, 48, 527

Ishibashi, K., Gull, T. R., Davidson, K., et al. 2003, AJ, 125, 3222

Itoh, C., Enomoto, R., Yanagita, S., et al. 2002, A&A, 396, L1

Itoh, C., Enomoto, R., Yanagita, S., et al. 2007, A&A, 462, 67

Itoh, C., Enomoto, R., Yanagita, S., et al. 2003, A&A, 402, 443

Johnson, K. E. 2004, in Astronomical Society of the Pacific Conference Series, Vol. 322, The Formation and Evolution of Massive Young Star Clusters, ed. H. J. G. L. M. Lamers, L. J. Smith, & A. Nota, 339–+

Karachentsev, I. D., Grebel, E. K., Sharina, M. E., et al. 2003, A&A, 404, 93

Knödlseder, J. 2009, ArXiv e-prints

Kothes, R. & Dougherty, S. M. 2007, A&A, 468, 993

Krymskii, G. F. 1977, Akademiia Nauk SSSR Doklady, 234, 1306

Kubo, H., Asahara, A., Bicknell, G. V., et al. 2004, New Astronomy Review, 48, 323

Lagage, P. O. & Cesarsky, C. J. 1983, A&A, 125, 249

Law, C. & Yusef-Zadeh, F. 2004, ApJ, 611, 858

Lehnert, M. D. & Heckman, T. M. 1996, ApJ, 472, 546

Leitherer, C. 2010, `http://www.stsci.edu/science/starburst99/`

Lemoine-Goumard, M., Degrange, B., & Tluczykont, M. 2006, Astroparticle Physics, 25, 195

Leyder, J., Walter, R., & Rauw, G. 2008, A&A, 477, L29

Lorenz, E. 2004, New Astronomy Review, 48, 339

Luna, A., Mayya, Y. D., Carrasco, L., & Bronfman, L. 2010, ArXiv e-prints

Mac Low, M. & McCray, R. 1988, ApJ, 324, 776

MAGIC Collaboration. 2007, ArXiv Astrophysics e-prints arXiv:astro-ph/0702475

Maier, G. & Knapp, J. 2007, Astroparticle Physics, 28, 72

Manchester, R. N., Hobbs, G. B., Teoh, A., & Hobbs, M. 2005, AJ, 129, 1993

McCarthy, P. J., van Breugel, W., & Heckman, T. 1987, AJ, 93, 264

McClure-Griffiths, N. M., Dickey, J. M., Gaensler, B. M., et al. 2005, ApJS, 158, 178

Melo, V. P., Pérez García, A. M., Acosta-Pulido, J. A., Muñoz-Tuñón, C., & Rodríguez Espinosa, J. M. 2002, ApJ, 574, 709

Meyer, M., Horns, D., & Zechlin, H.-S. 2010, Astronomy & Astrophysics, submitted

Moffat, A. F. J. & Corcoran, M. F. 2009, ApJ, 707, 693

Mohan, N. R., Goss, W. M., & Anantharamaiah, K. R. 2005, A&A, 432, 1

Montmerle, T. 1979, ApJ, 231, 95

Mücke, A. & Pohl, M. 2002, in Astronomical Society of the Pacific Conference Series, Vol. 260, Interacting Winds from Massive Stars, ed. A. F. J. Moffat & N. St-Louis, 355–+

Muno, M. P., Clark, J. S., Crowther, P. A., et al. 2006a, ApJ, 636, L41

Muno, M. P., Law, C., Clark, J. S., et al. 2006b, ApJ, 650, 203

Murphy, T., Mauch, T., Green, A., et al. 2007, VizieR Online Data Catalog, 8082, 0

Naumann-Godó, M., Beilicke, M., Hauser, D., Lemoine-Goumard, M., & de Naurois, M. 2008, in American Institute of Physics Conference Series, Vol. 1085, American Institute of Physics Conference Series, ed. F. A. Aharonian, W. Hofmann, & F. Rieger, 304–307

Naumann-Godó, M., Lemoine-Goumard, M., & Degrange, B. 2009, Astroparticle Physics, 31, 421

Nedbal, D. 2008, PhD thesis, Ruperto-Carola University of Heidelberg

Negueruela, I. & Clark, J. S. 2005, A&A, 436, 541

Negueruela, I., Smith, D. M., Reig, P., Chaty, S., & Torrejón, J. M. 2006, in ESA Special Publication, Vol. 604, The X-ray Universe 2005, ed. A. Wilson, 165–+

Nespoli, E., Fabregat, J., & Mennickent, R. E. 2008, A&A, 486, 911

Ohm, S. 2007, Algorithmen zur Gamma-Hadron-Separation mit den H.E.S.S.-Teleskopen, Diploma thesis

Ohm, S., Horns, D., Reimer, O., et al. 2009a, ArXiv e-prints

Ohm, S., van Eldik, C., & Egberts, K. 2009b, Astroparticle Physics, 31, 383

Paglione, T. A. D., Marscher, A. P., Jackson, J. M., & Bertsch, D. L. 1996, ApJ, 460, 295

Parizot, E., Marcowith, A., van der Swaluw, E., Bykov, A. M., & Tatischeff, V. 2004, A&A, 424, 747

Pence, W. D. 1980, ApJ, 239, 54

Pietsch, W., Roberts, T. P., Sako, M., et al. 2001, A&A, 365, L174

Pittard, J. M. 2009, MNRAS, 396, 1743

Pittard, J. M. & Corcoran, M. F. 2002, A&A, 383, 636

Pittard, J. M., Dougherty, S. M., Coker, R. F., O'Connor, E., & Bolingbroke, N. J. 2006, A&A, 446, 1001

Pittard, J. M., Stevens, I. R., Williams, P. M., et al. 2002, A&A, 388, 335

Pittori, C., Verrecchia, F., Chen, A. W., et al. 2009, A&A, 506, 1563

Reimer, A., Pohl, M., & Reimer, O. 2006, ApJ, 644, 1118

Rekola, R., Richer, M. G., McCall, M. L., et al. 2005, MNRAS, 361, 330

Rephaeli, Y., Arieli, Y., & Persic, M. 2010, MNRAS, 401, 473

Reynolds, A. P., Parmar, A. N., Hakala, P. J., et al. 1999, A&AS, 134, 287

Reynolds, S. P., Borkowski, K. J., Green, D. A., et al. 2008, ApJ, 680, L41

Ritz, S. M., Michelson, P. F., Meegan, C., Grindlay, J., & GLAST Mission Team. 2007, in Bulletin of the American Astronomical Society, Vol. 38, Bulletin of the American Astronomical Society, 909–+

Rowell, G. P. 2003, A&A, 410, 389

Saxton, R. D., Read, A. M., Esquej, P., et al. 2008, A&A, 480, 611

Seward, F. D., Butt, Y. M., Karovska, M., et al. 2001, ApJ, 553, 832

Skilton, J. L., Pandey-Pommier, M., Hinton, J. A., et al. 2009, MNRAS, 399, 317

Smith, N. 2006, MNRAS, 367, 763

Smith, N. 2008, Nature, 455, 201

Smith, N., Gehrz, R. D., Hinz, P. M., et al. 2003, AJ, 125, 1458

Sobczynska, D. 2007, Journal of Physics G Nuclear Physics, 34, 2279

Sreekumar, P., Bertsch, D. L., Dingus, B. L., et al. 1992, ApJ, 400, L67

Takahashi, H., Abdo, A. A., Ackermann, M., et al. 2009, `http://confluence.slac.stanford.edu/download/attachments/67503240/fermi2009_htakahashi.pdf?version=1`

Tang, S. & Wang, Q. D. 2005, ApJ, 628, 205

Tavani, M., Barbiellini, G., Argan, A., et al. 2009a, A&A, 502, 995

Tavani, M., Sabatini, S., Pian, E., et al. 2009b, ApJ, 698, L142

Taylor, J. H. & Cordes, J. M. 1993, ApJ, 411, 674

The VERITAS Collaboration, Acciari, V. A., Aliu, E., et al. 2010, ArXiv e-prints

Van Buren, D. & Greenhouse, M. A. 1994, ApJ, 431, 640

van Eldik, C., Bolz, O., Braun, I., & et al. 2008, in International Cosmic Ray Conference, Vol. 2, International Cosmic Ray Conference, 589–592

VERITAS Collaboration, Acciari, V. A., Aliu, E., et al. 2009, Nature, 462, 770

Vink, J. 2005, in American Institute of Physics Conference Series, Vol. 774, X-ray Diagnostics of Astrophysical Plasmas: Theory, Experiment, and Observation, ed. R. Smith, 241–251

Voges, W., Aschenbach, B., Boller, T., et al. 1999, VizieR Online Data Catalog, 9010, 0

Wagner, R. M., Donnarumma, I., Grube, J., et al. 2009, ArXiv e-prints

Weaver, K. A., Heckman, T. M., Strickland, D. K., & Dahlem, M. 2002, ApJ, 576, L19

Weaver, R., McCray, R., Castor, J., Shapiro, P., & Moore, R. 1977, ApJ, 218, 377

Weekes, T. C., Badran, H., Biller, S. D., et al. 2002, Astroparticle Physics, 17, 221

Weekes, T. C., Cawley, M. F., Fegan, D. J., et al. 1989, ApJ, 342, 379

Weis, K., Corcoran, M. F., Bomans, D. J., & Davidson, K. 2004, A&A, 415, 595

Westerlund, B. E. 1987, A&AS, 70, 311

White, R. L. & Chen, W. 1992, ApJ, 387, L81

Whitelock, P. A., Feast, M. W., Koen, C., Roberts, G., & Carter, B. S. 1994, MNRAS, 270, 364

Whitelock, P. A., Feast, M. W., Marang, F., & Breedt, E. 2004, MNRAS, 352, 447

Wiedner, C. A. 1998, Site aspects of the H.E.S.S. project: astronomical and visibility conditions, H.E.S.S. internal note

Winkler, C., Courvoisier, T., Di Cocco, G., et al. 2003, A&A, 411, L1

Wolk, S. J., Bourke, T. L., Smith, R. K., Spitzbart, B., & Alves, J. 2002, ApJ, 580, L161

Yang, H., Roe, B. P., & Zhu, J. 2005, Nuclear Instruments and Methods in Physics Research A, 555, 370

Zinnecker, H. 2003, in IAU Symposium, Vol. 212, A Massive Star Odyssey: From Main Sequence to Supernova, ed. K. van der Hucht, A. Herrero, & C. Esteban, 80–+

Zinnecker, H. & Yorke, H. W. 2007, ARA&A, 45, 481

Zirakashvili, V. N. & Völk, H. J. 2006, ApJ, 636, 140

Danksagung

An dieser Stelle möchte ich mich bei den Menschen bedanken, die auf die ein oder andere Art und Weise zum Gelingen dieser Arbeit beigetragen haben. Insbesonde gilt mein Dank dabei:

- ◇ Herrn Professor Werner Hofmann, für den gewährten Freiraum bei der Themenwahl, die konstruktive Kritik und die angenehme Arbeitsatmosphäre. Insbesondere für die Möglichkeit meine Arbeit auf internationalen Konferenzen vorstellen zu können möchte ich mich nochmals bedanken.
- ◇ Herrn Professor Heinz Völk, dafür das er sich als Koreferent zur Verfügung gestellt hat und für die Möglichkeit am NGC 253 Science Paper mitzuarbeiten.
- ◇ Meinen Eltern, Desdemona und Klaus-Peter, meinem Bruder Christoph, meiner Schwägerin in spe Claudia und natürlich meinen Grosseltern Erika und Wilfried – Danke, für wirklich Alles die letzten 28 Jahre!
- ◇ Daniil, mein Busenfreund; ohne Dich hätte die letzten 3 Jahre etwas Wesentliches gefehlt. Danke auch für die Übersetzertätigkeit in Armenien und die 62 unvergesslichen Abende an allen möglichen Orten Europas.
- ◇ Christopher van Eldik und Kathrin Egberts für die tolle Zusammenarbeit beim TMVA Paper und die Hilfe beim Zusammenschreiben. Christopher nochmal im Speziellen für die zahllosen Antworten auf alle möglichen Fragen und das stets offene Ohr, egal wie wenig Zeit er selbst hatte.
- ◇ Wilfried Domainko, für die Hilfe bei allen möglichen astronomischen Fragen, dem Korrekturlesen der Dissertation und natürlich den tollen Stunden in Deinem Wohnzimmer.
- ◇ Jim Hinton, für seine Unterstützung und Kooperation die gesamten letzten 3 Jahre, sowie die Möglichkeit in Konferenzen in Hertfordshire und Jaén H.E.S.S. Resultate präsentieren zu können.
- ◇ Joachim, Petter, Robert und Daniil für die tolle Zeit in Armenien und Heidelberg; Stefan, Anne, Kathrin, Rolf und Dalibor für ihre unvergleichliche Art sowie der gesamten Heidelberger H.E.S.S. Gruppe für die tolle Arbeitsatmosphäre.
- ◇ Nicole, Ronny, Alina, Daniel, Carmen und dem ganzen Rest für die Freundschaft, Musik, Filme und die vielen unvergesslichen Stunden.

Und Dir, Jenni. Dir danke ich für das Verständnis all die Jahre, dafür dass Du meinen schlechten Humor so magst (wehe wenn nicht!), für Deine ganze Art und dafür dass Du für mich da bist – ich liebe Dich.